JOURNAL OF MECHANICS OF MATERIALS AND STRUCTURES

msp.org/jomms

Founded by Charles R. Steele and Marie-Louise Steele

Cover photo: Wikimedia Commons

msp

BUCKLING OF TWO-PHASE INHOMOGENEOUS COLUMNS AT ARBITRARY PHASE CONTRASTS AND VOLUME FRACTIONS

MOHAMMED G. ALDADAH, SHIVAKUMAR I. RANGANATHAN AND FARID H. ABED

Buckling is an instability encountered in a wide variety of problems, both in engineering and biology. Almost all engineering structures are designed with adequate safety factors to prevent failure due to buckling, yielding or dynamic loads. In a classical sense, design for buckling is done by carefully controlling the modulus of elasticity, moment of inertia and the length of the structure. Further, such an approach assumes the material to be homogeneous and does not generally account for the microstructural details of the column. In this paper, we study the buckling of inhomogeneous columns with a two-phase checkerboard microstructure. Monte Carlo simulations are used to generate microstructures with arbitrary volume fractions and phase contrasts (ratio of the modulus of individual phases). An analytical form is obtained for the ensemble averaged critical buckling load based on the results of over 18,000 eigenvalue problems at arbitrary volume fractions, phase contrasts and distributions. Further, microstructural realizations that correspond to the highest buckling load (best design) and the lowest buckling load (worst design) are identified and the corresponding distribution of individual phases is determined. Finally, the statistical nature of the critical buckling load is discussed by computing the statistical moments that include the mean and coefficient of variation.

1. Introduction

Buckling is an instability phenomenon that leads to failure of slender members typically subjected to compressive loads. Perhaps the most widely used criterion for the buckling instability is Euler's buckling solution, which predicts the maximum axial compressive load that a slender, homogeneous and ideal column can carry. This classical result states that the critical buckling load is directly proportional to the modulus of elasticity, area moment of inertia, boundary conditions, and is inversely proportional to the square of the column length. This result is limited to long columns and does not account for material inhomogeneity. In reality, inhomogeneous materials are ubiquitous in nature and most materials exhibit inhomogeneity when the microstructural details are taken into account. Such materials can also be engineered to design columns with performance better than their homogeneous counterparts (for instance using 3D printing to create a functionally graded microstructure). Thus, there is an inherent need to understand the effect of material inhomogeneity on the overall response of such columns.

Although the buckling of inhomogeneous and functionally graded columns is still an ongoing area of research, there have been a few important studies that are noteworthy. Elishakoff and Rollot [1999] investigated columns with variable stiffness. In their study, Euler's buckling equation was modified to allow for variable stiffness across the length of the material. Then, using a preselected variable stiffness, the modified Euler equation was solved to obtain the critical buckling load. As a continuation of their

study, Elishakoff [2001] posed the same problem as an inverse buckling problem. The inverse method determined the stiffness distribution $k(x)$ and the critical buckling load P for a nonuniform beam with specified boundary conditions by using a preselected function for the buckling mode. Such a method produces results for a certain class of inhomogeneous materials, yet does not provide exact solutions for general heterogeneity.

Li [2001] derived a solution for the buckling load of nonuniform columns subjected to concentrated axial and distributed loads. In this approach, the governing equations were initially reduced using functional transformation and later solved using Bessel functions. The analytical solution provided results for twelve different cases that are important in engineering applications, such as high-rise buildings subjected to distributed loads. In yet another study, Huang and Li [2012] presented an analytical approach to determine the critical buckling load of a nonuniform column with or without continuous elastic restraint. Their study identified an optimal ratio between the radius in the middle of the cylinder and the radius at the end for maximum carrying load capacity.

Altus et al. [2005] introduced a new method for obtaining the buckling load analytically for linear inhomogeneous materials using the functional perturbation method (FPM). According to them, this method provided more accurate results for linear inhomogeneous materials than the conventional Galerkin and Rayleigh–Ritz methods. Along similar lines, Huang and Luo [2011] derived a solution for the buckling of inhomogeneous beams by using power series to represent the mode shapes. The power series method used was illustrated by studying a composite beam under various end supports. In addition, Morimoto and Tanigawa [2006] investigated the buckling of inhomogeneous rectangular plates subjected to uniform in-plane shear. In their study, an inhomogeneity parameter was introduced which in turn contributed to the bending rigidity. Also, as the inhomogeneity parameter was increased, the buckling load increased, whereas the buckling mode shape was unaffected. Furthermore, Earls [2007] emphasized the numerical limitations of using finite element modeling and eigenvalues in the solution of buckling equations. The limitations included differing results for the same structures using different software packages, and the stability of the results. This indicated the necessity to carefully assist the finite element solution with closed form analytical solutions or experiments wherever possible.

More recently, Li et al. [2011] solved the buckling equation for composite nonuniform columns with distributed axial loads or tip forces and used the solution to tailor materials such that the ratio of the buckling load to the weight is maximized for axially graded inhomogeneous composite columns with uniform cross-section. The optimization technique was performed on a column with a clamped end and a free end and resulted in the need to increase material density around the free end to increase the maximum load carrying capacity. Also, Singh and Li [2009] formulated a transcendental eigenvalue problem for elastically restrained functionally graded columns. In the problem they approximated a nonhomogeneous column with a piecewise function with constant geometrical and material properties. The resulting eigenvalue problem was then solved using a new numerical algorithm with different boundary conditions.

This paper presents a new study investigating the buckling capacity of inhomogeneous columns with two-phase checkerboard microstructures at arbitrary phase contrasts and volume fractions. To the best of our knowledge, the buckling of such two-phase checkerboard columns has not been investigated in the past. The microstructure of this column is made up of two materials with very different elastic moduli. A Monte Carlo technique is used to generate checkerboard microstructures at arbitrary phase contrasts, volume fractions and spatial distributions of the phases. After generating the microstructure,

the eigenvalue problem is then solved numerically using linear perturbation analysis that is implemented in the commercial finite element software ABAQUS [2004]. This procedure is repeated for all microstructural realizations, with the following objectives: (i) determine the critical buckling load for checkerboard columns as a function of the volume fraction; (ii) study the effect of phase contrast on the critical buckling load; (iii) identify the microstructural realizations (spatial distribution of individual phases) that result in achieving the highest and the lowest buckling loads for a given volume fraction.

2. Problem formulation

2.1. *General buckling equation.* The governing equation for the buckling of an inhomogeneous long column is given by the equation

$$E(x)I\frac{\partial^2 v}{\partial^2 x} + P_{\mathrm{cr}}v = 0, \tag{1}$$

where $E(x)$ indicates the spatial dependence of the modulus of elasticity, I represents the area moment of inertia, v is the transverse deflection and P_{cr} is the critical buckling load. It is well-known that for a homogeneous column with $E(x) = E$, the critical buckling load is given by $P_{\mathrm{cr}} = C\pi^2 EI/L^2$. Here, C is a constant representing the type of boundary condition and L is the column length.

In the present study, the microstructure is a two-phase material with a random checkerboard microstructure. Such a random checkerboard can be considered as a set of deterministic checkerboards: $\mathrm{B} = \{B(\omega) : \omega \in \Omega\}$ (see [Ostoja-Starzewski 1998]). Here, Ω is the realization space ($\Omega = 2^{100}$) and ω is the specific microstructural realization under consideration. For a two-phase checkerboard column with phases 1 and 2, $B(\omega) = B_1 \cup B_2$, with the local moduli of elasticity given by E_1 and E_2, respectively. Mathematically, the microstructure can be defined completely using the indicator function defined as [Ostoja-Starzewski 1998]

$$\chi_1(\vec{x}, \omega) = \begin{cases} 1 & \text{if } \vec{x} \in B_1, \\ 0 & \text{if } \vec{x} \in B_2. \end{cases} \tag{2}$$

Using (2), the local modulus of elasticity at any point in the column can be identified as follows:

$$E(\vec{x}, \omega) = \chi_1(\vec{x}, \omega)E_1 + [1 - \chi_1(\vec{x}, \omega)]E_2, \tag{3}$$

where $\vec{x}$ is a position vector and E_1 and E_2 are the moduli of elasticity of the individual phases. The volume fraction of phase 1 can be simply recovered by the ensemble averaging of the indicator function

$$\alpha = \langle \chi_1 \rangle. \tag{4}$$

Due to the randomness introduced in the distribution of the individual phases as well as the volume fraction, it is difficult to find an analytical solution to (1) that simultaneously satisfies continuity of displacement and tractions between the individual phases. Thus, in this study we use Monte Carlo runs along with finite element analysis to solve (1) and obtain the critical buckling load for each realization.

2.2. *Finite element modeling using linear perturbation analysis.* As mentioned previously, a Monte Carlo technique is employed to generate checkerboard microstructures at arbitrary phase contrasts, volume fractions and the spatial distributions the phases. After generating the microstructure, the eigenvalue problem is then solved numerically using linear perturbation analysis using the finite element
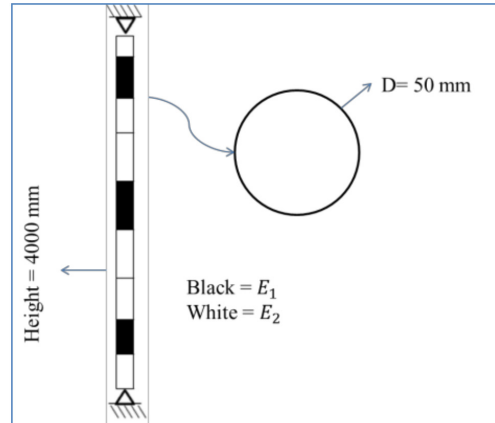
Figure 1. Two-phase checkerboard column with circular cross section.

software ABAQUS due to its versatility in handling such problems. A linear perturbation analysis step provides the linear response of the system about the base state, and estimates elastic buckling load via eigenvalue extraction. Eigenvalue buckling is generally used to approximate the critical buckling loads of stiff structures. Usually the loading on stiff structures is either an axial or membrane loading. The response to such loading involves small deformation before buckling. A simple example of stiff structure is the Euler column, which responds very stiffly to a compressive axial load until a critical load is reached, when it bends suddenly and exhibits a much lower stiffness. However, estimation using general eigenvalue extraction is useful, especially if the perturbation loads are elastic before the buckling occurs. The eigenvalue solution is obtained by making the model stiffness matrix singular. The model matrix is then described by $K^{ij}v^i = 0$, where K^{ij} is the tangent stiffness matrix and v^i is the displacement matrix [ABAQUS 2004].

In the proposed study, a column with a circular cross-section with diameter 50 mm and length of 4000 mm was used for the proposed analysis (see Figure 1). The dimensions were chosen such that elastic buckling is always ensured. Pinned connections were considered for both ends. The column is modeled with different material configurations for each simulation using deformable Timoshenko beam elements coded as B21 in ABAQUS. This type of line element accounts for the transverse shear stress. This is because Schnabl and Planinc [2011] have demonstrated that the transverse shear stress does affect the critical buckling load. Also, the B21 element is of much relevance to the current study as it provides better results for slender beams [ABAQUS 2004]. As for the boundary condition used in the FE modeling, the pin-pin connection was modeled by not allowing deformation in the axial and transverse directions for the bottom end. The restriction of deformation was only applied on the transverse direction for the top end to allow loading in the axial direction.

2.3. *Materials combinations.* In each analysis step, the column consists of two materials with different elastic modulus (E). The choice of the two materials used is based on the contrast, which is the ratio between the largest and the smallest elastic moduli, and can be calculated using the equation

$$k = E_1/E_2. \tag{5}$$

Material 1	Material 2	E_1 (GPa)	E_2 (GPa)	k
Steel	Magnesium	200	45	4.44
Steel	Wood	200	11	18.2
Magnesium	Wood	45	11	4.1
Copper	Aluminum	168	69	2.43

Table 1. Material combinations.

Table 1 presents the material combinations considered in the present study. The choice of materials was purely on the basis of providing different levels of contrast varying from very low to very high ratios. Columns made of steel and wood have the highest contrast, while columns made of aluminum and copper hold the lowest contrast. The other two conditions have almost equal contrasts. The use of a similar contrast helps in identifying behavioral similarities of the material combinations.

3. Methodology

For each analysis realization, the column is discretized into 100 segments, and each segment is assigned a random combination of E_1 and E_2. The volume fraction is changed by increasing the fraction of E_1 from 0% to 100% in increments of 10%. For each value of the E_1 volume fraction (10%, ..., 90%), the numerical simulations are performed 500 times to account for material randomness; moreover, the simulations are repeated for each material combination, with values of contrast k equal to, respectively, 2.43, 4.1, 4.4 and 18.2. Thus a total of $9 \times 4 \times 500 = 18,000$ runs were conducted, in order to determine the critical buckling load and to identify the microstructural realizations (spatial distribution of individual phases) that resulted in the highest and the lowest buckling loads for each volume fraction.

Figure 2 highlights the methodology employed in the current study. In step (a), a particular realization of the checkerboard is sampled randomly and its finite element model is set up in ABAQUS. The pin-pin
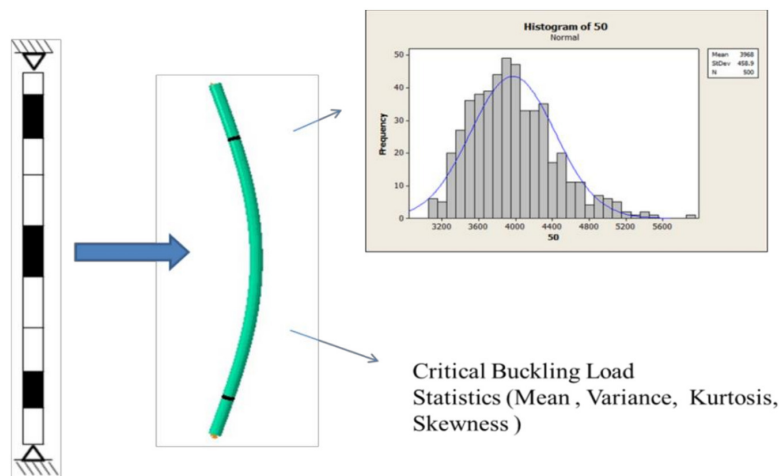
Figure 2. Methodology employed: microstructure of the column (left), buckling mode shape (middle), and statistical moments (right).

boundary conditions are then applied at the column ends. Next, in step (b), a concentrated unit load was applied and the eigenvalue problem was solved to obtain the mode-one critical buckling load and the corresponding mode shape. The procedure was repeated over 18,000 times in order to cover the entire realization space.

Subsequently, in step (c), the results were compiled to determine the minimum, maximum and ensemble averaged buckling load for each volume fraction and contrast. Also, the spatial distributions of the phases corresponding to the maximum and minimum buckling load were determined to identify the microstructure that corresponds to the best and worst designs, respectively. Finally, statistical analysis of the results was performed to obtain various statistical moments such as the mean and coefficient of variation.

4. Results and discussion

4.1. *Critical buckling load of the checkerboard column as a function of the volume fraction.* Prior to a discussion on the numerical results, it is convenient to define a rescaled buckling load, as follows:

$$P_c = \frac{P_{cr}L^2}{\pi^2 I},\tag{6}$$

where P_{cr} is the numerically obtained mode-one critical buckling load and P_c is the rescaled buckling load (typically in GPa). An alternative interpretation of P_c would be the equivalent effective elastic modulus of the checkerboard column. Depending upon the context, P_c could either represent the mean, minimum or the maximum rescaled buckling load.

Figure 3, left, presents the rescaled buckling load (average, maximum and minimum) for a checkerboard column made up of steel and wood. The modulus of elasticity for wood is 11 GPa and that of steel is 200 GPa, and thereby the contrast of the microstructure is $k = 18.2$. It is evident from this figure that the lower-modulus material (wood) affects the rescaled buckling load significantly more than the material with higher modulus (steel). Even at 50% volume fraction, the average value of the rescaled buckling load is only about 20.85 GPa. Similarly, the rescaled buckling load (average, maximum and
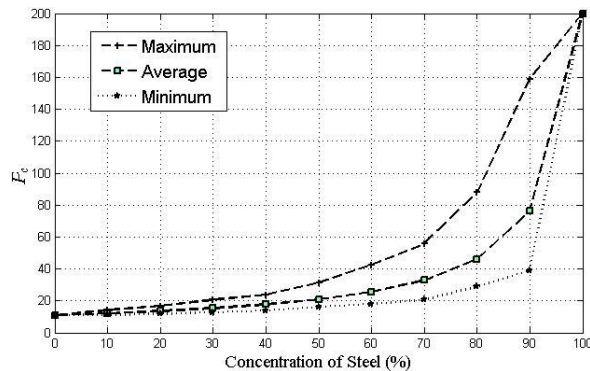
steel and wood microstructure ($k = 18.2$)   steel and magnesium microstructure ($k = 4.44$)
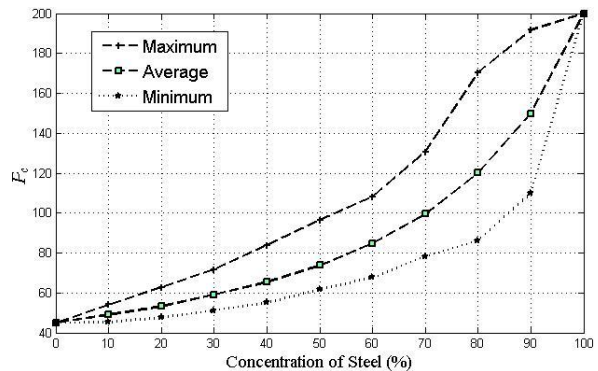
Figure 3. Rescaled buckling load (average, maximum and minimum) as a function of the volume fraction, for the first two material combinations.

magnesium and wood microstructure ($k = 4.1$)   ductile iron and aluminum ($k = 2$)
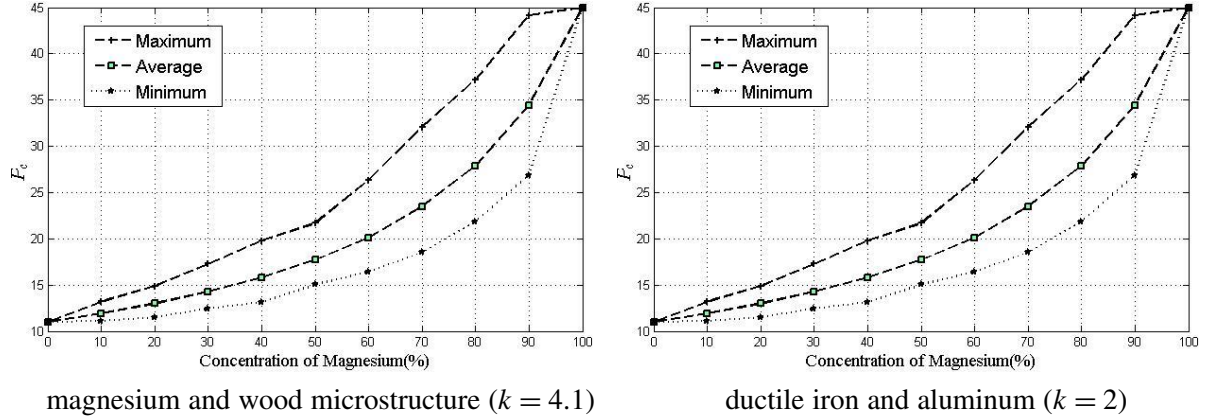
Figure 4. Rescaled buckling load (average, maximum and minimum) as a function of the volume fraction, for the last two material combinations.

minimum) for checkerboard columns made up of steel and magnesium ($k = 4.44$) and magnesium and wood ($k = 4.1$) are plotted in Figure 3, right, and Figure 4, left. The material properties for the individual phase are given in Table 1. It is evident from these plots that as the volume fraction of the stiffer material increases, the rescaled buckling capacity of the column increases. At a volume fraction of 50%, the rescaled buckling loads are 73.46 GPa and 17.68 GPa, respectively. Further, it can be noticed that the trends for the average, minimum and maximum rescaled buckling loads are identical for microstructures with similar contrasts. Finally, the rescaled buckling load (average, minimum and maximum) for ductile iron and aluminum is plotted in Figure 4, right. This particular microstructure has a contrast of 2.43.

Based on the numerical results obtained, it is possible to infer the analytical form for the average value of the rescaled buckling load as well as the ensemble averaged critical buckling load, as given in the equations

$$\langle P_c \rangle = \frac{E_1 E_2}{\alpha E_2 + (1 - \alpha) E_1} \qquad \text{(rescaled ensemble averaged buckling load)}, \qquad (7a)$$

$$\langle P_{cr} \rangle = \frac{\pi^2 I}{L^2} \frac{E_1 E_2}{\alpha E_2 + (1 - \alpha) E_1} \qquad \text{(ensemble averaged buckling load)}. \qquad (7b)$$

Here, E_1 and E_2 are the individual phase elastic moduli, α is the volume fraction of the phase 1, and the operator $\langle \cdot \rangle$ indicates the ensemble averaging.

4.2. *Effect of phase contrast on critical buckling load.* In order to clearly understand the effect of phase contrast, the notion of normalized buckling load is introduced. This is obtained by normalizing the maximum and minimum buckling load for each material combination with the ensemble averaged buckling load for the given combination:

$$P_n = P_{cr} / \langle P_{cr} \rangle. \qquad (8)$$

In Figure 5, left, the normalized buckling load is plotted as a function of contrast and volume fraction of the stiffer phase. When the volume fraction is 0% or 100%, all the curves converge to $P_n = 1$. This is
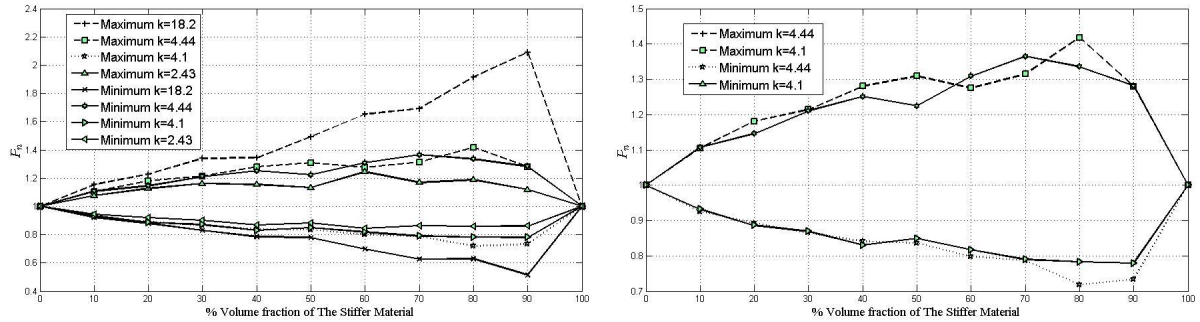
Figure 5. Normalized buckling load (maximum and minimum) as a function of the volume fraction of the stiffer phase. Left: differing contrasts. Right: similar contrasts.

because the microstructure is essentially homogeneous at these volume fractions. It is also evident from this plot that with increasing contrast, the curves for maximum and minimum normalized buckling loads are farther apart. Furthermore, from Figure 5, right, it is evident that these curves are identical when the contrasts are similar. Based on these observations, one can postulate the following functional form for the normalized buckling load:

$$P_n = f(\alpha, k). \tag{9}$$

4.3. *Spatial distribution of individual phases.* In order to determine the spatial distribution of individual phases corresponding to the maximum (best column design) and minimum (worst column design) buckling loads, the corresponding buckling mode shapes are plotted as a function of volume fraction, as shown in Figure 6. The top panel corresponds to a contrast of 2.43 and the bottom one to a contrast of 18.2. From these graphs, it is evident that for maximizing the buckling load, it is desirable to distribute
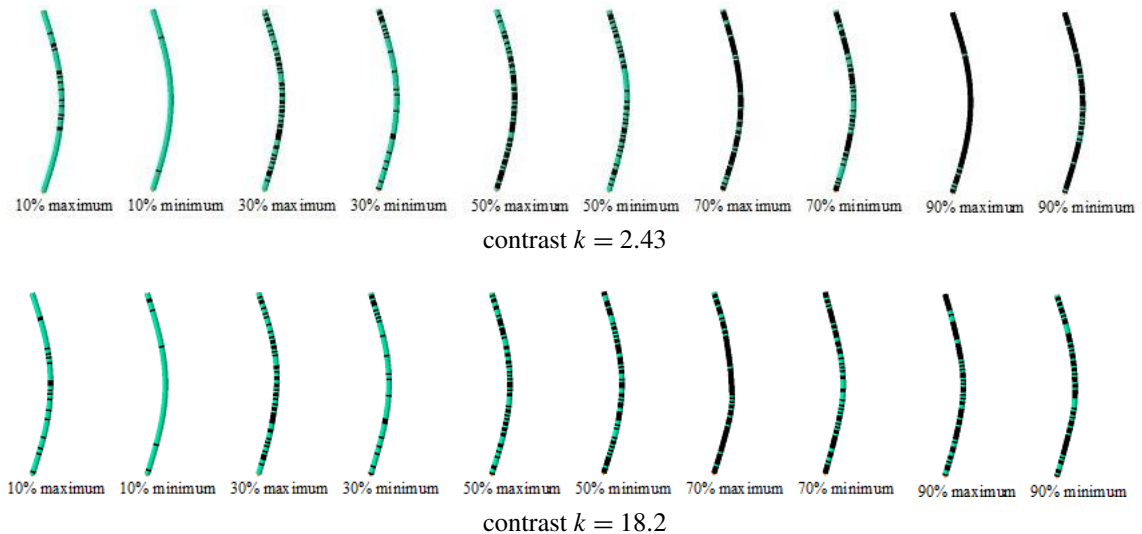
Figure 6. Buckling mode shapes corresponding to the maximum and minimum buckling load as a function of volume fraction.
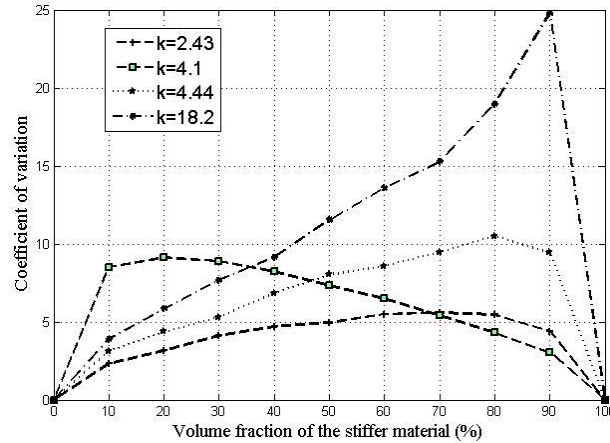
Figure 7. Data statistics: coefficient of variation.

the phase with higher stiffness in the middle of the column and vice versa for the minimum buckling load. This essentially implies that by allocating the phase with higher stiffness in the region with higher deflection, the buckling capacity is enhanced.

4.4. *Statistical analysis.* The numerical simulations performed in this study resulted in 18,000 simulations, and the pool of results for the buckling load is best analyzed using statistical tools that include the mean and coefficient of variation. The result on the mean value of the buckling load has been extensively discussed in the previous sections. The coefficient of variation for the data set is plotted as a function of contrast and volume fraction in Figure 7. As expected, it is zero for a homogeneous material that corresponds to 0% or 100% volume fraction. In general, as the contrast increases, the coefficient of variation also increases. It is interesting to note that the coefficient of variation for the steel-magnesium checkerboard ($k = 4.44$) and that of the magnesium-wood microstructure ($k = 4.1$) are about the same when the magnesium volume fraction is kept the same. Finally, it is worthwhile to note that the determination of higher moments such as the skewness and kurtosis would require significantly more realizations and would be computationally very expensive.

5. Conclusion

In this paper, a Monte Carlo technique was used to generate checkerboard microstructures at arbitrary phase contrasts, volume fractions and spatial distributions of the phases. Subsequently, the resulting eigenvalue problems were solved numerically in ABAQUS using linear perturbation analysis. The maximum, average and the minimum values for the critical buckling load were determined and the corresponding buckling mode shapes were identified under pin-pin boundary conditions. It was demonstrated that the ensemble averaged rescaled buckling load $\langle P_c \rangle$ was simply the volume-fraction weighted harmonic mean of the individual phase elastic moduli. Also, the normalized buckling load P_n was identical for microstructures with similar contrasts. Furthermore, it was demonstrated that distributing the phase with higher stiffness in regions of higher deflections (middle) maximizes the buckling capacity of the column and vice versa. Finally, a statistical analysis on the numerical results was conducted by studying the mean

and coefficient of variation as a function of contrast and volume fraction. To the best of our knowledge, this is the first time an analytical result has been proposed for the critical buckling load of a column with a random checkerboard microstructure.

References

[ABAQUS 2004] ABAQUS, *User manual 6.3*, Habbitt, Karlsson and Sorensen, Providence, RI, 2004.

[Altus et al. 2005] E. Altus, A. Proskura, and S. Givli, "A new functional perturbation method for linear non-homogeneous materials", *Int. J. Solids Struct.* **42**:5–6 (2005), 1577–1595.

[Earls 2007] C. J. Earls, "Observations on eigenvalue buckling analysis within a finite element context", in *Proceedings of the SSRC annual stability conference* (New Orleans, LA), edited by C. Stratman, Structural Stability Research Council, Rolla, MO, 2007.

[Elishakoff 2001] I. Elishakoff, "Inverse buckling problem for inhomogeneous columns", *Int. J. Solids Struct.* **38**:3 (2001), 457–464.

[Elishakoff and Rollot 1999] I. Elishakoff and O. Rollot, "New closed-form solutions for buckling of a variable stiffness column by Mathematica", *J. Sound Vib.* **224**:1 (1999), 172–182.

[Huang and Li 2012] Y. Huang and X.-F. Li, "An analytic approach for exactly determining critical loads of buckling of nonuniform columns", *Int. J. Struct. Stab. Dyn.* **12**:4 (2012), 1250027.

[Huang and Luo 2011] Y. Huang and Q.-Z. Luo, "A simple method to determine the critical buckling loads for axially inhomogeneous beams with elastic restraint", *Comput. Math. Appl.* **61**:9 (2011), 2510–2517.

[Li 2001] Q. S. Li, "Exact solutions for buckling of non-uniform columns under axial concentrated and distributed loading", *Eur. J. Mech. A Solids* **20**:3 (2001), 485–500.

[Li et al. 2011] X.-F. Li, L.-Y. Xi, and Y. Huang, "Stability analysis of composite columns and parameter optimization against buckling", *Compos. B Eng.* **42**:6 (2011), 1337–1345.

[Morimoto and Tanigawa 2006] T. Morimoto and Y. Tanigawa, "Linear buckling analysis of orthotropic inhomogeneous rectangular plates under uniform in-plane compression", *Acta Mech.* **187**:1-4 (2006), 219–229.

[Ostoja-Starzewski 1998] M. Ostoja-Starzewski, "Random field models of heterogeneous materials", *Int. J. Solids Struct.* **35**:19 (1998), 2429–2455.

[Schnabl and Planinc 2011] S. Schnabl and I. Planinc, "The effect of transverse shear deformation on the buckling of two-layer composite columns with interlayer slip", *Int. J. Non-Linear Mech.* **46**:3 (2011), 543–553.

[Singh and Li 2009] K. V. Singh and G. Li, "Buckling of functionally graded and elastically restrained non-uniform columns", *Compos. B Eng.* **40**:5 (2009), 393–403.

MOHAMMED G. ALDADAH: maldadah@alumni.aus.edu
Department of Mechanical Engineering, American University of Sharjah, 26666, United Arab Emirates

SHIVAKUMAR I. RANGANATHAN: ranganathan@rowan.edu
Department of Mechanical Engineering, Rowan University, 201 Mullica Hill Road, Glassboro, NJ 08028, United States

FARID H. ABED: fabed@aus.edu
Department of Civil Engineering, American University of Sharjah, 26666, United Arab Emirates

msp

A NONLINEAR STRESS-STRETCH RELATIONSHIP
FOR A SINGLE COLLAGEN FIBRE IN TENSION

FRANCESCO GENNA

A new stress-strain equation for a single, stretched collagen fibre (bundle) is developed, based on the statistical description of the fibre microstructure, down to the tropocollagen molecule level. The derivation follows previous work of Annovazzi and Genna (2010), but the modifications reported here both simplify and improve the final result. The model is governed by physically meaningful parameters. Comparisons between the model predictions and some available experimental results suggest that the proposed model could be of value in bioengineering applications.

1. Introduction

In [Annovazzi and Genna 2010] (hereafter referred to as [AG]), a constitutive model for a single collagen fibre was derived on the basis of assumptions concerning both the fibre microstructure and the mechanical behaviour of the tropocollagen molecule. The present paper aims at simplification, improvement, and better internal consistency with respect to what done in [AG].

The main motivation for this work is the relative scarcity of constitutive models for the stress-stretch behaviour of a single collagen fibre in tension. The most commonly adopted assumptions for the collagen fibre constitutive law are in fact still not fully adequate. They might be either unrealistic, such as linear elasticity, or purely phenomenological, such as linear or nonlinear viscoelasticity, or hyperelasticity, based on the definition of potential functions that depend on parameters having no physical meaning. One reason for this could be the fact that the interest is often focussed on tissue analysis, so complicated in itself that it leaves little space for an accurate description of the underlying constituents, i.e., the single fibres. Examples of this type of difficulty can be found in [Grytz and Meschke 2009; Cacho et al. 2007; Wang et al. 1997; Limbert 2011].

To the best of our knowledge, only one attempt — that of [AG] — has been made at deriving a microstructurally based stress-stretch law for a single collagen fibre. This could cover the whole range of possible tensile loading, and described the microstructure of the fibre itself, which includes several levels of subcomponents, down to the molecular level [Kastelic et al. 1978]. The fibre stress-strain relationship presented in [AG] was based on the statistical description of the crimp properties of all the internal levels — four, according to the available information — of the fibre itself. The results obtained in [AG], however, could be improved in several respects:

- in the absence of data concerning the tropocollagen molecule, the equation for the elastic behaviour at the molecular level was taken, in [AG], from a model developed for a DNA molecule, an extension of the so-called WLC model of [Bustamante et al. 2000];

- the failure of the tropocollagen molecule was described in [AG] on the basis of uncertain force data concerning the DNA molecule;

- the assumptions regarding the statistics of the waviness at the molecular level were inconsistent, in [AG], which resulted in needless analytical complications;

- crosslinking was ignored;

- all the subfibrils, at all the sublevels, were assumed to be continuous and stress-carrying, ignoring the existence of both interrupted subfibrils and of extra fibrous matter/voids;

- all the probability density functions for all the random variables, in [AG], were taken as Gaussian; this created some inconsistency in the definition of the governing parameters.

Here, a modification of the model of [AG] is presented. It overcomes the quoted problems and, at the same time, it is much simpler, and is better suited to be adopted even in large-scale applications, as shown in an accompanying paper [Genna and Paganelli 2014]. The main features of the constitutive model described here are of two types: those that follow what was already presented in [AG], and those which modify and improve the previous approach. In summary:

Retained features:

- a collagen fibre, or bundle, is seen as having an internal hierarchy of 4 sublevels of wavy or crimped subfibres, arranged in parallel at each sublevel; the waviness at each level is treated as a random variable;

- all the random variables are considered as stochastically independent;

- no compressive or bending stiffness is considered;

- the tropocollagen molecules are seen as forming wavy cables, of which the stress-carrying ones are treated as continuous, running from end to end of the bundle, and having an elastic-brittle behaviour.

New features:

- a bilinear elastic law is adopted for the tropocollagen molecule, as suggested in [Buehler and Wong 2007];

- the statistical aspects of the molecular failure are based on a simpler yet more consistent assumption, expressed in terms of displacement instead of force;

- crosslinking is accounted for;

- a beta probability density function is chosen for the statistics of all the random quantities;

- account is taken of the possible coexistence, at any sublevel, of stress-carrying and non-stress-carrying material.

The model herein proposed is valid for any material — and specially for soft tissues or tissue components — whose internal microstructure is made by nested wavy thin cables. Its effectiveness, in the context of collagen, is tested by comparing its predictions with the results of experiments available in the literature for single collagen fibres. An indirect verification is also presented, obtained by inserting the new fibre stress-stretch equation into a previously developed model for the mechanical behaviour in tension of the periodontal ligament (PDL) [Genna 2006].

2. Theory: the constitutive model

Figure 1 shows a sketch of the assumed hierarchy of subcomponents inside a collagen fibre, based on the description presented, for instance, in [Kastelic et al. 1978]. This follows [AG]; Figure 1 also shows the approximate geometrical scales of each level. The nomenclature adopted here is the following:

- Collagen fibre (or bundle, or fascicle): this is called here "level 0", and it is the component for which we desire to obtain a stress-stretch equation, starting from its uncoiled, unstretched configuration. Its characteristic diameter is, for collagen types I, II, and III, of about $100\,\mu$m. The uncoiled, unstretched length of the fibre, inside the proposed model, is taken as deterministic, denoted by L_b.

- Fibril: this is called here "level 1", and has a typical diameter of about 10 to 500 nm. This component exhibits a typical banded structure, with a period of about 65 nm, that derives from the features of the molecular arrangement [Petruska and Hodge 1964].

- Subfibril: this is called here "level 2". According to [Kastelic et al. 1978], this entity, of diameter ranging from 10 to 20 nm, has been described in previous literature; it seems hard to be distinguished from the next one (see also [AG]).

- Microfibril, formed by five tropocollagen units joined together: this is called here "level 3", and has a typical diameter of 3.5 nm;

- Tropocollagen molecule, having a diameter of 1.5 nm: this is the lowest level considered here, i.e., "level 4".
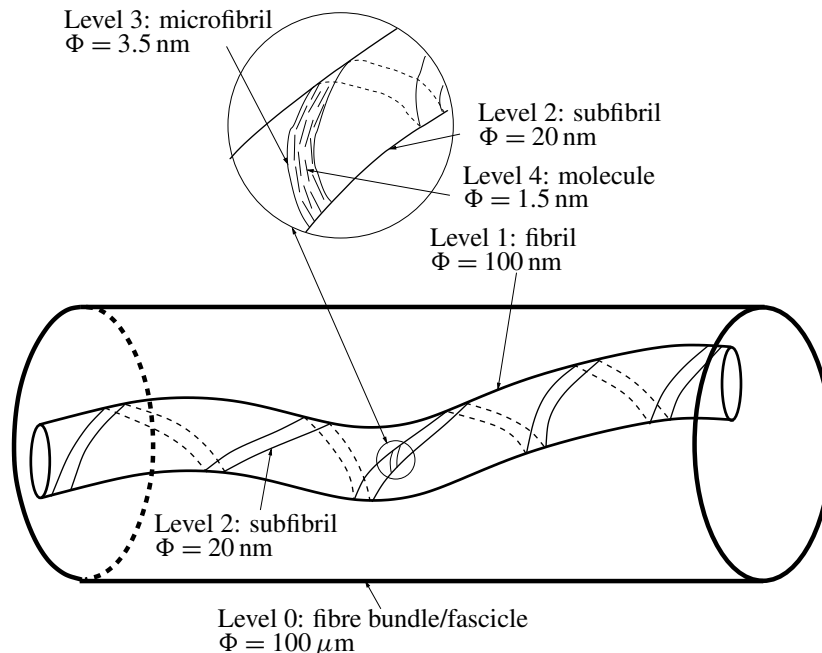
Figure 1. Schematic representation of the internal structure of a fibre-forming collagen fibre, as proposed for instance in [Kastelic et al. 1978].

List of abbreviations

A_m	Molecular cross-section area	$1.7671\,\text{nm}^2$
f_i	Volume fraction of fibrous matter in cable i	
F_s	Molecular force at the end of stiffness stage 2	
F_m	Molecular force	
$F_{4,A}$	Force in cable 4 during molecular stiffness stage 2	
$F_{4,B}$	Force in cable 4 during molecular stiffness stage 3	
K_s	Molecular stiffness in molecular stiffness stage 2	$10\,\text{pN/nm}$
K_m	Molecular stiffness in molecular stiffness stage 3	$30\,\text{pN/nm}$
$L_{0,i}$	Coiled end-to-end distance of a cable at level i	Random
$L_{0,m}$	Coiled end-to-end distance of a single molecule	Random
L_b	Unstretched uncoiled length of a collagen fibre	
$L_{d,i}$	Unstretched uncoiled length of a cable at level i	Random
L_m	Unstretched uncoiled length of a single molecule	$301.7\ (204.9)\,\text{nm}$
M	Number of molecules in cable at level 4	Random
N	Total number of levels (cables) in the cable microstructure	4 for a fibre of collagen type I, II, and III
s	Molecular displacement range spanned by stiffness stage 2	
u_1	Deterministic value of the displacement that stretches a collagen fibre	
u_f	Failure molecular displacement	Random
u_f^*	Difference between failure molecular displacement and displacement at the end of the first (entropic) stiffness stage	
u_i	Displacement of cable at level i starting from situation when cable $i-1$ is uncoiled and unstretched	
$\bar{u}_i$	Displacement u_i corresponding to complete uncoiling, but with no stretching, of cable at level i	
u_m	Molecular displacement starting from rest (coiled) configuration	
$\bar{u}_m$	Molecular displacement u_m corresponding to complete uncoiling, but with no stretching, of a single molecule	
u_s	Molecular displacement u_m corresponding to the end of stiffness stage 2 of a single molecule	Random
X_f	Crosslink parameter affecting molecular failure	
X_{ks}	Crosslink parameter affecting the stiffness in molecular stiffness stage 2	
X_{km}	Crosslink parameter affecting the stiffness in molecular stiffness stage 3	
y_i	Ratio between coiled end-to-end distance and unstretched uncoiled length of cable at level i	Random
z_4	Product $y_1 y_2 y_3 y_4$	Random
z_A	Current value of variable z_4 at the beginning of molecular stiffness stage 2 for cable 4	
z_B	Current value of variable z_4 at the transition between molecular stiffness stages 2 and 3 for cable 4	
z_C	Current value of variable z_4 at failure for cable 4	
$z_{C,0}$	Value of variable z_4 at failure for cable 4 with zero crosslinking	
Φ_m	Molecular diameter	$1.5\,\text{nm}$
σ_0	Cauchy stress in a collagen fibre	Random
σ_i^e	Stress in the non-fibrous matter in a cable at level i	0
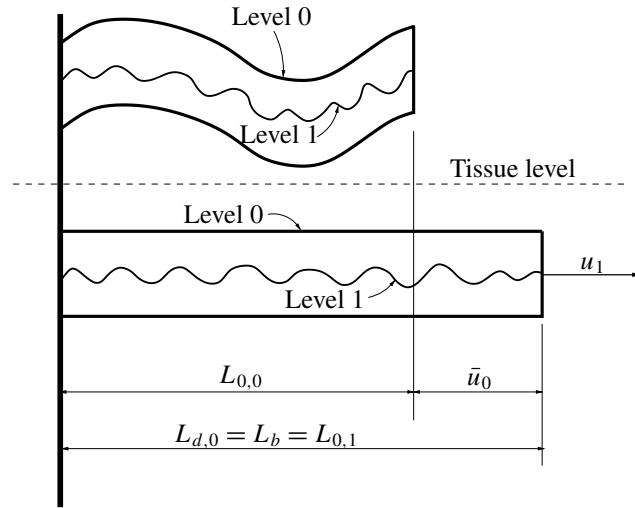
Figure 2. Symbols adopted for the top two levels in the assumed hierarchy. Level 0 is the collagen fibre; level 1 is a collagen fibril; u_1 is the deterministic input displacement value, corresponding to actual stretching of the collagen fibre.

In the model presented here, all the stress-carrying subcomponents, at all levels, are assumed to be continuous wavy cables, running from end to end of the collagen fibre. At each level i, a random number of stress-carrying extensible cables exist, with a wavy/crimped geometry. They are characterised by their uncoiled, unstretched length $L_{d,i}$, and by their coiled end-to-end distance, denoted by $L_{0,i}$, never longer than $L_{d,i}$. Both $L_{d,i}$ and $L_{0,i}$ are defined in an undeformed configuration, taken at the instant when the upper level, $i - 1$, is fully uncoiled but unstretched. Figure 2 shows the geometry assumed for the first two levels, 0 and 1, defined above. A list of all the symbols adopted in the rest of this work is provided on the previous page for convenience.

The constitutive equation derived here concerns level 0, *starting from the instant at which, upon a prescribed fibre displacement, the fibre has become completely uncoiled*. What happens before must be described at the tissue level, since it concerns geometrical properties of the collagen fibre itself. Therefore, the displacement of interest here, taken as the main input data of deterministic value, is the one denoted as u_1 in Figure 2, i.e., the displacement that causes an actual stretch in the collagen fibre. We assume that if $u_1 \leq 0$, no stress exists in the fibre.

Figure 3 shows the geometrical features of the considered problem at a generic level i. At each level, the subfibril displacement u_i is defined starting from the coiled, unstretched configuration with end-to-end distance $L_{0,i}$. For each level i one has

$$L_{d,i} = L_{0,i+1}, \quad i = 0, \ldots, N-1, \tag{1}$$

where N indicates the total number of sublevels in the considered microstructure; for a collagen fibre, N will always be set equal to 4. Equation (1) implies, as shown in Figure 2, that the deterministic input length L_b corresponds to

$$L_b = L_{d,0} = L_{0,1}. \tag{2}$$
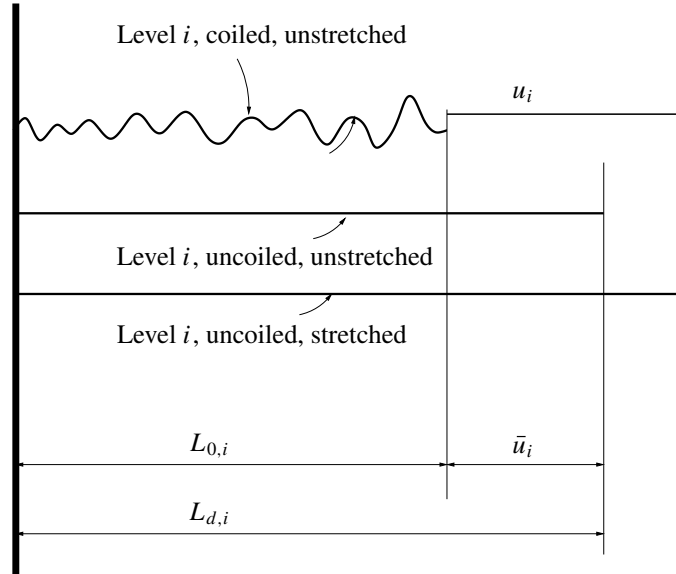
Figure 3. Symbols adopted for a generic internal level of the assumed microstructure.

The displacement u_i contains a part that uncoils the subcomponent i without stretching it: this part is denoted by $\bar{u}_i$, defined as

$$\bar{u}_i = L_{d,i} - L_{0,i} \geq 0. \tag{3}$$

For each level i, the following nondimensional quantity is defined:

$$y_i = \frac{L_{0,i}}{L_{d,i}}, \quad 0 < y_i \leq 1, \tag{4}$$

i.e., the ratio between the coiled end-to-end distance and the uncoiled, unstretched length of the subfibrils at that level. The quantities y_i are assumed to be random variables, governed by a probability density function of the beta type [Ross 2004], because of their taking values in the interval [0, 1]. It is assumed that (i) the quantities y_i, for all i, are stochastically independent, and that (ii) a mean value $E(y_i)$ and a variance $\mathrm{Var}(y_i)$ of each y_i are both known.

Exploiting (1)–(4), and following the same path taken in [AG] (where, though, a different definition of the random variables was adopted), the following results can be obtained:

$$L_{d,i} = \frac{L_b}{\prod_{j=1}^{i} y_j}, \quad 1 \leq i \leq N, \tag{5}$$

$$u_i - \bar{u}_i = u_1 + L_b\left(1 - \frac{1}{\prod_{j=1}^{i} y_j}\right), \quad 1 \leq i \leq N. \tag{6}$$

It is now necessary to define the mechanical behaviour at the tropocollagen molecule level, herein called "level 4".
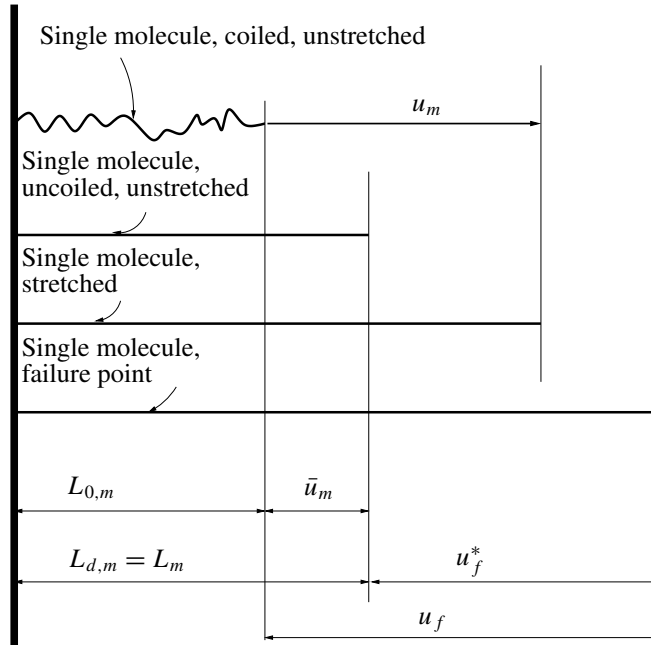
Figure 4. Symbols adopted for the displacements of a single tropocollagen molecule. The uncoiled, unstretched length $L_{d,m}$ of a single molecule coincides with its contour length L_m.

Figure 4 shows the geometry and the symbology adopted for a *single* molecule. Note that all the symbols previously introduced refer to continuous subcomponents, at all levels, running from end to end of the collagen fibre. In Figure 4, the subscripts m and f refer instead to a single molecule, and u_m is the molecular displacement defined from the coiled, unstretched configuration of a single molecule.

The contour length L_m is the uncoiled, unstretched length of the molecule, usually (but not always) taken equal to $L_m = 301.7$ nm (see for instance [Buehler and Wong 2007]). It is the sum of the end-to-end distance of the coiled molecule, $L_{0,m}$, with the displacement $\bar{u}_m$ necessary to fully uncoil the molecule. Both these quantities are assumed to be random variables. The displacement u_f^* that brings the molecule from its uncoiled state up to the brittle failure point (see for instance [Bozec and Horton 2005] and [Buehler and Wong 2007] for experimental evidence of the aspect of a stress-strain curve in tension of a tropocollagen molecule) is assumed to have a deterministic value; yet, the total failure displacement $u_f = \bar{u}_m + u_f^*$, defined as starting from the coiled configuration, is also a random variable.

The mechanical properties of a single molecule are defined on the basis of results presented in [Buehler and Wong 2007], where three stages are recognised in the tensile force-displacement behaviour: a first one, of entropic elasticity, up to an axial force of about 10–15 pN; a second one, corresponding to the uncoiling of the molecule triple helix; and a third stage, where the molecular bonds are stretched, that ends with brittle fracture, at a displacement u_f^* of about 150 nm.

Here, the first stage is neglected, assuming that, for $u_m \leq \bar{u}_m$, the molecular force is zero. Next, a bilinear elastic-brittle force-displacement law is assumed, illustrated in Figure 5. The molecule starts furnishing stiffness when $u_m > \bar{u}_m$; at this instant a second stiffness stage begins, spanning a displacement
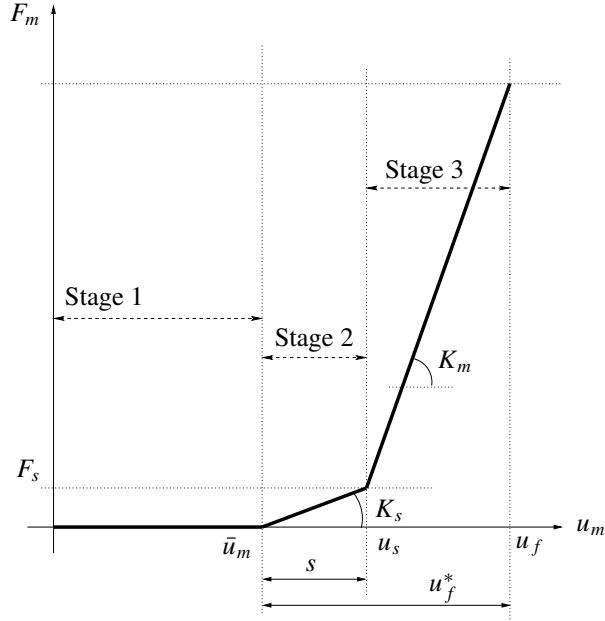
Figure 5. Bilinear force-displacement law adopted for a single tropocollagen molecule. F_m is the molecular force; u_m is the molecular displacement, defined from the initial (coiled) state; u_f indicates the brittle failure point. Both s and u_f^* are assumed to be deterministic quantities. Stage 1 corresponds to entropic elasticity, herein neglected. Stage 2 corresponds to the helix uncoiling phase. Stage 3 corresponds to actual molecular stretching.

range denoted by s. This stage 2 ends at a displacement u_s given by

$$u_s = \bar{u}_m + s. \tag{7}$$

During this stage 2, for $\bar{u}_m \leq u_m \leq u_s$ the molecular stiffness is denoted by K_s. For $u_s < u_m \leq u_f$ the molecular behaviour is in a third and final stiffness stage, still linear elastic, but governed by a different stiffness value, indicated by K_m.

We assume as deterministic, and known, beside the value of $u_f^* = u_f - \bar{u}_m$, also (i) the two stiffnesses K_s and K_m, and (ii) the displacement interval s spanning the stiffness stage 2. Also the molecular diameter Φ_m is assumed as deterministic and known, of value $\Phi_m = 1.5$ nm; this value is assumed to remain constant during the deformation.

The assumed force-displacement law for a single tropocollagen molecule is then as follows:

$$
\begin{aligned}
&F_m = 0, \quad u_m \leq \bar{u}_m \text{ (entropic elasticity, neglected)}; \\
&F_m = K_s(u_m - \bar{u}_m), \quad \bar{u}_m < u_m \leq u_s \text{ (uncoiling)}; \\
&F_m = F_s + K_m(u_m - u_s), \quad u_s < u_m \leq u_f = (\bar{u}_m + u_f^*) \text{ (stretching)}; \\
&F_m = 0, \quad u_m > u_f \text{ (failed)},
\end{aligned} \tag{8}
$$

with

$$F_s = K_s s = K_s(u_s - \bar{u}_m). \tag{9}$$

One needs next to describe the mechanical behaviour of a full cable at the molecular level, assumed to run continuously from end to end of the considered collagen fibre. This subcomponent is made of a series of a number M of tropocollagen molecules, given by

$$M = \frac{L_{d,4}}{L_m} \gg 1, \tag{10}$$

which, accounting for (5), can also be written as

$$M = \frac{L_b}{L_m \prod_{i=1}^{4} y_i} = \frac{L_b}{L_m z_4}, \tag{11}$$

where the new random quantity z_4 was defined as

$$z_4 = \prod_{i=1}^{4} y_i, \quad 0 < z_4 \le 1. \tag{12}$$

In the lack of precise information, it is assumed that the molecules are connected sequentially in a line which, however, has a waviness whose statistical properties are independent from those of a single molecule; furthermore, it is assumed that the polymerisation along the whole collagen fibre is equal to that of the molecule itself, and that both the stiffness and strength of the connection between molecules are the same as those of the molecule itself.

It is now possible to write the force-displacement equations for a single, continuous cable, at level 4, on the basis of the molecular equations (8), because the following hold:

$$u_4 = M u_m, \tag{13}$$

$$\bar{u}_4 = M \bar{u}_m, \tag{14}$$

$$u_4 - \bar{u}_4 = u_1 + L_b\left(1 - \frac{1}{z_4}\right), \tag{15}$$

(see (6)),

$$F_4 = F_m. \tag{16}$$

Hence, denoting by $F_{4,A}$ and $F_{4,B}$ the forces in molecular stiffness stages 2 and 3, respectively, one has:

$$F_{4,A} = K_s(u_m - \bar{u}_m) = \frac{K_s}{M}(u_4 - \bar{u}_4) = K_s L_m\left[\left(\frac{u_1}{L_b} + 1\right)z_4 - 1\right], \quad \bar{u}_4 < u_4 \le u_{s4}, \tag{17}$$

with $u_{s4} = M u_s$;

$$F_{4,B} = F_s + K_m(u_m - u_s) = F_s + \frac{K_m}{M}(u_4 - u_{s4})$$
$$= F_s + K_m L_m\left[\left(\frac{u_1}{L_b} + 1\right)z_4 - \left(1 + \frac{s}{L_m}\right)\right], \quad u_{s4} < u_4 \le M u_f; \tag{18}$$

and

$$F_4 = 0, \quad u_4 - \bar{u}_4 \le 0 \quad \text{or} \quad u_4 - \bar{u}_4 > M u_f^*. \tag{19}$$

From (17) and (18), it becomes apparent that the only random quantity that governs the mechanical behaviour of each cable at level 4 is z_4, defined by (12). The probability density function of z_4 cannot be defined in closed form, but it is assumed to be also a beta function, with known mean value and variance, that can be computed, for the product of stochastically independent random variables, exploiting the following expressions:

$$\text{if } x = y_i y_j, \quad \text{then } E(x) = E(y_i) E(y_j); \tag{20}$$

$$\text{if } x = y_i y_j, \quad \text{then } \text{Var}(x) = [E(y_i)]^2 \text{Var}(y_j) + [E(y_j)]^2 \text{Var}(y_i) + \text{Var}(y_i) \text{Var}(y_j) \tag{21}$$

(see for instance [Goodman 1960; 1962]).

Denoting now by $f_{z_4}(z_4)$ the probability density function for z_4, the expected value of F_4, for each assigned value of the collagen fibre displacement u_1, must be computed through an integration over the admissible values of z_4, as follows:

$$E[F_4(u_1, z_4)] = \int_{0 < z_A \leq 1}^{0 < z_B \leq 1} F_{4,A}(z_4) f_{z_4}(z_4) \, dz_4 + \int_{0 < z_B \leq 1}^{0 < z_C \leq 1} F_{4,B}(z_4) f_{z_4}(z_4) \, dz_4 \tag{22}$$

The integration limits z_A, z_B, and z_C, all deterministic, are to be computed as follows:

- from (15) and (19) one has

$$F_{4,A} \neq 0 \quad \text{if} \quad u_1 + L_b\left(1 - \frac{1}{z_4}\right) > 0 \quad \Longrightarrow \quad z_4 > \frac{L_b}{u_1 + L_b} = z_A; \tag{23}$$

- from (17) it is seen that the transition from $F_{4,A}$ to $F_{4,B}$ occurs for $u_4 = u_{s4}$, i.e., for

$$u_4 = M u_s = \bar{u}_4 + M s, \tag{24}$$

which, recalling (11) and again (15), gives

$$z_B = \frac{L_b}{u_1 + L_b}\left(1 + \frac{s}{L_m}\right); \tag{25}$$

- and from (11), (15), and (18) one has

$$F_{4,B} \neq 0 \quad \text{if} \quad u_1 + L_b\left(1 - \frac{1}{z_4}\right) < \frac{L_b}{L_m z_4} u_f^* \quad \Longrightarrow \quad z_4 < \frac{L_b}{u_1 + L_b}\left(1 + \frac{u_f^*}{L_m}\right) = z_C. \tag{26}$$

Note that, in order to account for the irreversibility of failure, in the calculation of integral (22) the upper integration limit z_C can not increase with increasing u_1, i.e., one must always set $dz_C/du_1 \leq 0$.

It is now possible to introduce into the previous equations some simple modifications in order to account for the possible presence of crosslinking. For this complex aspect, no attempt is made here at describing any physical feature of the substructural arrangement. The purpose is to model the main mechanical effects of crosslinking in a phenomenological way, through equations void of physical meaning, but as simple as possible.

The main effects of crosslinking considered herein are (i) the increase of the apparent stiffness of a single cable (see, for instance, [Thompson and Czernuszka 1995]); (ii) the influence of the brittle failure of a cable on the surrounding ones.

The first effect is described in a trivial way: the basic molecular stiffnesses, K_s and K_m, are introduced into the governing equations each multiplied by an independent dimensionless factor, denoted by $X_{ks} \geq 1$ and $X_{km} \geq 1$ respectively.

The second effect of crosslinking is recognised to be of reducing the failure displacement of the whole collagen fibre. Such a reduction is quite significant, according to [Pins et al. 1997]: non-crosslinked fibres are reported to fail at a strain (probably Biot, although this is not reported in [Pins et al. 1997]) that can reach values up to 0.68, whereas crosslinked ones fail at strains of the order of 0.15. This phenomenon could be explained considering that brittle failure is associated to a sudden release of elastic energy: if the failed cable is crosslinked to other parallel cables, the surrounding ones might absorb a portion of the released energy, and fail themselves, thus leading to a premature failure of the whole collagen fibre.

This effect has been taken into account by defining a progressive reduction of the upper integration limit in (22), i.e., z_C of (26). This reduction is proportional to the current value of the input displacement u_1 through a new nondimensional parameter $X_f \geq 0$. We have redefined z_C as follows:

$$z_C = z_{C,0} - f(X_f, u_1), \quad \frac{dz_C}{du_1} \leq 0, \quad \text{with} \quad z_{C,0} = \frac{L_b}{u_1 + L_b}\left(1 + \frac{u_f^*}{L_m}\right), \tag{27}$$

and with

$$f(X_f, u_1) = \frac{2\arctan(u_1 X_f/L_b)(z_{C,0} - z_A)}{\pi}. \tag{28}$$

These equations, which have no physical basis, when inserted into the governing equations allow one to obtain the desired effect: with increasing u_1, the upper integration limit z_C tends to approach the lowest one, z_A. This reflects the progressive disappearance, among the various subcomponents, of the shorter ones, at a rate that increases with increasing values of the parameter X_f.

The expected value of the axial stress in a cable at level 4, i.e., in a cable made by a sequence of tropocollagen molecules, for a given value of the collagen fibre displacement u_1, is then

$$E(\sigma_4) = \frac{E(F_4)}{A_m} = \frac{4E(F_4)}{\pi\,\Phi_m^2}. \tag{29}$$

Elementary homogenisation theory is finally exploited to compute the corresponding expected value of the macroscopic axial stress in the collagen fibre at level 0 of the assumed hierarchy, as shown in Figure 1. At each level, in fact, the stress-carrying subfibrils coexist with noncontinuous subfibrils, with some extra-fibrous (ground) matter, and with no matter at all.

Denote by σ_i^e the tensile stress possibly transmitted by the nonfibrous matter at each level i, and by f_i the volume fraction of stress-carrying fibrous matter at each level i. Then $f_i = A_i^f/A_i$, where A_i is the total area of a cable at level i, and A_i^f is the area occupied by continuous fibrous matter in that very cable. Then the elementary homogenisation theory allows one to calculate the average macroscopic stress σ_0 at level 0 as follows:

$$\sigma_0 = E(\sigma_4)f_3 f_2 f_1 f_0 + \sigma_3^e(1 - f_3)f_2 f_1 f_0 + +\sigma_2^e(1 - f_2)f_1 f_0 + \sigma_1^e(1 - f_1)f_0 + \sigma_0^e(1 - f_0). \tag{30}$$

From now on, for simplicity, we always assume that the extra-fibrous matter does not carry any mechanical stress in tension, even though it could do so in compression. Therefore, we will set $\sigma_i^e = 0$ for each

$i = 0, \ldots, 3$ in (30), which then reduces to

$$\sigma_0 = E(\sigma_4) f_3 f_2 f_1 f_0, \tag{31}$$

with $E(\sigma_4)$ given by (29), with (22) and following. This is an explicit expression for the axial stress in a single stretched collagen fibre for any corresponding value of the prescribed value of u_1; this last could be related to any conventional strain value through standard theory.

We note, finally, that the obtained stress-stretch equation, here derived explicitly for the case of $N = 4$, could be easily extended to any other structural component, biological or not, having the same type of microstructure of nested wavy cables, with any number N of subcomponents. Once the mechanical properties of the most microscopic level — i.e., level N — are known, a straightforward extension of the above equations will furnish the desired stress-stretch relationship. The only statistics to be described would be that of a variable z_N, defined as the product of the N random variables y_i, defined by (4). The expression for the average macroscopic stress that extends result (30) to an arbitrary number N of sublevels is the following:

$$\sigma_0 = E(\sigma_N) \prod_{i=0}^{N-1} f_i + \sum_{i=0}^{N-1} \left[\sigma_i^e (1 - f_i) \prod_{j=0}^{i-1} f_j \right]. \tag{32}$$

The proposed stress-stretch equation, with the force-displacement law of (17) and (18), and with the modifications of (27) and (28), included to account for crosslinking, requires a total number of constitutive parameters equal to $7 + 3N$ in general, and equal to 19 for the case $N = 4$.

3. Applicative examples

3.1. *Sea cucumber collagen fibril, from* [Eppell et al. 2006]. The first example considers a collagen *fibril*, i.e., the subcomponent at level 1 of the hierarchy considered so far. Therefore, to obtain the corresponding results one must adopt $N = 3$, and the molecular level corresponds now to $i = 3$ in (5) and (6). This example was chosen both because it helps in setting a basis for the data concerning the statistics at the lower levels of a fibre, and because there are experimental results available [loc. cit.].

Figure 6 shows tensile stress-strain curves: one as presented in [loc. cit.] (continuous), the other (with white circles) as obtained from the analytical approach proposed here. In this case, unlike all the remaining ones, the molecular length L_m has been set equal to $L_m = 204.9$ nm, instead of the commonly adopted value $L_m = 301.7$ nm, following the results presented in [loc. cit.]. We note (we will return to this in the next section) that a substantial uncertainty about experimentally measured quantities exists already for the "simple" molecular length L_m. The Almansi strain employed for the abscissa, as done in [loc. cit.], is defined as

$$\varepsilon_{\text{Almansi}} = \frac{\lambda^2 - 1}{2\lambda^2}, \quad \lambda = \frac{L_b + u_1}{L_b}. \tag{33}$$

Table 1 shows the set of parameters adopted to obtain the analytical results for this and the next three examples. The first ten parameters have values that will remain fixed in all the presented examples; the remaining nine will have different values for each example. Note that, for (31), we have not defined individual values for the stress-carrying fibrous matter volume fractions f_i, but rather a single value for

Material parameter	Sea cucumber fibril [Eppell et al. 2006]	Engineered [Gentleman et al. 2003]	Rat tail [Gentleman et al. 2003]	Rabbit patellar tendon [Yamamoto et al. 1999]
$E(y_2)$	0.9952	0.9952	0.9952	0.9952
$E(y_3)$	0.99779	0.99779	0.99779	0.99779
$E(y_4)$	0.9979	0.9979	0.9979	0.9979
$\mathrm{Var}(y_2)$	$4.9 \cdot 10^{-5}$	$4.9 \cdot 10^{-5}$	$4.9 \cdot 10^{-5}$	$4.9 \cdot 10^{-5}$
$\mathrm{Var}(y_3)$	$6.561 \cdot 10^{-7}$	$6.561 \cdot 10^{-7}$	$6.561 \cdot 10^{-7}$	$6.561 \cdot 10^{-7}$
$\mathrm{Var}(y_4)$	$2.5027 \cdot 10^{-6}$	$2.5027 \cdot 10^{-6}$	$2.5027 \cdot 10^{-6}$	$2.5027 \cdot 10^{-6}$
$\prod f_i$	0.0768	0.05	0.05	0.05
K_s (pN/nm)	10	10	10	10
K_m (pN/nm)	30	30	30	30
Φ_m (nm)	1.5	1.5	1.5	1.5
L_m (nm)	204.9	301.7	301.7	204.9/301.7
u_f^* (nm)	265	167	167	75
$E(y_1)$	-	0.99	0.99	0.99
$\mathrm{Var}(y_1)$	-	$1.7742 \cdot 10^{-4}$	$1.7742 \cdot 10^{-4}$	$8.281 \cdot 10^{-5}$
L_b (mm)	5	76	76	15
X_{ks}	1.8	3.64	15	6.5
X_{km}	5	2.25	2	1
X_f	0.12	9.85	6.8	15
s (nm)	115	23	32	5

Table 1. Values adopted for the material parameters of the collagen fibril and collagen fibres.
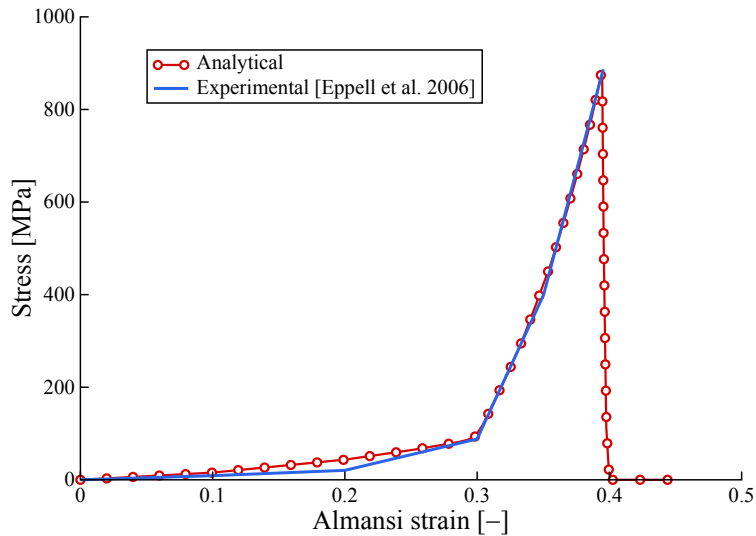
Figure 6. Stress-strain curves in uniaxial tension for the collagen fibril studied in [Eppell et al. 2006]. The blue curve is experimental [loc. cit.]; the red curve is obtained from the proposed equations. The Almansi strain is defined as in (33). Material data as in Table 1.

their product, based on the considerations presented in Section 4. A good agreement between experimental and analytical results could be found for this special example. The analytical result provides the expected value for the fibril stress; for this example, the peak stress expected value is 884 MPa, to which a predicted standard deviation of 4157 MPa corresponds.

3.2. *Engineered collagen fibre, from* [Gentleman et al. 2003]**.** The next example concerns the engineered collagen fibre studied in [loc. cit.]. Figure 7 shows tensile stress-strain curves: one as presented in [loc. cit.], and the others as obtained from the proposed analytical approach. The Biot strain in the abscissa — the same adopted in [loc. cit.] — is defined as

$$\varepsilon_{\text{Biot}} = \frac{u_1}{L_b}. \tag{34}$$

A good agreement between experimental results and analytical predictions can be observed. In this case, the peak stress expected value is 70.8 MPa, and the corresponding standard deviation is 419.5 MPa.

The other curves, with white markers, refer to analytical results obtained from different choices of material parameters, in order to provide a brief sensitivity analysis: each curve refers to the modification of a single parameter, with respect to those listed in Table 1. The following effects, easy to predict on the basis of the meaning of the considered parameters, are visible:

- a reduction of the molecular failure displacement, u_f^*, causes a reduction of both the global peak stress and strain, leaving the overall shape of the stress-strain curve unaltered;

- a reduction of the size of stage 2 of the molecular stiffness, through parameter s (see Figure 5), causes a corresponding increase of the overall stiffness, as well as of the global peak stress;
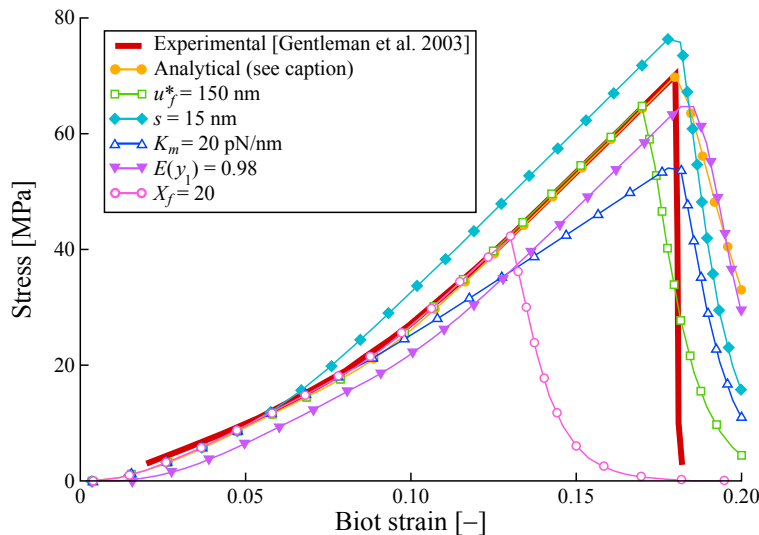
Figure 7. Stress-strain curves in uniaxial tension for the engineered collagen fibre studied in [Gentleman et al. 2003]. The solid curve is experimental, from [loc. cit.]; all the other curves, with markers, are obtained from the proposed equations. The Biot strain is defined in (34). Material data as in Table 1.
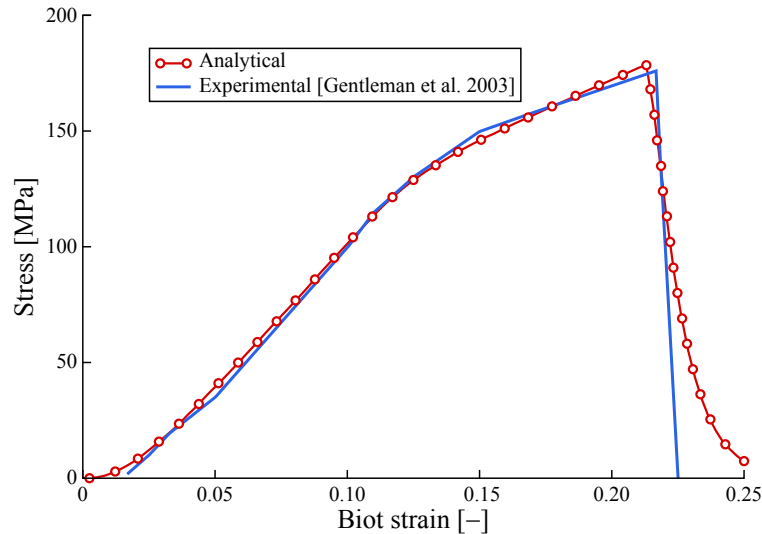
Figure 8. Stress-strain curves in uniaxial tension for the rat tail collagen fibre studied in [Gentleman et al. 2003]. The solid curve is experimental, from [loc. cit.]; the curve with circles is obtained from the proposed equations. Material data as in Table 1.

- a reduction of the molecular stiffness K_m has the opposite effect;
- a reduction of the expected value for the variable y_1 of (4) causes a change of shape of the stress-strain curve, as well as a reduction of the peak stress for the fibre;
- an increase of the parameter X_f causes a significant loss of ductility, as expected.

The model is relatively insensitive to small variations of the variances for the single variables y_i of (4).

3.3. *Rat tail tendon collagen fibre, from* [Gentleman et al. 2003]. Figure 8 shows a similar comparison, concerning now a single collagen fibre extracted from a rat tail tendon, as reported in [loc. cit.]. In this case, the peak stress expected value is 178.7 MPa, and the corresponding standard deviation is 1049 MPa.

3.4. *Rabbit patellar tendon sample, from* [Yamamoto et al. 1999]. Figure 9 illustrates results similar to the previous ones for a collagen fibre taken from a rabbit patellar tendon, for which experimental results are provided in [loc. cit.]. The figure shows two analytical curves, of which only the one adopting $L_m = 204.9$ nm, as done for the fibril example, corresponds well to the experimental result. In this case, the peak nominal stress (nominal stresses are shown in [loc. cit.]) expected value is 19.62 MPa, and the corresponding standard deviation is 116 MPa.

3.5. *Periodontal ligament sample, from* [Genna et al. 2008]. Figure 10 shows again a stress-strain plot, that now concerns the behaviour in tension of a small sample of swine periodontal ligament (PDL). The details of the sample and of the testing modalities are described in [loc. cit.]. In this case, the experiment concerns a tissue, not a single collagen fibre, and one has only an indirect validation of the model proposed herein.
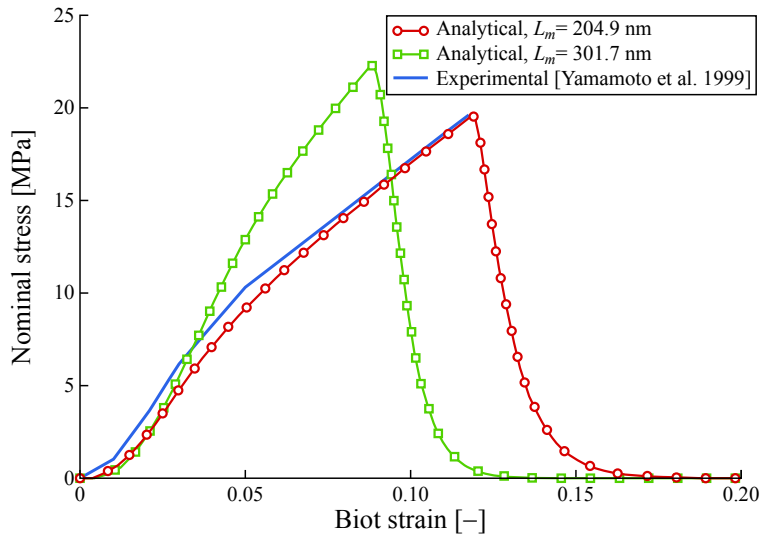
Figure 9. Stress-strain curves in uniaxial tension for the rabbit patellar collagen fibre studied in [Yamamoto et al. 1999]. The solid curve is experimental, from [loc. cit.]; the curves with markers are obtained from the proposed equations, and refer to different molecular lengths L_m as indicated. The nominal stress is force divided by initial cross-section area. Material data as in Table 1.
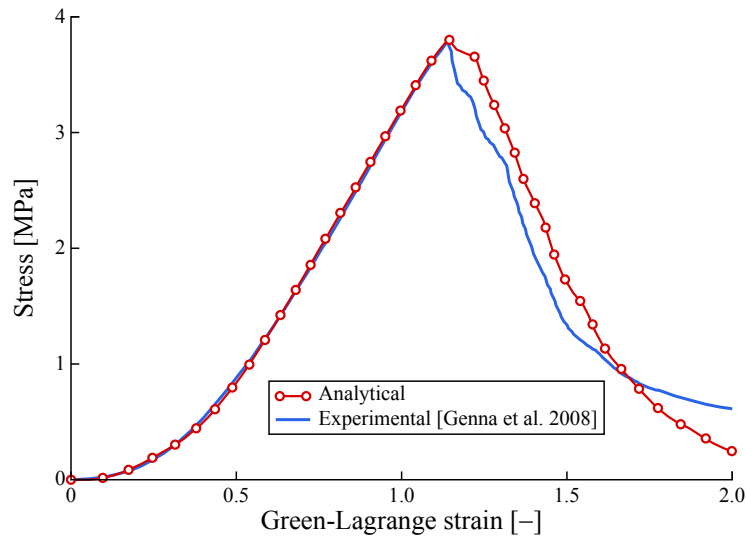
Figure 10. Stress-strain curves in uniaxial tension for one of the periodontal ligament samples studied in [Genna et al. 2008]. The solid curve is experimental, from [loc. cit.]; the curve with circles is obtained by means of the model of [Genna 2006], in which the equations developed in the present work have been inserted for the behaviour in tension of a single collagen fibre. The Green–Lagrange strain is defined as in (35) of the text. Material data as in Table 2.

The Green–Lagrange strain plotted in abscissa in Figure 10, as adopted in [loc. cit.], is defined as

$$\varepsilon_{GL} = \frac{1}{2}\left[\left(\frac{L_b + u_1}{L_b}\right)^2 - 1\right]. \tag{35}$$

In this case, (31) is inserted into an interface model, presented in [Genna 2006], that allows one, by means of yet another statistical integration over the waviness of the collagen fibres, to describe the tissue features. The accompanying paper [Genna and Paganelli 2014] makes extensive use of this model for studying the extraction of a tooth from its socket; we refer to [Genna 2006] and [Genna and Paganelli 2014] for more details of the interface description.

The main parameters required by the PDL model of [Genna 2006] are:

- the thickness w_0 of the PDL layer;

- the angle β_0 that defines the inclination of the collagen fibres in a longitudinal section of the tooth;

- the angle θ_0 that defines the inclination of the collagen fibres in a transversal section of the tooth;

- the volume fraction f_c of stress-carrying collagen fibres inside the PDL;

- statistical properties of the collagen fibres waviness in the PDL, described by the variable x_c which is the ratio between the uncoiled, unstretched length of a collagen fibre and its end-to-end distance at rest, governed by w_0, β_0, and θ_0;

- data for the constitutive law of a single collagen fibre, that here correspond to the 19 parameters required by the proposed stress-stretch model;

- other parameters that define the compressive behaviour of the PDL, of no interest here.

Table 2 reports all the relevant data adopted to obtain the result shown in Figure 10. In Table 2 the parameter L_b, denoting the uncoiled length of a collagen fibre at rest, is marked as a random variable, since its value now depends on the statistics of the waviness of the fibre, i.e., on the current values of x_c during the integration process.

$E(y_2)$	0.9952	u_f^*	167 nm	w_0	0.66 mm
$E(y_3)$	0.99779	$E(y_1)$	0.995	β_0	34°
$E(y_4)$	0.9979	$\text{Var}(y_1)$	$1.2078 \cdot 10^{-4}$	θ_0	76.8°
$\text{Var}(y_2)$	$4.9 \cdot 10^{-5}$	L_b	random variable	f_c	0.05
$\text{Var}(y_3)$	$6.561 \cdot 10^{-7}$	X_{ks}	1	$E(x_c)$	1.093
$\text{Var}(y_4)$	$2.5027 \cdot 10^{-6}$	X_{km}	1	$\text{Var}(x_c)$	0.00397
$f_0 f_1 f_2 f_3$	0.05	X_f	0		
K_s	10 pN/nm	s	50 nm		
K_m	30 pN/nm				
Φ_m	1.5 nm				
L_m	301.7 nm				

Table 2. Adopted values for the material parameters of the periodontal ligament sample studied in [Genna et al. 2008].
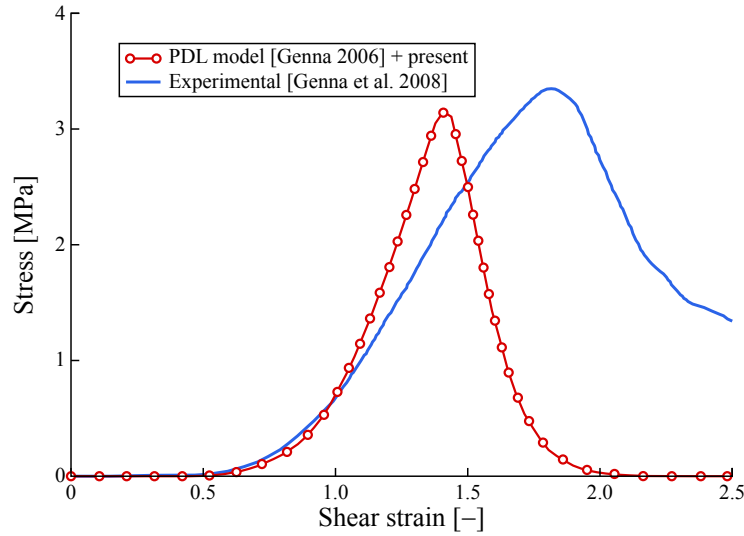
Figure 11. Stress-strain curves in shear for one of the periodontal ligament samples studied in [Genna et al. 2008]. The solid curve is experimental, from [loc. cit.]; the curve with circles is obtained by means of the model of [Genna 2006], in which the equations developed in the present work have been inserted for the behaviour in tension of a single collagen fibre. The shear strain is defined as the ratio between the displacement and the width at rest of the sample. Material data as in Table 2 except for $w_0 = 0.33$ mm and $\beta_0 = -7°$.

It is worth remarking, here, that the failure Biot strain of a single collagen fibre, with the data adopted to obtain the result of Figure 10, is $\varepsilon_f \approx 0.55$. As already observed, this quite large value is an indication of the probable lack of crosslinking in the PDL collagen.

Finally, Figure 11 shows a comparison obtained in the same way as the previous one, but on a different swine PDL sample, and for a different type of loading, i.e., shear in a plane normal to the tooth axis [Genna et al. 2008]. The curves in Figure 11 show a shear stress in ordinate, and, in abscissa, a shear strain defined as the ratio between the shear displacement and the width w_0 of the PDL sample. For this case the adopted data are the same as in Table 2, with the exception of w_0 and β_0, which are now $w_0 = 0.33$ mm and $\beta_0 = -7°$.

4. Discussion

A main source of difficulty for the model proposed here is the choice of the material parameter values. Results of a detailed sensitivity analysis, beside what was shown in Figures 7 and 9, are not reported here for the sake of brevity.

All the data concerning the statistics of the quantities y_i of (4), shown in Tables 1 and 2, have been rederived following the same approach adopted in [AG]. A partial confirmation of their usability derives from the result shown in Figure 6, which refers to a subcomponent of the fibres.

A precise evaluation of the volume fractions f_i of stress-carrying cables at the various sublevels can hardly be given. The following approach was therefore followed: a single cable at level i is assumed to

have a circular cross-section; fibrous matter is assumed to be present in cables, at level $i + 1$, also having a circular cross-section. For a full packing of infinite equal circles, the volume fraction of fibrous matter would be equal to $\pi/\sqrt{12} \approx 0.907$, at each sublevel. Assuming a large but finite number of internal circles, one can adopt a smaller value, that we chose equal to 0.85. Furthermore, it was necessary to define what part of the fibrous subcomponents, at each level, was continuous, i.e., stress-carrying: we assumed that only one half of the fibrous matter was continuous, thus obtaining a value $f_i \approx 0.425$. Therefore, one finds $f_0 f_1 f_2 f_3 \approx 0.425^4 = 0.033$, rounded to $f_0 f_1 f_2 f_3 = 0.05$, and $f_1 f_2 f_3 = 0.0768$ for the fibril, with $N = 3$, as shown in Tables 1 and 2.

More difficulties arise in defining several molecular parameters. We started by reasoning on the case of the periodontal ligament (PDL), in order to exclude the effects of crosslinking: in this tissue, in fact, the stress-carrying fibres seem to behave as if little or no crosslinking at all were present. This could be inferred from (i) the very low stiffness values, and the very large failure strains, compared to other tissues, observed in PDL samples [AG], and (ii) as said in Section 3.3, from the high value of the single fibre failure strain. No quantitative description of this aspect could be found; [Berkovitz et al. 1995] reports that PDL has "unique" crosslinking features, with respect to all other tissues, but no information is given about the relevance of this property with respect to mechanical behaviour.

Thus, the stress-carrying collagen fibres of the PDL were assumed to be uncrosslinked. This implies, in the approach illustrated here, to adopt $X_{ks} = X_{km} = 1$ and $X_f = 0$, which allows one to reason about raw molecular data.

In order to obtain a good match with the experimental result in tension of Figure 10, the values $K_s = 10\,\text{pN/nm}$, $K_m = 30\,\text{pN/nm}$, $u_f^* = 167\,\text{nm}$, and $s = 50\,\text{nm}$ were adopted (see Table 2).

The displacement values agree reasonably well with the corresponding ones reported in [Buehler and Wong 2007], which are $u_f^* = 150\,\text{nm}$ and $s = 90\,\text{nm}$. On the contrary, the molecular stiffness ones do not, since our K_m is ten times smaller than the one obtained in [Buehler and Wong 2007], and K_s is about 1/5. It is extremely difficult to obtain coherent information about these data from the literature, for several reasons. A relationship exists that relates the bending stiffness of a tropocollagen molecule to its persistence length, but this seems to hold for the entropic regime only, neglected here. Another relationship which provides the molecular stiffness in the stretching range derives from standard truss theory, and is

$$K_m = \frac{E_m A_m}{L_m}, \tag{36}$$

where E_m denotes the molecule Young modulus. According to several sources (see, for instance, [Gautieri et al. 2012]), the Young modulus of a collagen molecule takes values in the range $E_m = 300$–$16000\,\text{pN/nm}^2$ (i.e., MPa), depending both on the evaluation modalities and on the considered strain rate, both in experiments and in numerical simulations based on molecular dynamics theory.

Adopting an average value $E_m = 5000\,\text{pN/nm}^2$, equation (36) yields $K_m = 29.98\,\text{pN/nm}$. On the other hand, a value $E_m = 5000\,\text{pN/nm}^2$ hardly agrees with further data reported in [Buehler and Wong 2007], where the bending stiffness of a single molecule is reported to vary between $E_m I_m = 1.247 \times 10^{-29}\,\text{Nm}^2$ and $E_m I_m = 1.2 \times 10^{-28}\,\text{Nm}^2$, depending on the assumed strain rate, I_m denoting the molecule moment of inertia around its neutral axis. Assuming for the molecule a circular cross-section with diameter $\Phi_m = 1.5\,\text{nm}$, the first value corresponds to $E_m \approx 50\,\text{pN/nm}^2$, and the second to $E_m \approx 500\,\text{pN/nm}^2$.

On yet another hand, in order to obtain the stiffness value $K_m = 294.8\,\text{pN/nm}$ proposed in [Buehler and Wong 2007] for the molecular stretching regime, (36) would require a value $E_m \approx 50000\,\text{pN/nm}^2$, well outside the reported range of values. This uncertainty on the value of K_m may arise from the intrinsic measurement difficulties, from confusion between entropic and energetic behaviour, from presence/absence of crosslinking, strain-rate effects, solvated/dry conditions during the test, and so on.

In order to obtain results from the stress-stretch model proposed in this work, it was arbitrarily decided to assume as valid the average value $E_m = 5000\,\text{pN/nm}^2$, which corresponds to $K_m \approx 30\,\text{pN/nm}$, for the uncrosslinked, basic molecular stiffness. All the choices for the molecular parameters are made very difficult by the lack of reliable experimental results; even the basic molecular length L_m does not see agreement on its values (here we have been forced to adopt the values $L_m = 204.9\,\text{nm}$ or $L_m = 301.7\,\text{nm}$ in different cases.)

As for K_s, the molecular stiffness associated to the chain uncoiling, the situation is even less clear than for K_m. Its value could only be identified, and it was taken equal to $K_s = 10\,\text{pN/nm}$, in a proportion to K_m about twice as that indicated in [Buehler and Wong 2007].

The numerical values of the three parameters X_{ks}, X_{km}, and X_f, that govern crosslinking, in the results of Figures 7, 8, and 9, had to be identified case by case.

As for the last rows in Table 2, that concern the data defining the PDL behaviour, we refer to [Genna 2006], except for f_c of Section 3.3. In [loc. cit.] every single collagen fibre was supposed to run continuously from end to end of the PDL layer, and the value for the fibre volume fraction f_c was taken from the literature as equal to $f_c = 0.5$. Recent work [Trombetta and Bradshaw 2010] confirms that $f_c = 0.5$ is a reasonable estimate of the average value for the volume fraction of the fibrous component in the PDL. In the new model, only the stress-carrying portion of it is considered, which, at least according to available images of the PDL, is only a small fraction of the total. In order to obtain a good match with the experimental stress-strain results, the value $f_c = 0.05$ had to be adopted, as shown in Table 2.

An uncertainty remains about the shape of the stress-strain curves of both Figures 8 and 9, and the relevant material data, shown in Table 1. Work by Gutsmann et al. [2004] suggests that a plateau in the stress-strain curve of collagen might be due to crosslinking; the model proposed here might reproduce this effect through the reduction of the upper integration limit z_C ((27) and (28)), for increasing displacement u_1, until the stiffer portion of the molecular behaviour disappears from the picture. Nevertheless, with the set of material parameters herein adopted, and especially in view of the narrow extension of the molecular force-displacement law covered by the statistics of the variable z_4 of (12), it was impossible to obtain such an effect automatically. The only way to reproduce it was to adopt $X_{ks}K_s < X_{km}K_m$ as shown by Table 1, whose meaning remains unclear.

The simplicity of the model proposed herein allows one to consider any type of mechanical behaviour at the lowermost level — for instance, viscosity — with no conceptual difficulty.

Other considerations, similar to those already reported in [AG], remain still valid also for this modified, simplified, and improved version of the same approach.

5. Conclusions

No attempt has been made, here, to propose a complete and accurate representation of the physical microstructure of a single collagen fibre. The aim has been to obtain a simple and engineering-usable

(for instance, in large-scale 3D finite element calculations) set of equations that describe the nonlinear mechanical behaviour of this important biological component, based on a set of parameters having, where possible, a clear physical meaning. Several features of the real arrangement of subcomponents are explicitly taken into account, but several other important details still require more study. The ability to reproduce experimental results on the basis of reasonable values of the material parameters is however encouraging. An accompanying paper [Genna and Paganelli 2014] illustrates the performance of the model presented herein in the context of finite element simulations at the macroscopic scale.

References

[Annovazzi and Genna 2010] L. Annovazzi and F. Genna, "An engineering, multiscale constitutive model for fiber-forming collagen in tension", *J. Biomed. Mater. Res. A* **92A**:1 (2010), 254–266.

[Berkovitz et al. 1995] B. K. B. Berkovitz, B. J. Moxham, and H. N. Newman, *The periodontal ligament in health and disease*, 2nd ed., Mosby-Wolfe, London, 1995.

[Bozec and Horton 2005] L. Bozec and M. Horton, "Topography and mechanical properties of single molecule of type I collagen using atomic force microscopy", *Biophys. J.* **88**:6 (2005), 4223–4231.

[Buehler and Wong 2007] M. J. Buehler and S. Y. Wong, "Entropic elasticity controls nanomechanics of single tropocollagen molecule", *Biophys. J.* **93**:1 (2007), 37–43.

[Bustamante et al. 2000] C. Bustamante, S. B. Smith, J. Liphardt, and D. Smith, "Single-molecule studies of DNA mechanics", *Curr. Opin. Struct. Biol.* **10**:3 (2000), 279–285.

[Cacho et al. 2007] F. Cacho, P. J. Elbischger, J. F. Rodriguez, M. Doblaré, and G. A. Holzapfel, "A constitutive model for fibrous tissues considering collagen fiber crimp", *Int. J. Non-Linear Mech.* **42**:2 (2007), 391–402.

[Eppell et al. 2006] S. J. Eppell, B. N. Smith, H. Kahn, and R. Ballarini, "Nano measurements with micro-devices: Mechanical properties of hydrated collagen fibrils", *J. R. Soc. Interface* **3**:6 (2006), 117–121.

[Gautieri et al. 2012] A. Gautieri, S. Vesentini, A. Redaelli, and M. Buehler, "Viscoelastic properties of model segments of collagen molecules", *Matrix Biol.* **31**:2 (2012), 141–149.

[Genna 2006] F. Genna, "A micromechanically-based, three-dimensional interface finite element for the modelling of the periodontal ligament", *Comput. Methods Biomech. Biomed. Engin.* **9**:4 (2006), 243–256.

[Genna and Paganelli 2014] F. Genna and C. Paganelli, "Force–displacement relationship in the extraction of a porcine tooth from its socket: Experiments and numerical simulations", *J. Mech. Mater. Struct.* **9**:5 (2014), 497–514.

[Genna et al. 2008] F. Genna, L. Annovazzi, C. Bonesi, P. Fogazzi, and C. Paganelli, "On the experimental determination of some mechanical properties of porcine periodontal ligament", *Meccanica* **43**:1 (2008), 55–73.

[Gentleman et al. 2003] E. Gentleman, A. Lay, D. Dickerson, E. Nauman, G. Livesay, and K. Dee, "Mechanical characterization of collagen fibers and scaffolds for tissue engineering", *Biomater.* **24**:21 (2003), 3805–3813.

[Goodman 1960] L. A. Goodman, "On the exact variance of products", *J. Amer. Stat. Assoc.* **55**:292 (1960), 708–713.

[Goodman 1962] L. A. Goodman, "The variance of the product of K random variables", *J. Amer. Stat. Assoc.* **57**:297 (1962), 54–60.

[Grytz and Meschke 2009] R. Grytz and G. Meschke, "Constitutive modeling of crimped collagen fibrils in soft tissues", *J. Mech. Behav. Biomed. Mater.* **2**:5 (2009), 522–533.

[Gutsmann et al. 2004] T. Gutsmann, G. Fantner, J. Kindt, M. Venturoni, S. Danielsen, and P. Hansma, "Force spectroscopy of collagen fibers to investigate their mechanical properties and structural organization", *Biophys. J.* **86**:5 (2004), 3186–3193.

[Kastelic et al. 1978] J. Kastelic, A. Galeski, and E. Baer, "The multicomposite structure of tendon", *Connect. Tissue Res.* **6**:1 (1978), 11–23.

[Limbert 2011] G. Limbert, "A mesostructurally-based anisotropic continuum model for biological soft tissues—decoupled invariant formulation", *J. Mech. Behav. Biomed. Mater.* **4**:8 (2011), 1637–1657.

[Petruska and Hodge 1964] J. Petruska and A. Hodge, "A subunit model for the tropocollagen macromolecule", *Proc. Nat. Acad. Sci. USA* **51**:5 (1964), 871–876.

[Pins et al. 1997] G. Pins, E. Huang, D. Christiansen, and F. Silver, "Effects of static axial strain on the tensile properties and failure mechanisms of self-assembled collagen fibers", *J. Appl. Polym. Sci.* **63**:11 (1997), 1429–1440.

[Ross 2004] S. M. Ross, *Introduction to probability and statistics for engineers and scientists*, 3rd ed., Academic Press, Burlington, MA, 2004.

[Thompson and Czernuszka 1995] J. I. Thompson and J. T. Czernuszka, "The effect of two types of cross-linking on some mechanical properties of collagen", *Biomed. Mater. Eng.* **5**:1 (1995), 37–48.

[Trombetta and Bradshaw 2010] J. M. Trombetta and A. D. Bradshaw, "SPARC/Osteonectin functions to maintain homeostasis of the collagenous extracellular matrix in the periodontal ligament", *J. Histochem. Cytochem.* **58**:10 (2010), 871–879.

[Wang et al. 1997] J. L. Wang, M. Parnianpour, A. Shirazi-Adl, and A. E. Engin, "Failure criterion of collagen fiber: Viscoelastic behavior simulated by using load control data", *Theor. Appl. Fract. Mech.* **27**:1 (1997), 1–12.

[Yamamoto et al. 1999] E. Yamamoto, K. Hayashi, and N. Yamamoto, "Mechanical properties of collagen fascicles from the rabbit patellar tendon", *J. Biomech. Eng.* (*ASME*) **121**:1 (1999), 124–131.

FRANCESCO GENNA: francesco.genna@unibs.it
Department of Civil Engineering, University of Brescia, Via Branze 43, I-25123 Brescia, Italy

■msp

FORCE–DISPLACEMENT RELATIONSHIP IN THE EXTRACTION OF A PORCINE TOOTH FROM ITS SOCKET: EXPERIMENTS AND NUMERICAL SIMULATIONS

FRANCESCO GENNA AND CORRADO PAGANELLI

Results of new investigations about the global tensile stiffness and strength of the periodontal ligament are presented. Experimental results are reported first, referring to the extraction of swine teeth from their sockets: force–displacement curves are shown, obtained from samples including a portion of the jaw and a canine swine tooth. Numerical simulations of the same tooth extraction tests are then presented, which exploit specific modelling techniques previously developed. In particular, use is made of an interface finite element capable to describe the fibrous structure of the periodontal ligament, and of a stress–stretch constitutive model, for a single collagen fibre, based on the multiscale nature of its subfibrillar microstructure. The comparison between the new experimental results and the numerical ones helps in understanding the soundness of the adopted mechanical models in the simulations. This study is expected to be mainly useful in providing results usable for the indirect validation of mechanical models of both the periodontal ligament and its basic constituent, the single collagen fibre.

1. Introduction

The periodontal ligament (PDL) is, among the components of the masticatory system, the one that most profoundly influences and determines the mechanical behaviour of the system itself. This is because the PDL is the most compliant component in this system, and because it exhibits a strongly anisotropic and nonlinear response to applied mechanical actions.

Dental mechanics is still singularly lacking systematic and extensive contributions to the study of the mechanical behaviour of the PDL, especially in humans. Some experimental results are available, concerned with the behaviour in tension of rat, bovine, or swine PDL (see, for instance, [Alatli et al. 1997; Pini et al. 2004; Dorow et al. 2003; Genna et al. 2008]). Some work exists concerning experiments on the viscous tensile/compressive behaviour of the PDL: most of it done on whole teeth, thereby making it difficult to isolate the purely mechanical contribution of the PDL [Qian et al. 2009; Papadopoulou et al. 2014], some on small samples with a relatively simple geometry [Sanctuary et al. 2005]. The dynamic viscoelastic shear behaviour of PDL has been studied experimentally in [Tanaka et al. 2007]. A review of the experimental work on PDL published until 2011 can be found in [Fill et al. 2011]. Nevertheless, a tremendous uncertainty still exists about even the simplest tensile behaviour of the PDL at constant, small loading velocity (appropriate, for instance, for orthodontic loading analyses), mainly due to the difficulty in defining reliable testing standards.

It is felt that more experimental work, possibly more systematic, should be performed, in order to obtain data useful both to dentists and to engineers. In this paper, the attention is mostly devoted to

mechanical aspects, and, in its first part, the results of some experiments will be presented, possibly useful to validate mechanical models. The results of these tests might also be useful in other related fields, such as the forced orthodontic extrusion of fractured roots, or other fractured root extraction processes.

A method for the experimental study of the PDL properties that might furnish information about its tensile stiffness and strength, but which might also provide some insight into a common activity in the dental field, could derive from the analysis of the force–displacement relationship obtained during the extraction of a tooth from its socket. Also this seemingly important aspect of dental mechanics has hardly been explored. Some results, in terms of forces only, are reported in [Chiba et al. 1980; Komatsu et al. 1990; Lehtinen and Ojala 1980; Ahel et al. 2006]. Nothing seems to exist in terms of displacements corresponding to applied forces. Numerical simulations of this process have been reported in [Gei et al. 2002] and [Genna 2006], but only as a way of verifying the performance of analytical models for the mechanical behaviour of the PDL, with no experimental results to be compared with.

The first direct purpose of this work is to provide information concerning experimentally determined force–displacement curves in the extraction of swine teeth from their sockets.

The second is to report the results given by the coupling of two separate models, developed previously, applied to the simulation of the extraction of teeth from their sockets, by means of the finite element method (FEM). The first model, illustrated in [Genna 2006], describes the PDL as a thin interface with a fibrous microstructure. The second model, proposed in an accompanying paper [Genna 2014], concerns a stress–stretch equation for a single collagen fibre, to be inserted as a basic ingredient into the first model. In its original version [Genna 2006], the interface model for the PDL made use of a simple, phenomenological equation for the stress–stretch behaviour of a single collagen fibre in tension, based on physically meaningless constitutive parameters. The model proposed in [Genna 2014], on the contrary, describes the mechanical behaviour of a collagen fibre in tension on the basis of constitutive parameters that, for the most part, have a precise physical meaning.

Both these models, for the single collagen fibre and for the PDL seen as a fibrous tissue, once fully developed and validated, could be of use for the study of several other situations of interest in biomechanics in general. With specific reference to dentistry, the first applications that come to the mind are orthodontic loading, analysis of centre of rotation, analysis of mechanical fields produced by several types of loading, both physiological and exceptional. Accurate information about the stress and strain fields produced by loading upon healthy teeth is expected to be of use also for the design of innovative dental implants, or similar devices, which should reproduce the physiological conditions much more closely than what happens with the currently used designs.

Finally, this work provides indirect information about the mechanical strength in tension of swine PDL, and, in general, about the dependence of the PDL mechanical behaviour in tension on several parameters, both mechanical and geometrical, that govern the analysed system.

2. Materials and methods

The experimental activity concerns the extraction of single-rooted swine canine teeth. All the tests have been run at the Dental Clinic of the University of Brescia, Italy. The testing machine was the Instron MicroTester 5848, an electromechanical instrument designed for uniaxial tests in biomechanical applications at low values of applied forces [Instron Corporation 2001].

Figure 1. A typical sample of a swine canine and surrounding portion of jawbone.

Forty-seven samples have been tested, obtained from portions of jaws of 12–15 month old swine. The choice of swine teeth derives from three main reasons:

- the Italian law forbids the use of human teeth for experimental research;
- after monkeys, pigs have the best compatibility with the human genome, and they have eating habits reasonably close to humans';
- the availability of freshly slaughtered material in the zone of Brescia.

Canines have been chosen so as to have roots as straight and smooth as possible, in order to facilitate the experimental procedure.

All the tested jaws have been taken within one hour from the slaughter of the animal. The portions including the canines have been cut (see Figure 1), polished of the largest possible portion of external soft tissues, immersed in physiologic solution, and put in a refrigerator at $+4.3°$ C for 24 hours. It was impossible to immediately run the tests, owing to the necessity of waiting for the nowadays-mandatory legal controls on the slaughtered animals before any research activity.

The jaw portions were clamped directly into the lower grips of the Instron MicroTester. The connection of the teeth to the testing machine was obtained by drilling a small hole, of 1.2 mm of diameter, into the tooth crown, therefore at a safe distance from the PDL, threading a metallic wire for orthodontic applications into it, and connecting the wire to the Instron grips by means of a steel part specifically designed. Figure 2 shows the final setup of a typical test.

The adopted wire type is made of a titanium alloy, with a rectangular cross-section of size 0.5334×0.635 mm (0.021×0.025 in). Preliminary tension tests on the wire gave an average material Young modulus equal to $E_t \approx 78000$ MPa.

It was not feasible, in the experimental arrangement devised so far, to always have a perfectly constant setup for the connecting wire, whose length was of about 50 mm, with possible small variations from test to test.

The smallness of the external portion of the tooth crown, together with the presence of residual soft tissues around the jawbone, made it impossible to connect an instrument capable of measuring the relative displacement between tooth and bone. Therefore, the only displacement measure available was the current distance between the machine grips.

Before extraction, each tooth was subjected to syndesmotomy, to a depth of 2 mm, using a Hu–Friedy syndesmotome. Without this preliminary operation, it was impossible to obtain a clean extraction, as either the wire, the tooth crown, or the jawbone broke prematurely.

The tests have been conducted prescribing the displacement of the upper grip in the machine, keeping the lower one fully fixed, at a rate of 2 mm/min. Forces have been measured with a uniaxial load cell with range of ± 2 kN.

3. Numerical models

The extraction process performed experimentally has been simulated by means of nonlinear FEM analyses. Several geometries of a tooth plus a surrounding portion of the jawbone have been considered, some of which describe swine canine teeth and others human incisors or two-rooted molars.

Figure 2. The testing setup.

3.1. *Numerical techniques.* All the numerical analyses have been run adopting the FEM as implemented in the partially open commercial code ABAQUS [Hibbitt et al. 2013].

After an initial geometrically nonlinear step, in which the initial slack of the titanium alloy wire is recovered, a second step applies traction to the tooth in a regime of small displacements, confining the geometrical nonlinearity to the formulation of the interface element for the PDL.

An interface finite element has been developed and coded into a Fortran 90 user subroutine UMAT to describe the nonlinear behaviour of the PDL, as proposed in [Genna 2006]. Each element is defined by six nodes, three of which are shared with a tetrahedral element describing the jawbone, and the other three with the adjacent tetrahedral element describing the tooth root. The nodal displacements are defined in a local reference system $n - t_1 - t_2$, where n is orthogonal to the bone surface, directed from bone to tooth root; t_1 is orthogonal to n and lies in a plane defined by n and the main axis of the tooth root; t_2 forms a right-handed reference system with the first two axes. The initial thickness of the PDL layer is denoted by w_0. Figure 3 shows both a sketch of a generic interface element and the microstructural arrangement underlying the assumed mechanical behaviour.

Figure 3. Sketch of the geometrical arrangement of the interface finite element for the description of the periodontal ligament. Left: nodes, intrinsic reference system, Gauss points. Right: diagram of the two wavy cables that define, at each Gauss point, the mechanical behaviour of the tissue.

At each of the three Gauss points of each interface element, the mechanical behaviour is governed by the existence of two cables. Both are inclined, in the undeformed configuration, by an angle β_0 with respect to the n axis, in the $n - t_1$ plane, and by an angle $\pm\theta_0$ with respect to the t_2 axis, in the $n - t_2$ plane. In this way, at each Gauss point the two cables are arranged into an X-shaped configuration in a transverse plane; this provides a torsional stiffness even for small displacements, since, upon the application of a torque around the main axis of the tooth, one of the two cables starts elongating immediately (see [Genna 2006]).

Each cable, in this model, represents a large random number of collagen fibres, having a wavy geometry at rest; the uncoiled, unstretched length of a single collagen fibre is denoted by L_b, which will be assumed to be a random variable. Each fibre starts furnishing an axial stiffness only when it is fully uncoiled; bending stiffness contributions of the fibres are neglected. The definition of the PDL compressive behaviour is obtained by a phenomenological equation devoid of physical meaning, and of no interest here.

Denote by l_0 the end-to-end distance between the extremities of each coiled fibre in the unstretched configuration, i.e.,

$$l_0 = w_0 \sqrt{1 + \tan^2 \beta_0 + 1/\tan^2 \theta_0}. \tag{1}$$

Then the nondimensional variable x_c is introduced, defined as

$$x_c = \frac{L_b}{l_0}, \quad x_c \geq 1, \tag{2}$$

and assumed to be a random variable, whose probability density function $f_{x_c}(x_c)$ is here assumed to be of the gamma type, with known expected value and variance.

In order to obtain an expression for the expected value of the total macroscopic stress in each Gauss point of each interface element, for a given vector δ of displacement jumps defined in the local reference system, the forces F_1 and F_2 existing in the two cables are computed through a statistical integration

over the admissible values taken by the random variable x_c of (2); i.e., denoting by $l_i(\delta)$, $i = 1, 2$, the current, stretched length of each cable, for $l_i(\delta) > L_b$, we have

$$F_i(\delta) = A_i \int_1^{l_i/l_0} \sigma_i(x_c, \delta) f_{x_c}(x_c) \, dx_c, \quad i = 1, 2, \tag{3}$$

where $\sigma_i(x_c, \delta)$ indicates the local stress in a single collagen fibre for a given value of the displacement vector δ, and A_i indicates the cross-section area covered by all the fibres.

From (3), simple analytic developments lead to explicit expressions for the normal and shear stresses at each Gauss point of the interface element; in these expressions the areas A_i are accounted for by the volume fraction f_c of the stress-carrying portion of fibres, assumed to be known.

Equation (3) requires an expression for the local stress $\sigma_i(\delta)$ in a collagen fibre. In [Genna 2006] such an expression was provided by a simple nonlinear equation, with no physical meaning. Here, the microstructurally-based relationship proposed in the accompanying paper [Genna 2014] is adopted instead. Such a relationship requires, essentially, the calculation of a statistical integral of the type (3) also for obtaining the value of the local stress $\sigma_i(x_c, \delta)$.

This same stress–stretch expression automatically accounts for the tensile failure of the PDL because, after following a nonlinear increase of stress with elongation, it describes a stress peak and then a stress decrease due to the progressive failure of the shortest subfibrils, and finally reaches an irreversible zero stress value. From then on, the Gauss point gives no more mechanical contribution in tension.

According to these models, the mechanical behaviour of the PDL is nonlinear elastic–brittle, and time-dependency is neglected. This is a necessity, since both the adopted models — for the single collagen fibre, and for the PDL — are a first tentative description of the behaviour of these components, based on their microstructure: study is under way to include, among the basic mechanisms, also viscosity. On the other hand, and because of the short times involved by the tests, the specific problem herein analysed can be considered as inviscid as long as the material properties are obtained from tests performed at about the same loading velocity.

The reader is referred to [Genna 2006] for further details concerning the interface element formulation and implementation, and to [Genna 2014] for further details concerning the microstructurally-based stress–stretch equation for σ_i of (3).

3.2. Geometries. Figure 4 illustrates the four geometries considered in the numerical analyses. The first one, labelled (a), refers to one of the swine teeth extractions. The sample geometry has been acquired by means of a Sinergia Scan scanner, by Nobil–Metal Spa, which provides a surface point cloud with a resolution of $5 \, \mu m$. The point cloud has been transformed into a surface mesh, smoothed, and finally converted into a solid geometry by means of the code JRC 3D Reconstructor [Gexcel Src 2008].

The model includes the tested portion of the jaw, subdivided into cortical and spongious bones, the extracted canine tooth, and the titanium alloy wire adopted to connect the tooth to the testing machine. The jawbone is considered fully fixed to the reference system at a central portion that corresponds roughly to the size of the grips, and the top node of the wire is subjected to a prescribed displacement in the direction of the wire axis.

The remaining images in Figure 4 refer to human teeth. Image (b) refers to a two-rooted molar, whose geometry is taken from previous work [Corradi and Genna 2003]; image (c) to an incisor, also taken
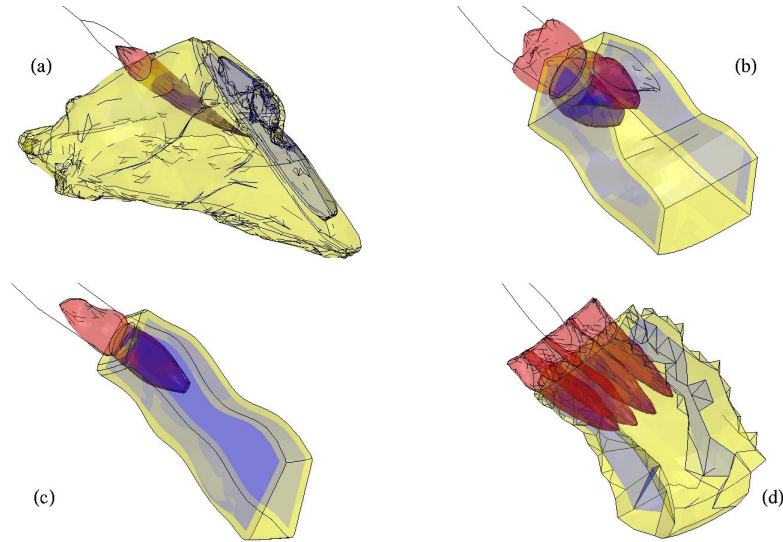
Figure 4. Geometries considered in the numerical analyses. (a) Swine canine, taken from a real sample; (b) human molar (schematic), taken from [Corradi and Genna 2003]; (c) human incisor (schematic), taken from [Corradi and Genna 2003]; (d) human incisor (schematic), from [Genna 2006]. The cortical bone is shown in yellow, the spongious bone in blue.

Tooth type	Height [mm]	Average diameter [mm]	PDL surface area [mm^2]
Swine canine (a)	29.32	4.26	292.04
Human molar (b)	15.04	6.50	240.76
Human incisor (c)	14.62	3.58	79.43
Human incisor (d)	21.19	4.22	160.18

Table 1. Geometrical data for the four tooth samples studied numerically.

from [Corradi and Genna 2003]; and image (d) corresponds to a different incisor, i.e., the same case, studied, by means of a simpler model, in [Genna 2006]. In all these analyses the boundary conditions are the same as described for the swine sample.

Table 1 reports the essential geometrical information about the four teeth studied numerically, i.e., sizes and areas of the root surfaces connected to the jawbone by the PDL.

3.3. *Materials.* In all the analyses, the bone, both cortical and spongious, and the dentine have always been described as linear elastic; the relevant material parameters are the same as those already adopted in [Genna 2006]. Also, the titanium alloy of the wire has been treated as linear elastic. The only nonlinear material, in all the numerical analyses, is the PDL layer, for which the following material parameters are required:

- the thickness w_0 of the PDL layer;
- the angles β_0 and θ_0 as defined above;

Material	Young's modulus [MPa]	Poisson's coefficient
Titanium alloy	78000	0.31
Dentine	20000	0.25
Cortical bone	13700	0.3
Spongious bone	1370	0.3

Table 2. Elastic properties of the jawbone and titanium alloy wire in the numerical models.

- the volume fraction f_c of stress-carrying collagen fibres inside the PDL;
- the expected value $E(x_c)$ and variance $\text{Var}(x_c)$ of the PDL collagen fibres waviness, described by the variable x_c introduced in Section 3.1;
- the data for the stress–stretch constitutive law of a single collagen fibre, that here correspond to the 19 parameters required by the model described in [Genna 2014]. The symbols and the relevant meanings are summarised here for convenience:
  - $N = 4$ is the number of internal levels defining the fibre microstructure;
  - K_s, K_m are the stiffnesses of a single tropocollagen molecule, described as a trilinear elastic–brittle rod;
  - X_{ks}, $X_{km} \geq 1$ are nondimensional coefficients that account for the effect of cross-linking on the fibre stiffness;
  - $X_f \geq 0$ is a nondimensional coefficient that describes the effect of cross-linking on the collagen brittle failure;
  - s is a molecular displacement related to the end of the second molecular stiffness range;
  - u_f^* is a molecular displacement related to the molecule failure;
  - Φ_m is the tropocollagen molecule diameter;
  - L_m is the contour length of a single tropocollagen molecule;
  - $f_0 f_1 f_2 f_3$ is the product of the volume fractions of the stress–carrying portion of internal sub-fibrils at the various internal levels of the collagen fibre microstructure (see [Genna 2014]);
  - $E(y_i)$, $\text{Var}(y_i)$ are the expected values and the variances, respectively, of the random variables $y(i)$, $i = 1, \ldots, N$, i.e., the nondimensional ratios that describe the waviness of the collagen subcomponents at the various internal levels;
- other parameters that define the compressive behaviour of the PDL, of no interest here.

Table 2 summarises the values of the elastic parameters for the two bone types, the dentine, and the titanium alloy wire.

Table 3 reports the numerical values of all the adopted material parameters for the description of the PDL. The thickness w_0 of the PDL layer has been varied, in some analyses, to verify its effect on the resulting force–displacement curves. Following the results presented in [Genna et al. 2008], for swine PDL the value $w_0 = 0.50$ mm has been adopted as a reference one, although in several cases higher values — up to about 1 mm — have been measured.

The values adopted for the angle β_0 depend on the position, along the tooth root axis, of each considered Gauss point, according to the geometrical information that can be found in the literature for human teeth [Berkovitz et al. 1995], and are the same as those adopted in [Genna 2006]. In the absence of better

Material parameter	Adopted value	Material parameter	Adopted value	Material parameter	Adopted value
w_0	swine: 0.50 mm	$E(y_2)$	0.9952	Φ_m	1.5 nm
	human: 0.25 to 1.0 mm	$E(y_3)$	0.99779	L_m	301.7 nm
β_0	$-25°$ to $30°$	$E(y_4)$	0.9979	s	50 nm
θ_0	$76.8°$ to $90°$	$\mathrm{Var}(y_2)$	$4.9 \cdot 10^{-5}$	u_f^*	167 nm
f_c	0.05	$\mathrm{Var}(y_3)$	$6.561 \cdot 10^{-5}$	L_b	random variable
$E(x_c)$	1.093	$\mathrm{Var}(y_4)$	$3.387 \cdot 10^{-5}$	X_{ks}	1
$\mathrm{Var}(x_c)$	0.00397	$f_0 f_1 f_2 f_3$	0.05	X_{km}	1
$E(y_1)$	0.995	K_s	10 pN/nm	X_f	0
$\mathrm{Var}(y_1)$	$2.5 \cdot 10^{-5}$	K_m	30 pN/nm		

Table 3. Material parameters required by the periodontal ligament model.

information, the same values have been adopted also for the swine canine.

In Table 3, the parameter L_b, which denotes the uncoiled, unstretched length of a single collagen fibre at rest, is marked as a random variable, since its value depends on the statistics of the waviness of the fibres, i.e., on the current values of x_c of (2) during the integration process.

4. Results

4.1. *Experimental results.* Of the forty-seven tests, only sixteen concluded with the successful extraction of the tooth from its socket. All the other ones ended prematurely either because of wire failure or because of the failure of the tooth crown, due to the propagation of a crack initiated by the drilled hole.

Of these successful sixteen tests, all producing scattered results because of the inevitable differences among specimens, only seven cases have been considered as fully significant. The other ones produced even more dispersed results, either because the teeth were somehow defective or too small, so as to produce extraction forces far too small, or because they were affected by an excessive interference with the tissues — including soft ones — surrounding the extracted tooth, as indicated by the extremely large values of the displacement corresponding to the peak forces.

Figure 5 shows the obtained force–displacement curves for the best seven cases. The peak forces found experimentally are in the range 100 to 450 N, and the corresponding displacements are in the range 1 to 4.6 mm.

Beside the absolute values of stiffness (from about 20 to about 150 N/mm, depending on the samples, in the initial region), peak force, and peak displacement, another significant feature of all the curves of Figure 5 is the presence of several local peaks of force, both before and after the absolute maximum. Some of the peaks after the absolute maximum force may have little importance, since they are probably due to the existence of gingival or bone tissue that stays connected to the tooth even after its detachment from the socket, as shown in Figure 6. This residual connection might also be responsible for some extremely large displacement values found before the full drop of the force value to zero.

The force peaks before the absolute maximum, and some after it, are due to the variable inclination of the PDL collagen fibres along the tooth root, as will be shown in Section 5.
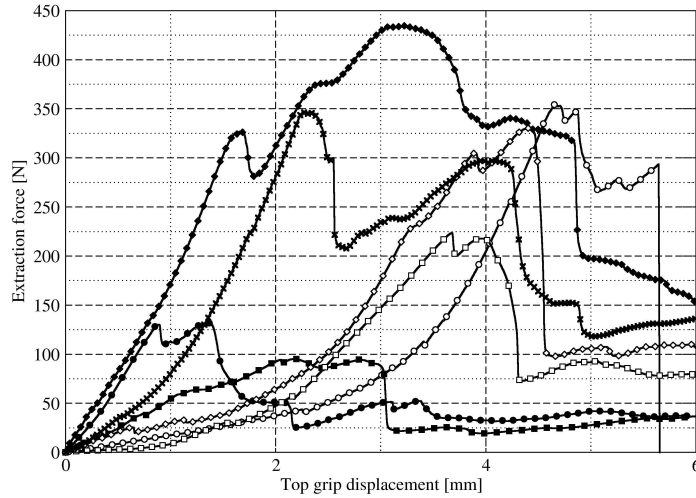
Figure 5. Experimental results from the tests on swine canines. In ordinate: force measured by the testing machine; in abscissa: grip opening displacement.
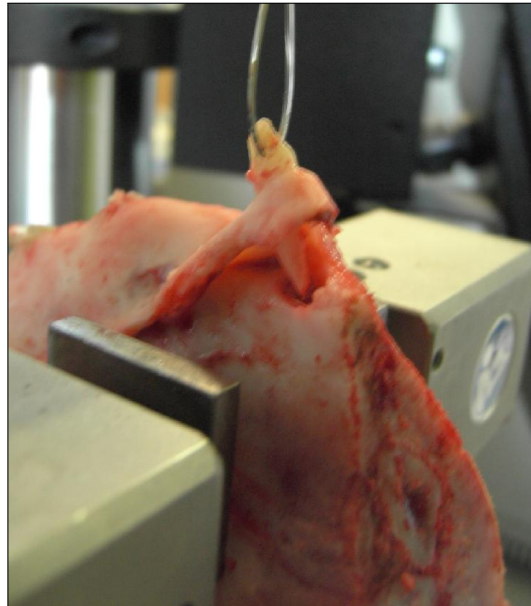
Figure 6. Tissues remaining connected to the swine canine after its extraction from the socket.

4.2. *Numerical results.* Figure 7 illustrates the first numerical result, which refers to the simulation of the extraction of a swine canine, performed on the geometry of Figure 4(a). In this analysis, the PDL thickness was set equal to $w_0 = 0.5$ mm. Figure 8 compares the numerical results obtained for the simulation of the extraction of human teeth on the geometries of Figure 4(b), (c), and (d); in all these cases the PDL thickness was set equal to $w_0 = 0.25$ mm.
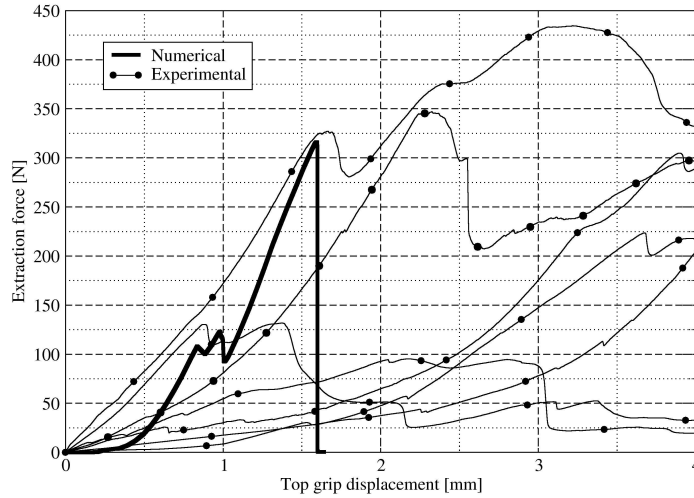
Figure 7. Swine canine extraction: comparison between experimental and numerical results. The thick solid curve is obtained numerically, from the approach presented in this work. All the remaining curves, with black circles, are experimental results already shown in Figure 5.
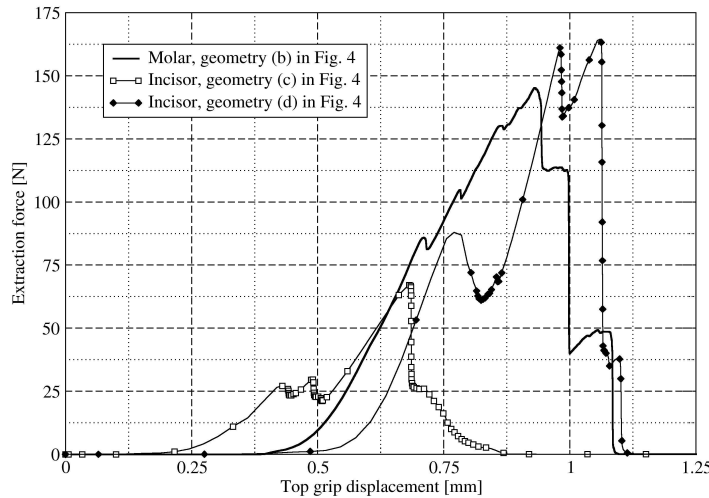
Figure 8. Numerical results: comparison among different geometries for human teeth. The solid curve refers to the molar of Figure 4(b); the curve with white squares refers to the geometry of Figure 4(c); and the curve with black diamonds refers to the geometry of Figure 4(d).

Figures 9 and 10 show, respectively, the influence of the PDL thickness on the computed force–displacement extraction curve, and the influence of the wire stiffness on the same curve. Figure 9 shows results obtained from the same geometry (that of Figure 4(c)), by varying the adopted value for the PDL thickness w_0. Figure 10 presents two plots, both referring to the same simulation, i.e., the case of the
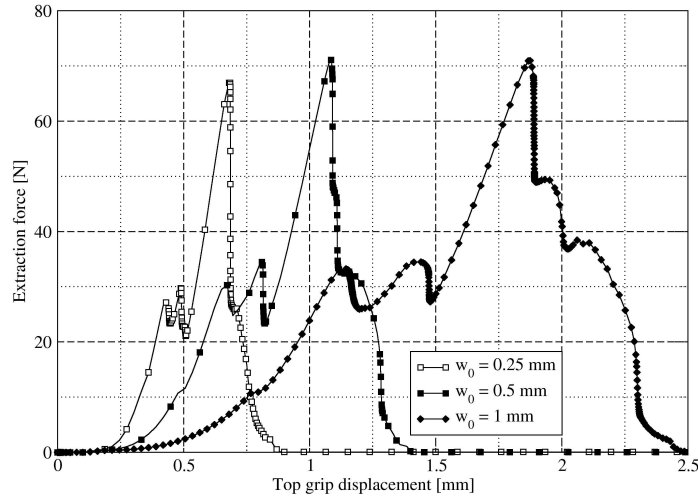
Figure 9. Numerical results: effect of the PDL thickness w_0 on the computed force–displacement curves. The geometry is that of Figure 4(c) (human incisor).
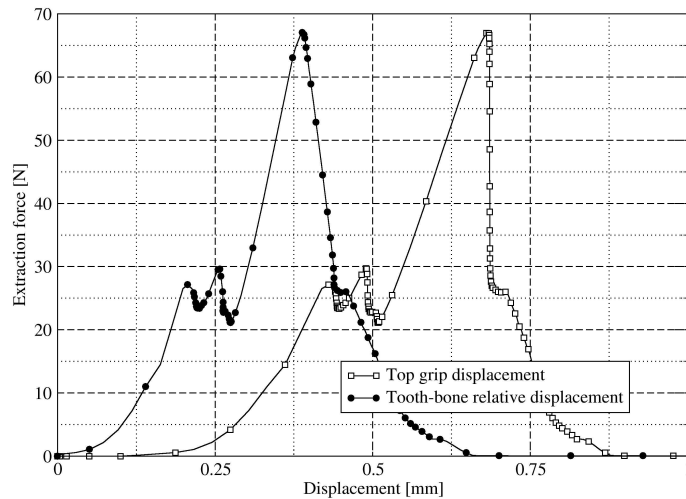
Figure 10. Numerical results: effect of the stiffness of the connecting wire on the computed force–displacement curves. The geometry is that of Figure 4(c) (human incisor).

human incisor of Figure 4(c), with $w_0 = 0.25$ mm: the first curve is the same as in Figure 8, the second curve plots the same force as a function of the relative displacement between the root crown and the top surface of the cortical bone around the tooth itself.

Finally, Figure 11 illustrates the effect produced by the variation of the PDL fibre inclination, along the tooth root, on the force–displacement curve. The plots refer to the case of the human incisor of Figure 4(c), with $w_0 = 0.25$ mm; the first one coincides with that of Figure 8, the second one is obtained by setting $\beta_0 = 0$ and $\theta_0 = 90°$ in the PDL constitutive parameters, i.e., fixed fibre direction, orthogonal to the root external surface, and with no X-shaped transversal arrangement.
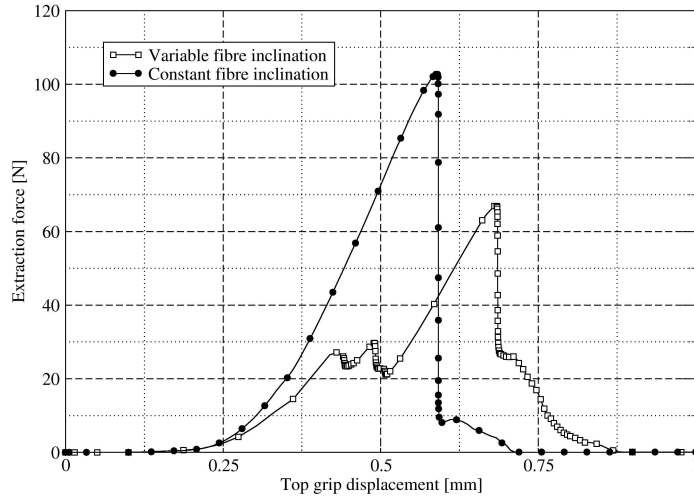
Figure 11. Numerical results: effect of the inclinations β_0 and θ_0, shown in Figure 3, on the computed force–displacement curves. The geometry is that of Figure 4(c) (human incisor). The curve with white squares is the same as the one in Figure 8, with "realistic" values for both β_0 and θ_0. The curve with black dots is obtained by setting $\beta_0 = 0°$ and $\theta_0 = 90°$ at all the interface elements.
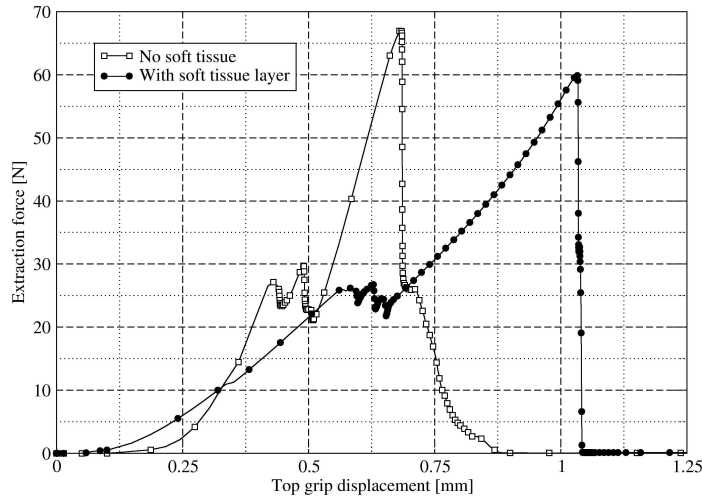
Figure 12. Numerical results: effect of the stiffness of a thin layer of soft tissue around the jawbone on the computed force–displacement curves. The geometry is that of Figure 4(c) (human incisor).

The size of the discretised numerical problem has always been in the range of 30 000 to 50 000 degrees of freedom, depending on the considered model. The CPU times, on a Hewlett–Packard workstation xw9300, with 2 AMD Opteron 64-bit dual-core processors, but no parallel processing exploited, have

been of the order of 3 hours for all the cases. This demonstrates the practical usability of the constitutive model adopted for the single collagen fibre proposed in [Genna 2014].

5. Discussion

The experimental force–displacement curves shown in this paper are obtained by means of a technique that differs from the one adopted in real dental practice: the tooth has simply been pulled out of the socket, whereas the standard procedure involves applying a luxation, with leverage and torsion. It is currently impossible to understand the extent of the possible differences in the force and displacement values due to this discrepancy.

Moreover, the choice of extracting only single-rooted canines has somehow limited the range of results that could possibly be obtained. On the other hand, it has to be considered that, quite often, the extraction of two- or three-rooted teeth, or of teeth having roots with a complex/defective geometry, results in breaking either the socket bone or the root itself: this would have been a useless complication in our case.

Both a significant dispersion even in the best experimental results, and a lack of an established standard for the experimental technique are apparent. The last difficulty could not be avoided, in view of the complete novelty of the performed tests; it would be desirable to establish a standard procedure even for tooth extraction laboratory tests, but the extreme variability of all the factors involved makes this a quite difficult task, and anyway outside the scope of this work.

As for the scatter in the measured force–displacement curves, it should be noted that each curve refers to a completely different sample, taken from a different animal, each with its own physical and geometrical properties. The dispersion of the results is similar to that obtained in the past from experiments, in a much more controlled regime, performed on small PDL samples, such as those of [Genna et al. 2008] and [Pini et al. 2004]. The situation, in the case of large mandible blocks and full teeth, is understandably more dispersed.

The experimental setup seems to influence mainly the displacement values, but to provide reliable values for the extraction forces. This is also confirmed by considering the average stress values corresponding to the peak extraction force, obtained by dividing the force by the root area. Adopting an average value for the root surface area equal to $143 \, \text{mm}^2$ as given by the tests, and considering the observed range of peak force values, i.e., 100 to 450 N, one obtains average values for the fracture stresses of the PDL in the range 0.7 to 3.2 MPa, in good agreement with the experimental results on swine PDL samples reported in [Genna et al. 2008].

Both the observed and the computed peaks of force fall within the range of values that can be found in the literature; nevertheless, the results presented here seem to be the first that have been obtained directly from an extraction test performed by means of a standard testing machine capable of measuring both forces and displacements. The few results previously available are all obtained in somewhat indirect ways, such as, for instance, those presented in [Ahel et al. 2006], where a forceps was instrumented in such a way as to obtain "pressure and rotation measurements".

Figure 9 shows that larger values of the PDL thickness produce larger displacements at about the same force values. This might help in explaining some of the larger values of displacements recorded in the laboratory tests: swine PDL can be much thicker than human one, according to the available information, and its thickness gives a clear contribution to the overall stiffness of the tooth-PDL-bone system.

The comparison of the curves shown in Figure 11 illustrates an important effect of the PDL collagen fibre inclination, and especially so for single-rooted teeth. In the real situation the fibres are arranged so as to withstand all the possible types of loading, always offering stiffness due to their being stretched. The fibres that first offer stiffness, upon an axial pulling displacement of the tooth, are those more aligned with the loading direction, while all the others will undergo either a rigid rotation, or milder stretching. Increasing the tooth axial displacement will eventually lead to the failure of the most stretched fibres, thus causing a local drop in the global extraction force. Thereafter, other groups of fibres will start becoming aligned with the loading direction, and offering stiffness, thus causing a new force increase. This effect is shown by the numerical results, which, for the case of a fixed fibre inclination along the root, do not show any local force maximum.

In the case of molars, the variable inclination of the collagen fibres is less important, because the root surface is not convex. In fact, even considering $\beta_0 = 0°$ and $\theta_0 = \pm90°$, in a numerical simulation of the extraction of molars, one would obtain at least a local peak of force before the absolute maximum, corresponding to the failure of the interradicular fibres located between the roots, in the internal concave zone under the tooth crown. These fibres, with $\beta_0 = 0°$, are practically aligned with the root axis in the undeformed configuration, and would be the first to stretch and break.

The numerical simulations are based on mathematical models for both the PDL as a tissue, and a single collagen fibre as its basic constituent, developed from the same basic idea, i.e., to describe in the simplest possible way both the tissue and the fibre microstructure. Of course, for both the PDL and the collagen fibres many other mathematical models exist in the literature, although, to the best of our knowledge, none of them has a micromechanical basis. There is no space here (and this is not the proper place, also) to review the existing literature; the interested reader is referred to the list of references in [Genna 2014] for collagen, and to [Fill et al. 2012; Romanyk et al. 2013], and the list of references in [Genna 2006], for the PDL.

In all the force–displacement plots illustrated in the previous section, the influence of the wire stiffness and initial slack is quite important, as explicitly shown also by Figure 10. Beside this aspect, one must also consider that, in the experiments, the lower grips of the testing machine were connected to a block of bone which contained residual portions of soft tissues, whose influence on the recorded displacements might be nonnegligible. In order to quantify this aspect, a second FEM analysis for the case of the human incisor of Figure 4(c) was run, in which the cortical bone was surrounded by a thin layer (0.5 mm thick) of soft tissue, whose mechanical behaviour was simulated by means of a hyperelastic model of the Ogden type, with a quadratic potential function.

Figure 12 shows the comparison between the force–displacement curves obtained with and without the soft tissue around the cortical bone: it is apparent that even a very thin layer of very compliant material can increase the displacement at the peak force by about 60%, with a slight decrease of peak force value.

It is also interesting to observe that the numerical simulations, even when they take into account several factors that might increase the overall compliance, always tend to underestimate the displacement corresponding to the maximum force, with respect to the experimental results. It must be recalled that the material parameter choice in the description of the PDL collagen corresponds to a very large ductility, with uniaxial Green–Lagrange strain at peak stress of the order of 1.2 for the PDL layer, as shown in Figure 8 of [Genna 2014], and uniaxial Biot strain at peak stress of the order of 0.55 for a single collagen fibre, as was also necessary when adopting the different model presented in [Genna 2006]. In

the numerical simulations presented here, cross-linking in the PDL collagen has always assumed to be absent, which corresponds to the highest possible values of strains at failure in the collagen fibres [Pins et al. 1997] in the adopted model; yet, the global behaviour obtained from the FEM simulations, as said, always shows an underestimated ductility with respect to the experimental one. Even the case expected to produce the largest displacement at the force peak, i.e., one in which both the wire and the thin layer of soft tissue are present, with the largest among the adopted values of the PDL thickness ($w_0 = 1$ mm), yields a displacement value of 2.3 mm at the force peak, smaller than most of the experimental values.

The large displacement values obtained experimentally seem therefore to confirm the corresponding high strain values that can be reached by the PDL collagen fibres before failure.

6. Conclusions

For the first time, to the best of the authors' knowledge, force–displacement curves have been obtained experimentally from the process of extraction of swine teeth from their sockets. The experimental setup adopted allows the use of a standard testing machine, thus providing direct values of both forces and displacements. Nevertheless, at the current stage of development it is not yet fully standardised so as to provide results substantially independent of the testing apparatus itself. Work is in progress in two main respects: the inclusion of a "rigid" connection between tooth and machine grip, and the measurement of the relative displacement between tooth and bone, possibly through optical devices.

The results herein presented are expected to be useful to developers of mathematical models for the PDL, since they provide at least some indirect information (for instance, about the fibre inclination) on the mechanical and geometrical properties of the PDL.

The numerical analysis of the same problem has shown the ability to obtain meaningful results, and has also proven the practical applicability of the constitutive model for a single collagen fibre proposed in an accompanying paper [Genna 2014].

Further work, in this respect, should tackle the problem of the PDL behaviour under small and cyclic loading, which will require taking into account irreversible and time-dependent effects. With respect to these last, we point out that, for simplicity in this initial stage, the experimental program carried out so far did not investigate the effect of the loading, i.e., displacement, rate, which was always kept constant, at 2 mm/min. Although slower loads could be successfully applied with the adopted setup, faster ones could not, since they would produce premature ending of the experiment due to fracture either of the wire or of the tooth crown.

References

[Ahel et al. 2006] V. Ahel, I. Brekalo, J. Ahel, and G. Brumini, "Measurements of tooth extraction forces in upper incisors", *Coll. Anthropol.* **30**:1 (2006), 31–35.

[Alatli et al. 1997] I. Alatli, J. Li, and L. Hammarström, "Ultimate tensile strength of PDL of molars in rats after 1-hydroxy-ethylidene-1, 1-bisphosphonate injections", *J. Dent.* **25**:3-4 (1997), 313–319.

[Berkovitz et al. 1995] B. K. B. Berkovitz, B. J. Moxham, and H. N. Newman, *The periodontal ligament in health and disease*, 2nd ed., Mosby-Wolfe, London, 1995.

[Chiba et al. 1980] M. Chiba, S. Ohshima, and K. Takizawa, "Measurement of force required to extract the mandibular incisor of rats of various ages", *Arch. Oral Biol.* **25**:10 (1980), 683–687.

[Corradi and Genna 2003] L. Corradi and F. Genna, "Finite element analysis of the jaw-teeth/dental implant system: A note about geometrical and material modeling", *Comput. Model. Eng. Sci.* **4**:3 (2003), 381–396.

[Dorow et al. 2003] C. Dorow, N. Krstin, and F. Sander, "Determination of the mechanical properties of the periodontal ligament in a uniaxial tensional experiment", *J. Orofac. Orthop.* **64**:2 (2003), 100–107.

[Fill et al. 2011] T. S. Fill, J. P. Carey, R. W. Toogood, and P. W. Major, "Experimentally determined mechanical properties of, and models for, the periodontal ligament: Critical review of the current literature", *J. Dent. Biomech.* **2**:1 (2011), Article ID 312980.

[Fill et al. 2012] T. S. Fill, R. W. Toogood, P. W. Major, and J. P. Carey, "Analytically determined mechanical properties of, and models for the periodontal ligament: Critical review of literature", *J. Biomech.* **45**:1 (2012), 9–16.

[Gei et al. 2002] M. Gei, F. Genna, and D. Bigoni, "An interface model for the periodontal ligament", *J. Biomech. Eng. ASME* **124**:5 (2002), 538–546.

[Genna 2006] F. Genna, "A micromechanically-based, three-dimensional interface finite element for the modeling of the periodontal ligament", *Comput. Methods Biomech. Biomed. Engin.* **9**:4 (2006), 243–256.

[Genna 2014] F. Genna, "A nonlinear stress-stretch relationship for a single collagen fibre in tension", *J. Mech. Mater. Struct.* **9**:5 (2014).

[Genna et al. 2008] F. Genna, L. Annovazzi, C. Bonesi, P. Fogazzi, and C. Paganelli, "On the experimental determination of some mechanical properties of porcine periodontal ligament", *Meccanica* **43**:1 (2008), 55–73.

[Gexcel Src 2008] *JRC 3D Reconstructor*, Gexcel Src, Brescia, Italy, 2008, http://www.gexcel.it/en/lidar-software-solutions/reconstructor-full.

[Hibbitt et al. 2013] H. D. Hibbitt, B. Karlsson, and P. Sorensen, *Abaqus user's manuals, Release 6.12*, Dassault Systèmes, Simulia Corp., Providence, RI, 2013.

[Instron Corporation 2001] *Instron model 5848 MicroTester: Reference manual—equipment*, Instron Corporation, Norwood, MA, 2001, http://www.instron.us/wa/library/StreamFile.aspx?doc=808.

[Komatsu et al. 1990] K. Komatsu, S. Ohshima, and M. Chiba, "Measurement of force required to extract the mandibular first molar from its socket in the dissected jaw of growing young rats", *Gerodontology* **9**:1 (1990), 3–7.

[Lehtinen and Ojala 1980] R. Lehtinen and T. Ojala, "Rocking and twisting moments in extraction of teeth in the upper jaw", *Int. J. Oral Surg.* **9**:5 (1980), 377–382.

[Papadopoulou et al. 2014] K. Papadopoulou, L. Keilig, T. Eliades, R. Krause, A. Jäger, and C. Bourauel, "The time-dependent biomechanical behaviour of the periodontal ligament—an *in vitro* experimental study in minipig mandibular two-rooted premolars", *Eur. J. Orthod.* **36**:1 (2014), 9–15.

[Pini et al. 2004] M. Pini, P. Zysset, J. Botsis, and R. Contro, "Tensile and compressive behaviour of the bovine periodontal ligament", *J. Biomech.* **37**:1 (2004), 111–119.

[Pins et al. 1997] G. Pins, E. Huang, D. Christiansen, and F. Silver, "Effects of static axial strain on the tensile properties and failure mechanisms of self-assembled collagen fibers", *J. Appl. Polym. Sci.* **63**:11 (1997), 1429–1440.

[Qian et al. 2009] L. Qian, M. Todo, Y. Morita, Y. Matsushita, and K. Koyano, "Deformation analysis of the periodontium considering the viscoelasticity of the periodontal ligament", *Dent. Mater.* **25**:10 (2009), 1285–1292.

[Romanyk et al. 2013] D. L. Romanyk, G. W. Melenka, and J. P. Carey, "Modeling stress–relaxation behavior of the periodontal ligament during the initial phase of orthodontic treatment", *J. Biomech. Eng. ASME* **135**:9 (2013), 1–8.

[Sanctuary et al. 2005] C. S. Sanctuary, H. W. A. Wiskott, J. Justiz, J. Botsis, and U. C. Belser, "In vitro time-dependent response of periodontal ligament to mechanical loading", *J. Appl. Physiol.* **99**:6 (2005), 2369–2378.

[Tanaka et al. 2007] E. Tanaka, T. Inubushi, K. Takahashi, M. Shirakura, R. Sano, D. A. Dalla-Bona, A. Nakajima, T. M. G. J. van Eijden, and K. Tanne, "Dynamic shear properties of the porcine molar periodontal ligament", *J. Biomech.* **40**:7 (2007), 1477–1483.

FRANCESCO GENNA: francesco.genna@unibs.it
Department of Civil Engineering, University of Brescia, Via Branze 43, I-25123 Brescia, Italy

CORRADO PAGANELLI: corrado.paganelli@unibs.it
Dental Clinic, University of Brescia, Piazzale Spedali Civili, 1, I-25123 Brescia, Italy

msp

NONUNIFORM SHEAR STRAINS IN TORSIONAL KOLSKY BAR TESTS ON SOFT SPECIMENS

ADAM SOKOLOW AND MIKE SCHEIDLER

We investigate inertial effects in torsional Kolsky bar tests on nearly incompressible, soft materials. The results are relevant for materials with instantaneous elastic shear modulus on the order of 1–1000 kPa and density on the order of water. Examples include brain tissue and many other soft tissues and tissue surrogates. We have conducted one- and three-dimensional analyses and simulations to understand the stress and strain states that exist in these materials in a torsional Kolsky bar test. We demonstrate that the short loading pulses typically used for high strain-rate (e.g., 700/s) tests do not allow the softer specimens to "ring-up" to uniform stress and strain states and that consequently the shear stress versus shear strain data reported in the literature are erroneous. We also show that normal stress components, which are present even in quasistatic torsion of nonlinear elastic materials, can be amplified in dynamic torsion tests on soft materials.

1. Introduction

Kolsky bar tests are widely used to study strain-rate effects in inelastic solids [Gray 2000; Chen and Song 2011]. In a *compression* Kolsky bar test, a relatively thin specimen is sandwiched between two bars. Impact at one end of the incident bar generates a compressive wave that travels along the bar, through the specimen, and into a transmission bar. The goal of this test is to subject the specimen to uniform uniaxial stress and uniform (biaxial) strain at a prescribed axial strain-rate. These uniform conditions can often be achieved after an initial "ring-up" period involving multiple wave reflections from the specimen-transmission bar and specimen-incident bar interfaces. Once uniform conditions have been achieved in the specimen, the axial stress, axial strain, and axial strain-rate histories in the specimen can be deduced from strain gage measurements on the elastic bars: the axial stress is proportional to the strain in the transmission bar, and the axial strain-rate is proportional to the strain in the incident bar generated by the wave reflected from the specimen and transmission bar. A similar approach utilizes a *torsional* wave in the Kolsky bar instead of a compressive wave [Gilat 2000; Hartley et al. 1985]. Typically, a number of test are performed at different strain-rates, and the data are presented as a family of stress-strain curves with each curve corresponding to a different (approximately constant) strain-rate.

The standard Kolsky bar techniques work well on metals, composites, and stiff polymers and have provided useful data for the calibration of viscoplastic constitutive models and rate-dependent failure models. More recently, Kolsky bar tests have been performed on gelatins and soft biological specimens with the goal of providing data for the calibration of viscoelastic constitutive models for these materials. However, considerable difficulties have been encountered with these softer specimens. Radial accelerations in compression tests may result in stress states that are not uniaxial, that is, radial and
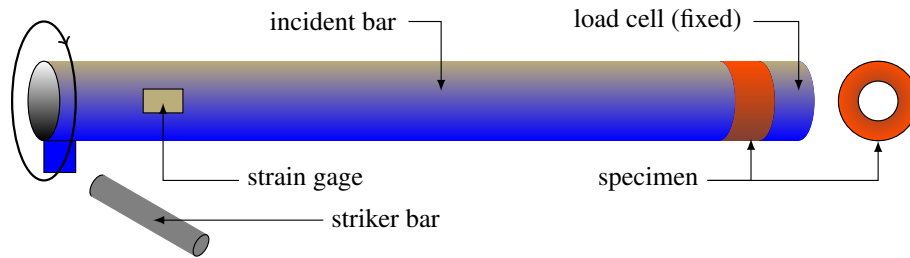
Figure 1. Schematic (not to scale) of the experimental setup for the modified torsional Kolsky bar described in [Nie et al. 2013]. Only the specimen is included in the simulations.

hoop stresses that are a significant fraction of the axial stress but cannot be measured [Scheidler and Kraft 2010; Scheidler et al. 2011; Warren and Forrestal 2010]. Studies utilizing compression Kolsky bar techniques purportedly removed radial inertia effects by switching from disk-shaped specimens to annular specimens [Chen and Song 2011]. It was later shown that annular specimens are also plagued by radial inertia effects and that the observed increases in axial stress at high strain-rates were falsely attributed to viscoelastic properties of the specimen [Scheidler and Kraft 2010; Sanborn 2011; Sanborn et al. 2012].

Recently, a variation of the torsional Kolsky bar test has been developed for studying the strain-rate sensitivity of very soft materials and applied to bovine brain tissue [Nie et al. 2013; Sanborn et al. 2012]. In this modified torsion test, the transmission bar is replaced with a torque load cell in order to generate a stronger signal than could be obtained from strain gage measurements on a transmission bar; see Figure 1. The faces of thin annular specimens are glued to the incident bar and the load cell. Strain gage measurements in the incident bar are used to infer the rate of the angle of twist at the specimen-incident bar interface and consequently a volumetric average of the shear strain-rate in the specimen. Integration yields the angle of twist at the interface and consequently a volumetric average of the shear strain in the specimen. The radially averaged shear stress at the specimen-load cell interface is deduced from the torque measured at the load cell. The stress-strain curves in [Nie et al. 2013] are obtained by plotting this *radially averaged shear stress at the load cell* versus the *volume averaged shear strain in the specimen*. Comparison of stress-strain curves at different strain-rates could (in principle) yield information on the rate-sensitivity of the shear stress. Nie et al. [2013] performed Kolsky bar tests on bovine brain tissue at an average shear strain-rate of 700/s. Analogous quasistatic tests at strain-rates of 0.01/s and 1/s were performed for comparison, and the results appeared to indicate a substantial increase in shear stress in the dynamic test.

The effects of radial inertia in this torsional Kolsky bar test are expected to be much lower than in a compression test at the same strain-rate. *However, for specimens as soft as brain tissue, the effects of axial inertia (i.e., torsional wave propagation) may be significant.* The shear wave speeds in the softer specimens are so low that even for thin (i.e., 1–2 mm thick) specimens there may be insufficient time for the specimen to "ring-up" to an axially uniform state of stress, strain, and strain-rate. In particular, if the shear strain has large axial variations, then the shear strain at the specimen-load cell interface may not be close to the average shear strain used to generate the stress-strain curves in [Nie et al. 2013], in which case their "stress-strain curves" would not provide valid constitutive data. Likewise, the shear strain-rate at the specimen-load cell interface may not be close to the reported average shear strain-rate.

Torsion and compression tests on soft materials differ in another significant way. As noted above, for compression tests, the desired uniaxial stress state may be impossible to achieve dynamically, but uniaxial

stress can always be achieved quasistatically if frictional effects at the specimen faces are negligible. However, even in a quasistatic torsion test, the desired state of *pure shear stress* is impossible to achieve except for infinitesimal deformations. Significant normal stresses can develop in finite deformation quasistatic torsion. While radial stresses can be reduced by the use of annular specimens, axial and hoop stresses may not be negligible. Furthermore, the glued boundary conditions for annular specimens can be expected to result in axial variations in the stress and strain state even in a quasistatic test since radial deformations are prohibited at the ends of the specimen but not in the interior. Thus, unlike quasistatic compression tests, the stress state in quasistatic torsion tests on soft materials is already quite complicated, and inertial effects in the corresponding dynamic test will further complicate these stress states. Even if the full stress state could be measured in a dynamic torsion test, it would be difficult to sort out the role of inertial effects from nonlinear elastic or viscoelastic effects without results for the corresponding quasistatic case for comparison. This problem is compounded by the fact that in the torsional Kolsky bar test only the torsional (θz) stress component can be inferred from the test data, and this is known only on the face of the specimen in contact with the load cell.

In view of these issues, we have undertaken numerical simulations of both dynamic and quasistatic torsion tests on soft and nearly incompressible materials. To simplify the dynamic simulations, the incident bar and the load cell are not included; they are replaced with appropriate boundary conditions at the specimen ends. Unlike a real torsion test, the simulations provide the complete stress and strain states at each point in the specimen although a constitutive model must necessarily be assumed. A linear elastic constitutive model was used in our one-dimensional simulations, and a nonlinear elastic constitutive model was used in most of our three-dimensional simulations.

Of course, soft tissues are viscoelastic (and poroelastic as well), and the goal of Kolsky bar tests on these inelastic materials is to quantify their strain-rate sensitivity. However, performing numerical simulations with elastic constitutive models is a particularly useful way of revealing inertial effects in dynamic tests. The stress in an elastic material is rate-independent. Thus, any differences between quasistatic and dynamic simulations of torsion on elastic specimens must necessarily be due to *inertial effects*: *gradients in stress and strain resulting from acceleration of the specimen*. As discussed above, axially nonuniform shear strains in the specimen would invalidate the analysis used to generate the stress-strain curves from the experimental data. Use of viscoelastic models in the simulations will add strain-rate effects but not alter the presence of inertial effects; as we will demonstrate, the main issue here is the slow shear wave speed in the specimen.

Finally, we emphasize that the purpose of this paper is not to propose or examine particular constitutive models for brain tissue or other soft materials but rather to investigate the validity of a particular dynamic test that was developed in an attempt to characterize the high strain-rate response of brain tissue.

The paper is organized as follows. First, in Section 2, we provide an overview of the loading pulses, material properties, and simulation parameters. Next, in Section 3, we discuss our one-dimensional analysis and simulations of torsional waves in a linear elastic specimen. In Section 4, we present the results of our quasistatic analysis and simulations of a full three-dimensional isotropic nonlinear elastic specimen. Here we used a compressible version of the well-known Mooney–Rivlin model for incompressible materials with bulk and shear moduli chosen to yield a nearly incompressible material. Section 5 contains the results of our three-dimensional dynamic simulations of the torsion test, most of which also used the Mooney–Rivlin model. However, Section 5B contains a brief summary of three-dimensional dynamic

simulations that used a nonlinear viscoelastic model for the specimen. Finally, Section 6 contains our major conclusions and their implications on the experimental data collected from torsional Kolsky bar tests. These should be relevant to other dynamic test techniques that attempt to generate a (locally) simple shear such as a double-lap shear test [Saraf et al. 2007; Trexler et al. 2011] or a circular shearing test [Nie et al. 2011]. In Appendix A, we provide some additional details of the numerical methods that were used. Appendix B contains the mathematical details of the loading pulses used in these simulations.

2. Overview of specimen properties, loading pulses, and simulations

We tailored our simulations to be relevant to the experimental loading conditions and specimen geometries considered in [Nie et al. 2013]. In Sections 2A–2C, we discuss how we arrived at our material parameters, boundary conditions, and loading pulse shapes. We also provide an overview of the set of simulations in Sections 2D and 2E.

2A. *Material properties.* From the 0.01/s and 1/s quasistatic tests on bovine brain tissue in [Nie et al. 2013], we estimated small strain shear moduli of $\mu = 4.5$ and 9 kPa, respectively.[1] In most of this paper, we use a shear modulus $\mu = 8$ kPa as representative of brain tissue.[2] This is near the upper limit of the quasistatic shear moduli reported for brain tissue in the literature, the lowest values being around 2 kPa [Donnelly and Medige 1997; Hrapko et al. 2006; Miller and Chinzei 1997; Nicolle et al. 2004; Saraf et al. 2007; Shuck and Advani 1972]. In view of the high water content of brain tissue, we assumed that the density of the brain tissue specimens was that of water ($1\,\mathrm{g/cm}^3$). This specimen density was used in all simulations although the shear modulus was varied considerably (as described in Sections 2D and 2E).

2B. *Specimen geometry and boundary conditions.* The annular specimen was defined as a hollow cylinder of outer radius $R_o = 9.5$ mm, inner radius $R_i = 7.35$ mm, and relatively short length $L = 1.7$ mm, giving a small length-to-diameter ratio of 0.09.[3] Let $\bar{R}$ denote the arithmetic average radius and Δ the corresponding difference in radii:

$$\bar{R} = \frac{R_o + R_i}{2}, \qquad \Delta = \frac{R_o - R_i}{2} = R_o - \bar{R} = \bar{R} - R_i \tag{2-1}$$

so that $R_i = \bar{R} - \Delta$ and $R_o = \bar{R} + \Delta$. Table 1 summarizes the geometrical parameters for all of the simulations performed.

In the Kolsky bar tests, the faces of the specimen were glued to the incident bar and load cell, and for soft specimens, the twist at the specimen-load cell interface should be negligible compared to the twist at specimen-incident bar interface. Thus, for all simulations, one face of the annular specimen was subjected to a rigid rotation while the other face was fixed so that material points on either face could not undergo axial or radial displacements.

Relative to a cylindrical coordinate system, let (r, θ, z) and (R, Θ, Z) denote the coordinates of a material point in the deformed configuration and undeformed reference configuration, respectively. The

---

[1] In view of the difficulties in extracting an initial slope from stress-strain data, these estimates are reasonably close to their estimates of 5.9 and 10.4 kPa.

[2] An instantaneous elastic shear modulus of 40 kPa was used in the viscoelastic simulations discussed in Section 5B. The motivation for this choice is discussed there and in Section 3D.

[3] No information is provided in [Nie et al. 2013] as to the variability in specimen dimensions in the five samples they tested.

R_o (mm)	R_i (mm)	$\bar{R}$ (mm)	Δ (mm)	$\Delta/\bar{R}$	L (mm)	$L/2R_o$
9.5	7.35	8.425	1.075	0.13	1.7	0.09

Table 1. Summary of geometrical parameters for all simulations conducted.

end of the specimen at $Z = L$ is taken to be the fixed face and thus corresponds to the specimen-load cell interface. The other end ($Z = 0$) corresponds to the specimen-incident bar interface; it is rotated by an angle $-\Psi(t)$, where $\Psi \geq 0$ is measured in radians and t denotes time. Thus,

$$\theta|_{Z=0}(t) = \Theta - \Psi(t), \qquad \theta|_{Z=L}(t) = \Theta. \tag{2-2}$$

The *average angle of twist per unit length* is given by

$$\psi(t) = \frac{\theta|_{Z=L}(t) - \theta|_{Z=0}(t)}{L} = \frac{\Psi(t)}{L} \geq 0. \tag{2-3}$$

A measure of the *average shear strain-rate in the specimen* often used in the experimental literature on torsional Kolsky bar tests is

$$\dot{\gamma}_s(t) = \frac{\dot{\theta}|_{Z=L}(t) - \dot{\theta}|_{Z=0}(t)}{L} \bar{R} = \frac{\dot{\Psi}(t)}{L} \bar{R} = \dot{\psi}(t)\bar{R}, \tag{2-4}$$

where a superposed dot denotes the time derivative and $\bar{R}$ is the average radius introduced above [Gilat 2000; Nie et al. 2013]. This average shear strain-rate is typically inferred from strain gage measurements on the bar(s) and then integrated to give an *average shear strain in the specimen*:

$$\gamma_s(t) = \frac{\theta|_{Z=L}(t) - \theta|_{Z=0}(t)}{L} \bar{R} = \frac{\Psi(t)}{L} \bar{R} = \psi(t)\bar{R} \geq 0. \tag{2-5}$$

While other measures of average shear strain are often used in the theoretical literature (see Section 4B), we will use $\gamma_s(t)$ and its rate in order to simplify comparison with the experimental data in [Nie et al. 2013]. For the dynamic simulations considered here, we applied an angular displacement at $Z = 0$ that delivered the desired average strain-rate history $\dot{\gamma}_s(t)$ for the particular simulation. In view of (2-2) and (2-5), this displacement history is given by

$$\theta|_{Z=0}(t) - \Theta = -\Psi(t) = -\frac{L}{\bar{R}}\gamma_s(t). \tag{2-6}$$

2C. ***Loading pulse shapes.*** We use the term *loading pulse* to refer to the average strain-rate history imposed on the specimen. The key features of a typical loading pulse[4] are summarized in panel *a* of Figure 2. These loading pulses are intended to mimic those generated in Kolsky bar experiments. The pulse ramps up smoothly over the time interval $[0, t_r]$ to a maximum average strain-rate $\dot{\gamma}_{max}$, which is held constant for the plateau duration t_p. We assume a symmetric unloading of the pulse; that is, the unloading time is equal to the rise time t_r so that the total duration t_d of the loading pulse is given by

$$t_d = 2t_r + t_p. \tag{2-7}$$

The average strain accumulated during the constant strain-rate portion is $t_p\dot{\gamma}_{max}$. For the loading pulse shapes considered here, the strains accumulated during the initial rise and during the unloading are

---

[4] A complete mathematical description of this idealized loading pulse is included in Appendix B.
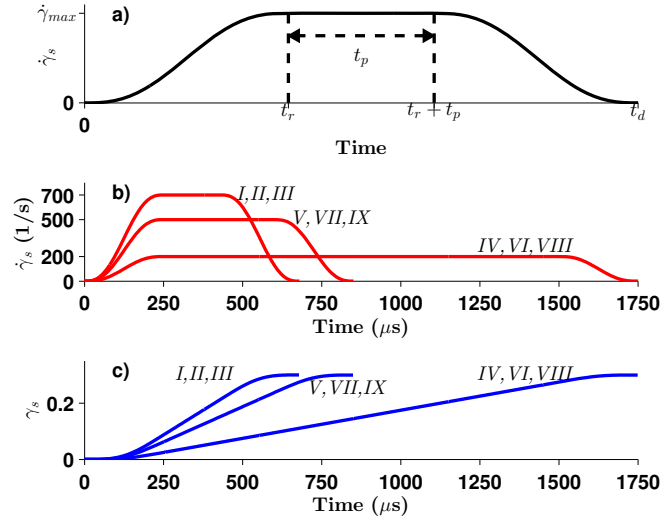
Figure 2. Key features of a typical average strain-rate history for the dynamic simulations (panel *a*). Average strain-rate histories (panel *b*) and strain histories (panel *c*) for *Simulations I–IX*.

each $\frac{1}{2} t_r \dot{\gamma}_{\max}$. Thus, the total average strain is

$$\gamma_{\max} = 2\left(\tfrac{1}{2} t_r \dot{\gamma}_{\max}\right) + t_p \dot{\gamma}_{\max} = (t_r + t_p)\dot{\gamma}_{\max}. \tag{2-8}$$

Nie et al. [2013] reported stress-strain curves from quasistatic and torsional Kolsky bar tests on five samples of bovine brain tissue. The Kolsky bar tests in [Nie et al. 2013] are described as being at a strain-rate of 700/s with a pulse duration of 600 μs. The final average shear strain for their tests was about 0.3. No additional details of the loading pulse are provided with the following exception. The reader is referred to their Figure 4 for "a typical set of Kolsky torsion bar result". This figure has plots of output voltage versus time for the two gages. The only information that we could infer from this figure is that the rise time of the loading pulse shown was about 250 μs.[5]

An *average* strain-rate history $\dot{\gamma}_s(t)$ consistent with the key features described above was obtained by choosing the imposed maximum (average) strain-rate $\dot{\gamma}_{\max}$ to be 700/s, the rise time t_r to this 700/s plateau to be 250 μs, and the maximum (average) strain $\gamma_{\max}$ to be 0.3. These conditions, together with (2-7) and (2-8), yield a plateau duration of $t_p = 179\,\mu$s and a loading pulse duration of $t_d = 679\,\mu$s. The curves for the one-dimensional *Simulations I–III* in Figure 2 show the average strain-rate history $\dot{\gamma}_s(t)$ (panel *b*) and the corresponding average strain history $\gamma_s(t)$ (panel *c*) obtained from this construction. The other two curves in these panels are the average strain and strain-rate histories for the one-dimensional *Simulations V, VII,* and *IX* and *Simulations IV, VI,* and *VIII*.

---

[5] From the discussion in [Nie et al. 2013], it is not clear whether the data in this figure corresponds to any of the tests in that paper or whether the data is taken from an earlier study by Nie et al. [2011] that is cited frequently in the 2013 paper. The earlier paper describes a *circular shearing test*, but it is referred to as a torsion test. Results from that paper are cited as providing evidence that the specimens were "undergoing uniform deformation" for the 700/s tests in [Nie et al. 2013], a claim that is contradicted by the results presented here.

parameter	unit	Simulation								
		I	II	III	IV	V	VI	VII	VIII	IX
$\gamma_{\max}$		0.3	—	—	—	—	—	—	—	—
$\dot{\gamma}_{\max}$	1/s	700	700	700	200	500	200	500	200	500
t_r	μs	250	—	—	—	—	—	—	—	—
t_p	μs	179	179	179	1250	350	1250	350	1250	350
t_d	μs	679	679	679	1750	850	1750	850	1750	850
ρ	g/cm^3	1	—	—	—	—	—	—	—	—
μ	kPa	800	80	8	8	8	80	80	800	800
c	mm/μs	0.0283	0.0089	0.0028	0.0028	0.0028	0.0089	0.0089	0.0283	0.0283
t_{travel}	μs	60.1	190.1	601	601	601	190.1	190.1	60.1	60.1

Table 2. Summary of material and loading pulse parameters for nine one-dimensional simulations. Long dashes (—) indicate parameters that were not changed.

2D. *One-dimensional torsion simulations.*

The one-dimensional linear elastic simulations described in Sections 3C, 3D, and 3F were conducted with the primary focus on the effects of the shear modulus and the loading pulse on the quality of the experiment. Table 2 summarizes the parameters specific to the nine one-dimensional simulations in Sections 3C and 3D. Columns 1 and 2 list the parameters and respective units, and the remaining columns give the values of the parameter used. The shear modulus was varied by two orders of magnitude: 800, 80, and 8 kPa, the latter being on the order of brain tissue, as discussed in Section 2A. These shear moduli are used in *Simulations I, II,* and *III*, respectively, together with the 700/s loading pulse discussed above. In Section 3C, the spatial and temporal variation of the actual shear strain and shear strain-rate in the specimen are compared for these three simulations.

In Section 3D, we compare the "stress-strain curves" for the same three shear moduli and three maximum (average) strain-rates (200, 500, and 700/s) for a total of nine simulations (*Simulations I–IX*). The 200/s and 500/s loading pulses had the same rise time (250 μs) and maximum strain (0.3) as the 700/s case but different plateau durations and total pulse durations (see Table 2 and Figure 2). The "stress-strain curves" presented here are obtained by plotting the average shear stress at the load cell versus the average shear strain in the specimen as in the experimental results reported by [Nie et al. 2013]. The errors introduced by this procedure are illustrated by comparison with the actual (linear) stress-strain curves that would have been obtained if the specimen were undergoing a uniform (i.e., pure torsional) deformation.

In Section 3F, we explore the plausibility of improving the quality of experimental results by changing the parameters of the loading pulse, specifically the rise time t_r and plateau duration t_p. In these studies, t_r took on the thirteen values 125, 250, 500, 750, 1000, 1250, 1500, 1750, 2000, 2250, 2500, 2750, and 3000 μs and t_p took on the eleven values 1, 100, 200, 300, 400, 500, 600, 700, 800, 900, and 1000 μs for a total of 143 additional one-dimensional simulations. These simulations were conducted on a soft material with the same geometry and material properties as in *Simulation III*.

Additional details about the numerical methods for the one-dimensional simulations are included in Appendix A.

2E. *Three-dimensional torsion simulations.*

In all of our three-dimensional simulations, stress-free boundary conditions were used on the outer surface $R = R_o$ and the inner surface $R = R_i$ of the annular specimen. With the exception of the viscoelastic results in Section 5B, the constitutive relation for the

specimen was a compressible version of the nonlinear elastic Mooney–Rivlin model (see Section 4). We used a bulk modulus of 2.3 GPa for all simulations; this is the bulk modulus of water and approximates the bulk modulus of many gelatins and soft tissues (such as brain tissue).

For the quasistatic simulations in Section 4F, the shear modulus was varied by almost three orders of magnitude: $\mu = 800, 80, 8$, and 2 kPa. The corresponding ratios of bulk to shear modulus varied from 2875 to 1.15×10^6 so that in all cases the material was nearly incompressible. For each value of the shear modulus, simulations were performed for three values of the nondimensional parameter ω in the Mooney–Rivlin model: 0.3, 0.6, and 1 (neo-Hookean model).

The three-dimensional dynamic simulations (*Simulations X–XVIII*) with an elastic specimen are discussed in Section 5A. The material parameters for these simulations were varied in an analogous way to the three-dimensional quasistatic simulations except that the $\mu = 2$ kPa case was not considered. The loading parameters were the same as in the one-dimensional *Simulations I–III*. Section 5B contains a brief discussion of some three-dimensional dynamic simulations that used a nonlinear viscoelastic model for the specimen.

Additional details about the numerical methods for both the quasistatic and dynamic three-dimensional simulations are included in Appendix A.

3. One-dimensional treatment of dynamic torsion

Unlike traditional Kolsky bar tests where the force or torque is measured at both ends of the specimen, in the modified torsional Kolsky bar test of [Nie et al. 2013], the torque is measured by a load cell at one end of the specimen only, and a (radially averaged) shear stress *at that end of the specimen* is extracted from this measurement. The test provides no means for determining whether an axially uniform state of shear stress has been achieved in the specimen. This would not be an issue if the shear strain could also be measured at the specimen-load cell interface, in which case a valid stress-strain curve could be obtained. However, it is not possible to measure the shear strain at any specific location in the specimen. Only an average measure of shear strain in the specimen, $\gamma_s(t)$ in (2-5), can be extracted from the test data, and this represents a volumetric average.[6]

As pointed out in the introduction, the stress-strain curves reported by [Nie et al. 2013] were obtained by plotting the (radially averaged) shear stress at the load cell versus the average shear strain $\gamma_s(t)$ in the specimen. Clearly, this is meaningful only if $\gamma_s(t)$ is close to the actual shear strain at the specimen-load cell interface. Such a condition can be expected to hold over some time interval only if the shear strain in the specimen is axially uniform on that time interval. In an effort to determine when a state of uniform shear strain can be achieved, we have performed one-dimensional simulations of dynamic torsion on linear elastic specimens. Although the goal of the torsional Kolsky bar tests is to measure strain-rate effects due to viscoelastic properties of the material, a study of one-dimensional linear elastic wave propagation in the torsion specimens reveals the difficulty in achieving uniform conditions in soft specimens.

In Section 3A, we discuss the one-dimensional wave equation that is solved in our simulations. Section 3B contains a brief discussion of dynamic equilibrium. An overview of the simulations in Sections 3C, 3D, and 3F was given in Section 2D. In Section 3E, we consider some ways of improving the quality of the torsion experiments.

---

[6] In this regard, see also (3-11) below.

3A. *The wave equation for dynamic torsion.* To investigate the possibility of axially nonuniform shear strains in dynamic torsion tests, we consider the torsional deformation

$$r = R, \qquad \theta = \theta(Z, t) = \Theta + \delta(Z, t), \qquad z = Z \tag{3-1}$$

so that

$$\delta(z, t) \equiv \theta(z, t) - \Theta \tag{3-2}$$

is the angular displacement at the axial location z at time t. Note that for the deformation (3-1) there are no axial or radial displacements in the specimen. The boundary conditions (2-2) imply that the angular displacements at the ends of the specimen are

$$\delta(L, t) = 0, \qquad \delta(0, t) = \theta(0, t) - \Theta = -\Psi(t) = -L\psi(t). \tag{3-3}$$

Recall that $\psi(t)$ is the *average* angle of twist per unit length (see (2-3)).

We assume that the displacement vector u and its spatial gradient ∇u are infinitesimal. Let ϵ denote the infinitesimal strain tensor: $\epsilon = \frac{1}{2}(\nabla u + (\nabla u)^T)$. Then for the deformation (3-1), the only nonzero components[7] of u and ϵ relative to the cylindrical coordinate system are

$$u_\theta = r\delta(z, t), \qquad \epsilon_{z\theta} = \epsilon_{\theta z} = \frac{1}{2}\frac{\partial u_\theta}{\partial z} = \frac{1}{2}r\frac{\partial \delta}{\partial z}. \tag{3-4}$$

We also assume that the specimen satisfies the isotropic linear elastic constitutive relation

$$T = \lambda(\operatorname{tr} \epsilon)I + 2\mu\epsilon, \tag{3-5}$$

where T is the Cauchy stress tensor and the constants λ and μ are the Lamé modulus and shear modulus, respectively. Then for the deformation (3-1), the only nonzero components of T are

$$T_{z\theta} = T_{\theta z} = 2\mu\epsilon_{\theta z} = \mu\frac{\partial u_\theta}{\partial z} = \mu r\frac{\partial \delta}{\partial z}. \tag{3-6}$$

In this case, the equations for momentum balance in cylindrical coordinates reduce to

$$\frac{\partial T_{\theta z}}{\partial z} = \rho\frac{\partial^2 u_\theta}{\partial t^2}, \tag{3-7}$$

where ρ is the specimen density. Then by (3-6), it follows that u_θ satisfies the one-dimensional wave equation; hence, by (3-4)$_1$ and (3-2), δ and θ satisfy the same equation.[8] For example,

$$\frac{\partial^2 \delta}{\partial t^2} = c^2\frac{\partial^2 \delta}{\partial z^2}, \qquad c = \sqrt{\frac{\mu}{\rho}}. \tag{3-8}$$

That is, a small angular displacement will propagate axially along the specimen at the linear elastic shear wave speed c.[9]

---

[7] Here and elsewhere in the paper, we use the physical components of vectors and tensors, that is, their components relative to the unit basis vectors along the cylindrical coordinate directions. See [Graff 1975, §A.9.1] for the physical components of ϵ and the momentum balance equations for infinitesimal strains.

[8] These results also follow from strength-of-materials approximations [Graff 1975, §2.6; Wylie 1975, §8.2].

[9] A shear wave propagating into an initially unstrained, *nonlinear* elastic material also travels at the linear elastic wave speed [Truesdell and Noll 1965, §73, 74, 77]. The shear wave speed may change after the wave is reflected and begins to travel into

The results above hold for both disc-shaped specimens and annular specimens.[10] In either case, the outer lateral surface $r = R_o$, and for annular specimens the inner lateral surface $r = R_i$, is stress-free since $T_{rr} = T_{r\theta} = T_{rz} = 0$. The shear strain $\epsilon_{\theta z}$ and the shear stress $T_{\theta z}$ vary linearly with the radius as shown above. Restricting attention to annular specimens, we see from (3-6) that the arithmetic average of the shear stress at the outer and inner lateral surfaces is

$$\sigma(z, t) \equiv \frac{T_{\theta z}|_{r=R_o} + T_{\theta z}|_{r=R_i}}{2} = \mu \bar{R} \frac{\partial \delta}{\partial z} = \mu \gamma(z, t), \tag{3-9}$$

where

$$\gamma(z, t) \equiv \bar{R} \frac{\partial \delta}{\partial z} = \bar{R} \frac{\partial \theta}{\partial z}. \tag{3-10}$$

Note that, by (3-4), $\gamma(z, t)$ is twice the arithmetic average of $\epsilon_{\theta z}(z, t)$ at the outer and inner lateral surfaces.[11] In interpreting the results of our one-dimensional simulations, we have chosen to use $\gamma(z, t)$ as a measure of the *radially averaged* shear strain at the axial location z for consistency with the average shear strain $\gamma_s(t)$ used in the experimental literature. Indeed, by (3-10), (3-3), and (2-5), $\gamma_s(t)$ is the axial average value of $\gamma(z, t)$:

$$\frac{1}{L} \int_0^L \gamma(z, t) \, dz = \frac{1}{L} \int_0^L \bar{R} \frac{\partial \delta}{\partial z} \, dz = \frac{\bar{R}}{L} [\delta(L, t) - \delta(0, t)] = \psi(t) \bar{R}$$
$$= \gamma_s(t). \tag{3-11}$$

Note that since $\gamma(z, t)$ represents a radial average of the shear strain at z, $\gamma_s(t)$ represents a volumetric average of the shear strain in the specimen.

Recall that, in the dynamic torsion tests, the angle of twist $\Psi(t)$ imparted to the face of the specimen (at $z = 0$) is typically determined in such a way that a desired average strain-rate history $\dot{\gamma}_s(t)$ is delivered. By (3-2) and (2-6), the angular displacement history necessary to deliver that average strain-rate history is

$$\delta(0, t) = -\frac{L}{\bar{R}} \gamma_s(t). \tag{3-12}$$

The average strain histories shown in Figure 2c, when substituted into (3-12), yield the angular displacement boundary conditions that are actually applied at the loading end of the specimen ($z = 0$) in our simulations. These simulations involve the numerical solution[12] of the one-dimensional wave equation (3-8) for δ with zero initial conditions and boundary conditions (3-12) and (3-3)$_1$ (i.e., $\delta(L, t) = 0$).

A *pure torsional deformation* satisfying the boundary conditions (2-2) is given by (3-1) with angular displacement

$$\delta(z, t) = \psi(t)(z - L), \quad \psi \geq 0. \tag{3-13}$$

---

a strained portion of the material. For the strains considered here, nonlinearity could introduce small variations in wave speeds that would be minor compared with other effects discussed later.

[10] Because of the small length-to-diameter ratio of the specimens considered here, namely 0.09, the more common terms "rod" and "tube" do not seem appropriate.

[11] For the annular specimens considered here, the shear strain should be approximately radially uniform. See the discussion of pure torsional deformation in Section 4B.

[12] Additional details about the numerical methods for the one-dimensional simulations are included in Appendix A.

In this case, by (3-4), the only nonzero components of the infinitesimal strain tensor are

$$\epsilon_{z\theta} = \epsilon_{\theta z} = \tfrac{1}{2} \psi(t) r \geq 0. \tag{3-14}$$

And by (3-10) and (2-5), the shear strain γ is axially uniform and equal to the average shear strain γ_s:

$$\gamma(z, t) = \psi(t) \bar{R} = \gamma_s(t) \quad \text{for pure torsion.} \tag{3-15}$$

However, a state of pure torsion might not be achieved in a given test so that $\gamma(z, t) \neq \gamma_s(t)$ in general. The degree to which $\gamma(z, t)$ differs from its measured average value $\gamma_s(t)$ is a critical point of this paper and is discussed in the following sections.

3B. *Dynamic equilibrium.* In the experimental literature, the terms "force equilibrium", "stress equilibrium", "dynamic stress equilibrium", or simply "dynamic equilibrium" are used to indicate that the axial forces (compression tests) or torques (torsion tests) on the two ends of the specimen are balanced [Gray 2000; Chen and Song 2011]. This condition is clearly necessary (but not sufficient) for an axially uniform state of stress and strain within the specimen, and in the experimental literature, these uniform conditions are often (implicitly) assumed to hold on any time interval for which dynamic equilibrium is achieved. We will use the term "dynamic equilibrium" in this stronger sense of axially uniform stress and strain states.

Whether or not dynamic equilibrium is reached depends on many factors, including the properties of the loading pulse, the specimen wave speed, and the specimen length. In particular, a critical factor in achieving dynamic equilibrium in torsion tests is the travel time of the shear wave:

$$t_{\text{travel}} = \frac{L}{c} = L \sqrt{\frac{\rho}{\mu}}, \tag{3-16}$$

that is, the time it takes for the shear wave to travel from one end of the specimen to the other. For a uniform strain state to exist in the material, key features of the loading pulse such as the rise time t_r and the plateau duration t_p need to be much longer than the travel time to allow the specimen to "ring-up" to dynamic equilibrium after multiple reflections.

Table 2 lists the three different travel times for *Simulations I–IX*; recall that we assume the density ρ is that of water and the specimen length L is 1.7 mm. For the values of the shear modulus used in our dynamic simulations (8–800 kPa), the travel time ranges from 601 μs to 60.1 μs. Since the travel time is the delay in microseconds between the initial loading of the specimen at $z = 0$ and the arrival of the wave at the load cell at $z = L$, the way this travel time is incorporated into the analysis of experimental data is extremely important when generating stress-strain curves as we will demonstrate in Section 3D. Assuming that the shear stress $\sigma(L, t)$ at the load cell is being plotted against the measured averaged shear strain $\gamma_s(t)$, these signals would have to be shifted in time to synchronize them. However, we will show that this procedure can introduce considerable errors.

3C. *Failure of soft specimens to reach equilibrium.* In this section, we examine the spatial and temporal variation of the strain and strain-rate in the specimen for *Simulations I–III*. These simulations differ only in the value of the shear modulus μ used for the specimen (see Table 2). The results are summarized in Figure 3. False color images of the strain-rate (left panels) and strain (right panels) as a function of axial
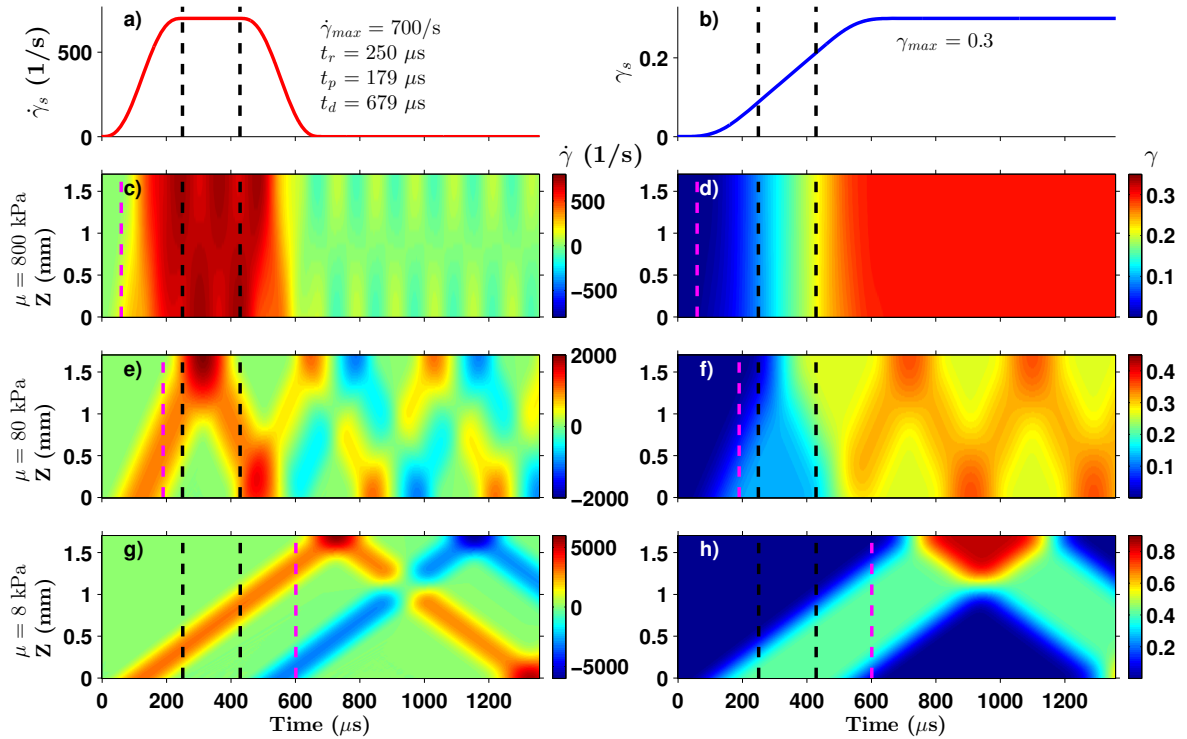
Figure 3. The average strain-rate history $\dot{\gamma}_s(t)$ (panel *a*) and corresponding average strain history $\gamma_s(t)$ (panel *b*) imposed on the specimen for *Simulations I–III*. The first black vertical dashed line corresponds to the rise time t_r to constant strain-rate. The second black vertical dashed line is the time $(t_r + t_p)$ at which the strain-rate starts to ramp down after a constant strain-rate plateau of duration t_p. The remaining panel pairs (*c–d*, *e–f*, and *g–h*) are false color images of the corresponding actual strain-rates $\dot{\gamma}(z, t)$ and strains $\gamma(z, t)$ in specimens with shear moduli $\mu = 800$, 80, and 8 kPa, respectively. Note that the color scale varies for the three groups of plots. The vertical magenta lines correspond to t_{travel}, which depends on the shear modulus.

position (vertical axis) and time are presented in panels *c–h*. Panels *a* and *b* show the *average* strain-rate and strain histories that are imposed on the specimen.

Figure 3 illustrates the degree to which dynamic equilibrium has (or has not) been achieved. Shear waves are initiated at the specimen–bar interface ($z = 0$) and propagate to the *Load Cell* ($z = L$). In each panel, the first vertical black dashed line indicates the rise time t_r. The two vertical black dashed lines taken together represent the window of time during which the imposed average strain-rate is constant. The vertical magenta dashed line indicates the travel time and thus the arrival of the shear wave at the *Load Cell*, which increases with decreasing shear modulus (see (3-16)). Thus, the black dashed lines indicate the key time scales of the loading pulse and the magenta line represents the critical travel time of the specimen. Ideally, the magenta line should lie well before both black lines.

The results for $\mu = 800$ kPa (*Simulation I*) are shown in panels *c* and *d* of Figure 3. These results are close to what one might expect for a valid torsional Kolsky bar experiment. The strain-rate (panel *c*)

increases to an approximately axially uniform (intended) plateau value of 700/s before dropping back down to a zero strain-rate but nonzero final strain (panel d). From the false-color representation, one can conclude that both the strain and strain-rate are fairly uniform along the length of the specimen at any instant. This is indicated by a nearly uniform color in the vertical direction at any instant. The ringing that can be seen, especially in the strain-rate, is one of the fundamental modes of the specimen. There is moderate variability in the strain-rate due to the ringing, but the intended strain-rate and maximum strain nearly match their imposed average values plotted in panels a and b. Thus, panels c and d in Figure 3 are a representation of a strain state where dynamic equilibrium is nearly achieved. If dynamic equilibrium was actually reached, the color representation of $\gamma(z, t)$ and $\dot{\gamma}(z, t)$ would not change in the vertical direction.

The results for the smaller shear modulus, $\mu = 8\,\text{kPa}$ (*Simulation III*), are shown in panels g and h of Figure 3. Clearly, the strain and strain-rate in *Simulations III* and *I* are considerably different both in magnitude and uniformity. Recall that a shear modulus of 8 kPa is on the order of brain tissue, so the specimen stiffness in this case most closely resembles the stiffness of the brain tissue specimens in the tests of [Nie et al. 2013]. Since the linear elastic shear wave speed is proportional to the square root of the shear modulus and the shear modulus in *Simulation III* is one hundred times smaller than in *Simulation I*, the wave speed is ten times slower than in *Simulation I*. The travel time is therefore ten times longer, i.e., $601\,\mu\text{s}$ instead of $60\,\mu\text{s}$ (compare the magenta lines for panels c and d against panels g and h in Figure 3). For the $\mu = 8\,\text{kPa}$ case, the travel time is so close to the pulse duration ($t_d = 679\,\mu\text{s}$) that the shear strain and shear strain-rate within the specimen are nonuniform traveling pulses. Thus, *the same loading conditions* that produced axially uniform shear strain and shear strain-rate in the $\mu = 800\,\text{kPa}$ case resulted in highly nonuniform shear strain and shear strain-rate within the 8 kPa specimen.

For the $\mu = 8\,\text{kPa}$ case, it is grossly inaccurate to describe the strain and strain-rate at any location in the specimen by their average values γ_s and $\dot{\gamma}_s$ although these averages are all that can be inferred from test measurements. The following features illustrate the degree of nonuniformity in the specimen:

(1) During the first $600\,\mu\text{s}$ of the simulation, that is, prior to reflection of the shear wave from the *Load Cell*, the peak strain-rate and peak strain in the specimen are about 3200/s and 0.42, respectively. These peak values occur at different axial locations at different times (see panels g and h) and well exceed the maximum average strain-rate ($\dot{\gamma}_{\text{max}} = 700/\text{s}$) and maximum average strain ($\gamma_{\text{max}} = 0.3$).

(2) The largest strain achieved in the specimen during the simulation is about 0.84. This occurs near the end $Z = 1.7\,\text{mm}$ (i.e., adjacent to the *Load Cell*) at about $900\,\mu\text{s}$ (panel h). This peak strain is nearly three times larger than the average strain γ_s at $900\,\mu\text{s}$, which has already reached its final value of $\gamma_{\text{max}} = 0.3$.

(3) The largest strain-rate achieved in the specimen during the simulation is about 5800/s. This also occurs at the *Load Cell* end of the specimen ($Z = 1.7\,\text{mm}$) at about $730\,\mu\text{s}$, by which time the average strain-rate $\dot{\gamma}_s$ has unloaded to zero. This peak strain-rate is more than eight times higher than the maximum average strain-rate (700/s) imposed on the specimen.

(4) Large positive strain-rates and a zero *average* strain-rate at the same instant imply negative strain-rates of large absolute value must also be experienced in some portions of the specimen. This is evidenced by the blue bands in panel g.

(5) The doubling of the peak strains (from 0.42 to 0.84) and the near doubling of the peak strain-rates

(from 3200/s to 5800/s) is due to the reflection of the shear wave from the fixed end ($Z = 1.7$ mm) beginning at 601 μs.[13]

(6) As an example of the large axial gradients, the strain at 300 μs decreases from 0.275 to 0 over a distance of 0.3 mm. However, the change in the angle of twist over this 0.3 mm length is quite small: roughly 0.005 radians or about 0.3°. This is well below the resolution of the high speed camera images of the specimen in [Nie et al. 2011] that were often cited in [Nie et al. 2013] as evidence that the specimens undergo uniform deformation.

The results for $\mu = 80$ kPa (*Simulation I*) are shown in panels *e* and *f* of Figure 3. Even for this intermediate case, dynamic equilibrium is not reached. Further evidence of this fact is given by the stress-strain curves for $\mu = 80$ kPa in the next section. Clearly, achieving dynamic equilibrium in specimens with shear moduli substantially less than 800 kPa can be quite problematic.

3D. *"Stress-strain curves" for linear elastic specimens.* Up to this point, we have used the linear elastic simulations only for predictions of the strain and strain-rate within the specimen. In this section, we use the results of those simulations to construct "stress-strain curves" at several "constant strain-rates", analogous to the way that test data is typically analyzed and presented in the experimental literature.

Let $\sigma_{\text{Load Cell}}(t)$ and $\gamma_{\text{Load Cell}}(t)$ denote the (radially averaged) shear stress and shear strain at the *Load Cell*:

$$\sigma_{\text{Load Cell}}(t) = \sigma(L, t), \qquad \gamma_{\text{Load Cell}}(t) = \gamma(L, t). \qquad (3\text{-}17)$$

In the torsional Kolsky bar test of [Nie et al. 2013], the torque is measured at the load cell and $\sigma_{\text{Load Cell}}(t)$ can be extracted from this measurement. However, $\gamma_{\text{Load Cell}}(t)$ cannot be measured in this or any other torsional Kolsky bar test — only the average shear strain $\gamma_{\text{s}}(t)$ can be inferred as discussed in Section 2B. Consequently, the stress-strain curves in [Nie et al. 2013] are plots of $\sigma_{\text{Load Cell}}$ versus γ_{s}. But while $\gamma_{\text{s}}(t)$ starts increasing at $t = 0$, that is, as soon as the twist is applied to the end $z = 0$, there is a delay (equal to the travel time) before a nonzero strain is experienced by the specimen at the load cell (see Figure 3). Since this travel time is a significant portion of the test duration for the soft specimens of interest, it might seem reasonable to time-shift the $\sigma_{\text{Load Cell}}(t)$ history in order to synchronize it with the $\gamma_{\text{s}}(t)$ history (or vice versa) prior to plotting one against the other. On the other hand, *a time shift is unnecessary if the specimen is in dynamic equilibrium*, a condition that Nie et al. [2013] assumed to hold in their tests. Since the issue of travel time in the specimen was not discussed in their paper, it was not clear to us whether a time shift had been performed in generating their stress-strain curves.

In this section, we utilize the results from *Simulations I–IX* (see Table 2) to generate "stress-strain curves" (i.e., $\sigma_{\text{Load Cell}}$ versus γ_{s}) with and without time shifts. We compare the results of both approaches in order to illustrate the different apparent "strain-rate effects" that each produces. Recall that the simulations solve the one-dimensional wave equation (3-8) for the angular displacement δ with the boundary condition at $z = 0$ determined by the appropriate average strain history (see (3-12) and Figure 2). Six sets of "stress-strain curves" are plotted in Figure 4. Solid colored curves are shear stress measured at the *Load Cell* plotted against the average shear strain γ_{s}. The colored curves in the left column do not involve any time shifts of the data; i.e., they are parametric plots of $\sigma_{\text{Load Cell}}(t)$ versus $\gamma_{\text{s}}(t)$. The colored

---

[13] Another doubling would be expected to occur at the specimen-bar interface ($Z = 0$) if the simulation had been continued to longer times.

curves in the right column are parametric plots of $\sigma_{\text{Load Cell}}(t - t_{\text{travel}})$ versus $\gamma_s(t)$; i.e., the *Load Cell* data has been time-shifted to synchronize it with the average strain data. Each row of plots is for a unique shear modulus (800, 80, and 8 kPa), and each color within a panel represents a simulation taken at a different intended maximum *average* strain-rate: $\dot{\gamma}_{\text{max}} = 700/\text{s}$ (blue), $500/\text{s}$ (green), and $200/\text{s}$ (red). The average strain-rate histories are shown in panel *b* of Figure 2. The maximum strain γ_{max} and rise time were held constant at 0.3 and $250\,\mu\text{s}$, respectively, and only the plateau time and the total duration were changed to accommodate the various strain-rates (see Table 2).

In the simulations the stress and strain at the *Load Cell* are linearly related: setting $z = L$ in (3-9) gives

$$\sigma_{\text{Load Cell}}(t) = \mu \gamma_{\text{Load Cell}}(t). \tag{3-18}$$

Thus, regardless of the strain and strain-rate histories experienced by the specimen, a parametric plot of $\sigma_{\text{Load Cell}}(t)$ versus $\gamma_{\text{Load Cell}}(t)$ should be linear with slope μ. We cannot actually plot the linear relation in (3-18) in Figure 4 since the variable on the horizontal axis is $\gamma_s(t)$, which (as shown in Section 3C) is generally not equal to $\gamma_{\text{Load Cell}}(t)$. However, if the shear strain were uniform, then γ_s would coincide with $\gamma_{\text{Load Cell}}$, in which case the shear stress at the *Load Cell* would vary linearly with γ_s: $\sigma_{\text{Load Cell}} = \mu \gamma_s$. This linear curve is shown by the black dashed lines in each panel in Figure 4. It represents *the correct stress-strain curve* against which the colored "rate-dependent" curves should be compared. That is, while each of the colored curves are valid plots of $\sigma_{\text{Load Cell}}$ versus γ_s (with or without time shifts), they represent the $\sigma_{\text{Load Cell}}$ versus $\gamma_{\text{Load Cell}}$ curve only to the extent to which they agree with the black dashed lines in Figure 4. Recall that the shear strain $\gamma(z, t)$ is uniform for a specimen undergoing a pure torsional deformation (see the discussion at the end of Section 3A). Hence, the black dashed lines represent the stress-strain curves that would be obtained for pure torsion.

Panel *a* in Figure 4 corresponds to a shear modulus of 800 kPa without a time shift. Note that all four curves lie nearly on top of each other. Here the blue curve represents the results from *Simulation I*. As discussed earlier, this was considered a "valid" Kolsky bar test, and that conclusion is confirmed here. Panel *b* is the same set of stresses shifted by the travel time ($60\,\mu\text{s}$). This has the *appearance* of valid Kolsky bar data. Note, however, that all these curves are vertically offset from the true (dashed) response, implying an apparent rate-dependence. Despite the vertical offset, their slopes capture the true linear behavior of the material.

We emphasize that if a linear elastic specimen is in dynamic equilibrium, there should be absolutely no strain-rate effects. However, Figure 4 clearly shows that, for the smaller shear moduli of 80 and 8 kPa, the apparent "rate effects" are substantial regardless of whether the *Load Cell* data is time-shifted. It is unclear what information could have been inferred from these plots if the true linear stress-strain relation were unknown with the exception that, for $\mu = 80$ kPa, a linear fit to the unshifted curves or to the time-shifted 200/s curve might return a slope close to μ.

When the shear stress is plotted without a time shift, there is an initial strain interval for which the stress is zero. The strain duration of this initially flat portion of the stress-strain curve increases with the strain-rate and decreases with increasing shear modulus. These initially flat regions are present even for the $\mu = 800$ kPa case (panel *a*) although they cannot be observed on the scale of that figure. This nonphysical behavior is most profound for the softest specimen ($\mu = 8$ kPa, panel *e*). In particular, for the 700/s case in that panel, there is no measured stress until $\gamma_s(t)$ is close to 0.3. Recall that it takes $601\,\mu\text{s}$ for the shear wave to arrive at *Load Cell* whereas the average strain has reached its final value
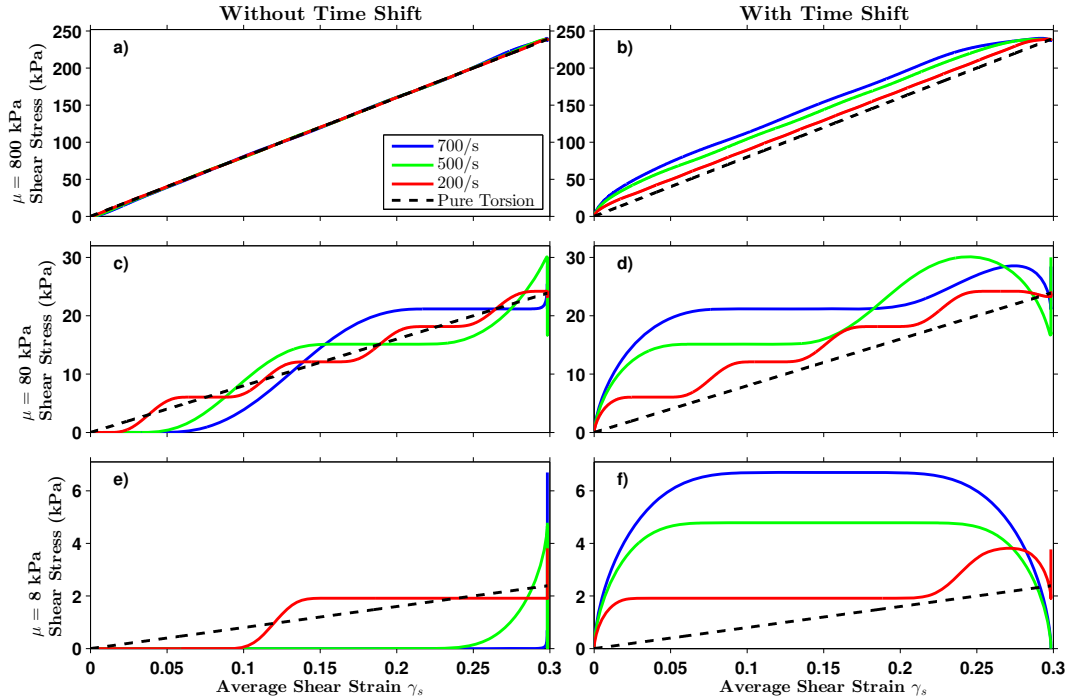
Figure 4. Panel pairs *a–b*, *c–d*, and *e–f* show apparent "strain-rate effects" in three linear elastic materials with shear moduli $\mu = 800$, 80, and 8 kPa, respectively. Note the differences in the vertical scales for the three groups of panels. Solid colored curves are shear stress measured at the *Load Cell* plotted against the average shear strain γ_s. The black dashed lines correspond to the stress-strain curve that results for a pure torsional deformation in dynamic equilibrium.

of 0.3 by 679 μs (the pulse duration). For $t > t_{\text{travel}} = 601$ μs, the strain at the *Load Cell* increases to roughly 0.8 (see panel *h* in Figure 3) and subsequently falls to zero strain, and of course, the stress at the *Load Cell* is proportional to this strain. Thus, a parametric plot of $\sigma_{\text{Load Cell}}(t)$ versus $\gamma_s(t)$ becomes essentially a vertical line at $\gamma_s = 0.3$, where a single average shear strain maps to infinitely many stresses.

When the $\mu = 80$ and 8 kPa data is plotted with a time shift (panels *d* and *f* in Figure 4), the data *appears* more reasonable but is still completely erroneous. In particular, the "initial" shear moduli (that is, the slopes of the stress-strain curves at the origin) are substantially higher than the actual shear modulus of the linear elastic specimen, which is the slope of the dashed curve. For strains up to 0.05, our 700/s curves (for $\mu = 8$ and 80 kPa) agree qualitatively, though not quantitatively,[14] with the 700/s stress-strain curves for bovine brain tissue in Figures 5 and 6 of [Nie et al. 2013]. In particular, their stress-strain curves have no initially flat region of the type in panels *c* and *e* in our Figure 4. Based on these observations, it would appear that Nie et al. [2013] time-shifted the *Load Cell* data to synchronize it with the average strain data in order to generate the stress-strain curves for the "700/s" tests that they reported. But regardless

---

[14] Our linear elastic simulations for $\dot{\gamma}_{\text{max}} = 700$/s were not intended or expected to *fit* the 700/s stress-strain curves in [Nie et al. 2013]. Their quasistatic curves show large nonlinear elastic effects that would be expected to persist in dynamic tests.

of whether they time-shifted their *Load Cell* data, the results in this section indicate that the stress-strain curves reported for bovine brain tissue in [Nie et al. 2013] most likely have large systematic errors in the strains. The results in the next paragraph lend further support for this conclusion.

The 700/s curve in Figure 6 of [Nie et al. 2013] is an average of the 700/s stress-strain curves for their five samples. From this curve, they estimated an (average) initial shear modulus of 53.5 kPa. If this were an accurate estimate of the instantaneous elastic shear modulus of a *viscoelastic* specimen, then the shear wave speed in the specimen would be controlled by this modulus, giving a travel time in the specimen of 232 μs. Our $\mu = 80$ kPa elastic simulations are closest to this case with an even shorter travel time of 190 μs. However, as panels *c* and *d* in Figure 4 and panels *e* and *f* in Figure 3 show, dynamic equilibrium is not reached even for this stiffer case.

It is clear that the apparent "rate effects" discussed here are not due to viscoelastic or viscoplastic behavior in the specimen. Rather, they are due to the fact that the average shear strain, which is used to construct the stress-strain curves, is significantly different from the strain at the location where the stress is measured. However, in a Kolsky bar test on specimens that exhibit rate-dependent behavior, the distinction between the actual material response and apparent "rate effects" would be lost. Thus, one might falsely attribute the apparent rate effects discussed above to either viscoelastic or viscoplastic properties of the specimen.

After this portion of the paper had been completed, private communications with Xu Nie (the first author of [Nie et al. 2013]) suggested some possibilities that were not considered above. Nie stated that in generating their stress-strain curves, they did not time-shift the *Load Cell* data to synchronize it with the average strain data.[15] Furthermore, he estimated that the travel time in the specimen was approximately 30 μs. This estimate was obtained from the difference between the arrival time of the loading wave at the specimen and the onset of a signal at the *Load Cell*. These times were estimated from oscilloscope traces from one test.[16] Clearly, a travel time of 30 μs is inconsistent with the results presented here for a specimen as soft as brain tissue. Indeed, it would imply an instantaneous elastic shear modulus of 3.2 MPa, which is totally unreasonable for brain tissue.

On examining a snapshot of the oscilloscope traces provided to us by Xu Nie, we noticed that there was a discontinuity in the slope of the *Load Cell* signal at about 260 μs.[17] Subsequently, the *Load Cell* signal exhibits a substantial increase in noise. We suspect that the travel time of the *torsional shear wave* in the specimen was (approximately) 260 μs and that the onset of the *Load Cell* signal at 30 μs is due to some other source. Note that a travel time of 260 μs would imply an instantaneous elastic shear modulus of 42 kPa, which is not unreasonable. The early *Load Cell* signal would also explain why the stress-strain curves in [Nie et al. 2013] do not exhibit an initially flat region even though they claim that the data was plotted without a time shift. Indeed, no such region is observable in panel *a* of Figure 4 even though the travel time in that case was 60 μs. If our conjecture is correct, then the shear stress inferred from the

---

[15] They did, of course, perform the necessary time shift of the strain gage data to account for the time it takes the shear wave to propagate from the strain gage to the specimen end of the incident bar.

[16] Nie points out (and we agree) that such estimates for arrival and onset times, and particularly for their differences, are subject to errors that are difficult to bound. Our estimate of the actual travel time of the shear wave, and consequently our estimate for the instantaneous elastic shear modulus for the specimen, are subject to even more uncertainty. However, it is only the order of magnitude of these estimates that are essential for the arguments given here.

[17] To simplify the discussion, we take the arrival time of the loading wave at the specimen to be $t = 0$ as has been assumed previously this paper.

Load Cell signal would be erroneous from 30–260 μs (and hence for the smaller strains), and possibly for later times as well, depending on how long this spurious signal persisted.

A possible explanation for the early onset of the *Load Cell* signal is the presence of bending or longitudinal waves in the incident bar, which would travel faster than the torsional shear wave. Another possible explanation is the longitudinal precursor wave that is generated in the specimen by the shearing deformation from the torsional wave. This precursor wave is a real effect as discussed in the analysis of our three-dimensional dynamic simulations in Section 5. But it is not clear to us whether any of these waves could even generate a measurable signal in the *torque* sensor, so at the moment, the early onset of this signal remains unresolved.

3E. *Increasing the quality of the test.* In the previous sections, we examined the axially nonuniform strain and strain-rate states that may exist in the specimen in torsional Kolsky bar tests. For sufficiently soft specimens, large systematic error in the stress-strain curves is associated with the loading conditions and the specimen lengths considered. In this section, we discuss some alterations to the experiment that might alleviate this error. Some dimensional analysis is particularly useful here and can indicate how to improve the experimental setup.

Using parameters specific to our loading pulse, by (2-7) and (2-8), we see that the total average strain and the pulse duration can be expressed as

$$\gamma_{\max} = (t_r + t_p)\dot{\gamma}_{\max}, \qquad t_d = 2t_r + t_p = t_r + \frac{\gamma_{\max}}{\dot{\gamma}_{\max}} = 2\frac{\gamma_{\max}}{\dot{\gamma}_{\max}} - t_p. \qquad (3\text{-}19)$$

If we take $\dot{\gamma}_{\max}$ as fixed, we need only specify two of the three parameters t_r, t_p, and $\gamma_{\max}$ in order to determine the four parameters t_r, t_p, $\gamma_{\max}$, and t_d. We choose to track changes by altering the rise time t_r and the plateau duration t_p.

Two quality measures of the test conditions are the ratio Q_r of the rise time to the travel time and the ratio Q_p of the plateau time to the travel time:

$$Q_r \equiv \frac{t_r}{t_{\text{travel}}} = \frac{ct_r}{L} = \frac{t_r}{L}\sqrt{\frac{\mu}{\rho}}, \qquad Q_p \equiv \frac{t_p}{t_{\text{travel}}} = \frac{ct_p}{L} = \frac{t_p}{L}\sqrt{\frac{\mu}{\rho}}. \qquad (3\text{-}20)$$

Q_r can be thought of as the number of wave reflections that occur during the initial rise time, and Q_p can be thought of as the number of reflections that occur during the plateau period. A high quality test would be one for which both $Q_r \gg 1$ and $Q_p \gg 1$. We emphasize that these measures are dimensionless and depend on the details of the loading pulse, the specimen length, and the shear wave speed of the specimen.

For a given range of values of the shear wave speed c, the parameters L, t_d, t_r, t_p, $\gamma_{\max}$, or $\dot{\gamma}_{\max}$ can be chosen to ensure a large quality factor. The $\mu = 800$ kPa case in Figure 4 (panel *a*) gave the most accurate results; here $Q_r = 4.2$ for all three cases, and $Q_p = 2.98$, 5.82, and 20.8 for $\dot{\gamma}_{\max} = 700$/s, 500/s, and 200/s, respectively. For our particular examples, transitioning from $\mu = 800$ kPa to $\mu = 8$ kPa reduces the wave speed by a factor of ten. This also reduces Q by a factor of ten.[18] Thus, to perform a valid experiment, the parameters that determine Q need to be adjusted in the softer material case to compensate for the slower wave speed and thus restore Q to a larger value.

An obvious change to make is reducing the specimen length. Although in practice this might be quite difficult for brain tissue, reducing the length (i.e., thickness) of the specimen by a factor of 10 (from 1.7

---

[18]The symbol Q without an r or p subscript refers to *both* Q_r and Q_p.

to 0.17 mm) would increase Q by a factor of 10. However, by reducing the length, inhomogeneities in the tissue are more likely to influence measurements. There are also practical concerns: how to cut slices that are submillimeter, how to handle them, and the effects of gluing them.

Another means of increasing the quality Q_r is to increase the rise time of the loading pulse. To increase Q_r by a factor of 10 without reducing the specimen length, t_r must also increase by a factor of 10; i.e., we need $t_r = 2500\,\mu$s. From $(3\text{-}19)_1$, we see that this can be achieved by reducing the maximum (average) strain-rate $\dot{\gamma}_{\max}$ or by increasing the maximum (average) strain $\gamma_{\max}$. However, in an actual torsion test, buckling or tearing is likely to occur at sufficiently large strain. Similar comments apply to Q_p and t_p.

There are experimental constraints on the duration of the loading pulse, namely the bar length, bar wave speed, and location of the strain gage on the bar. Attempting to accommodate a long (e.g., 7 ms) loading pulse for an aluminum or steel bar by only increasing its length would yield impractical bar lengths. However, a considerable increase in loading pulse duration can be gained by switching to polymer bars without changing the length of the bar. For example, polycarbonate (PC) and polymethyl methacrylate (PMMA) have shear wave speeds of 0.91 mm/μs and 1.3 mm/μs, respectively. Compared to aluminum or steel bars, which have shear wave speeds on the order of 3 mm/μs, the longest pulse for a fixed length of bar would be increased by 3.6 and 2.5 for a PC and a PMMA bar, respectively.

Additional gains can be made in accommodating longer loading pulses by replacing the strain gage with an optical measurement of the angle of twist imposed on the specimen. The traditional analysis of Kolsky bar test data uses the fact that the average strain-rate in the specimen is proportional to the strain generated in the incident bar by the reflected wave, *assuming the specimen is in dynamic equilibrium*; see (7) in [Gilat 2000] for torsion tests and [Gray 2000; Chen and Song 2011] for compression tests. For sufficiently long loading pulses, however, the incident and reflected waves can overlap at the strain gage location, in which case the reflected wave signal cannot be separated from the combined signal, making it impossible to extract the strain in the incident bar associated with the reflected wave.[19] This would no longer be an issue with an optical measurement of the angle of twist at the end of the incident bar adjacent to the specimen. Also, since the specimens could not have been in dynamic equilibrium in the tests of [Nie et al. 2013], the method discussed above for determining the strain-rate in the specimen can be called into question. This issue would also be bypassed by direct optical measurement of the angle of twist.

3F. *A parametric study of test quality.* In view of the discussion in the previous section, we conducted a parametric study in which t_r and t_p were varied in an attempt to increase the quality of the test within the experimental constraints. For these simulations, we used $\dot{\gamma}_{\max} = 700/$s, $\mu = 8$ kPa, and $L = 1.7$ mm. With these parameters fixed, and varying only the rise time and plateau time, we present in Figure 5 the results on the peak strain reached at the *Load Cell* during the simulation (panel *a*), the total duration of the loading pulse (panel *b*), and the average error (panel *c*) as defined below.

Equation (3-19) predicts that, for a fixed maximum average strain-rate $\dot{\gamma}_{\max}$, the maximum *average* strain $\gamma_{\max}$ depends linearly on the sum of t_r and t_p. In panel *a*, the *actual peak strain* in the specimen at the *Load Cell*, max$[\gamma]$, i.e., the maximum value of $\gamma(L, t)$ over the duration of the experiment, deviates

---

[19] This was one of the difficulties encountered by Nie et al. [2013]. They partially bypassed the problem by substituting the (negative of the) incident wave for the reflected wave, arguing that this is a good approximation for very soft specimens, which in fact it may be. They could then use the measured strain in the incident bar due to the incident wave at least up until the time of arrival of the reflected wave.
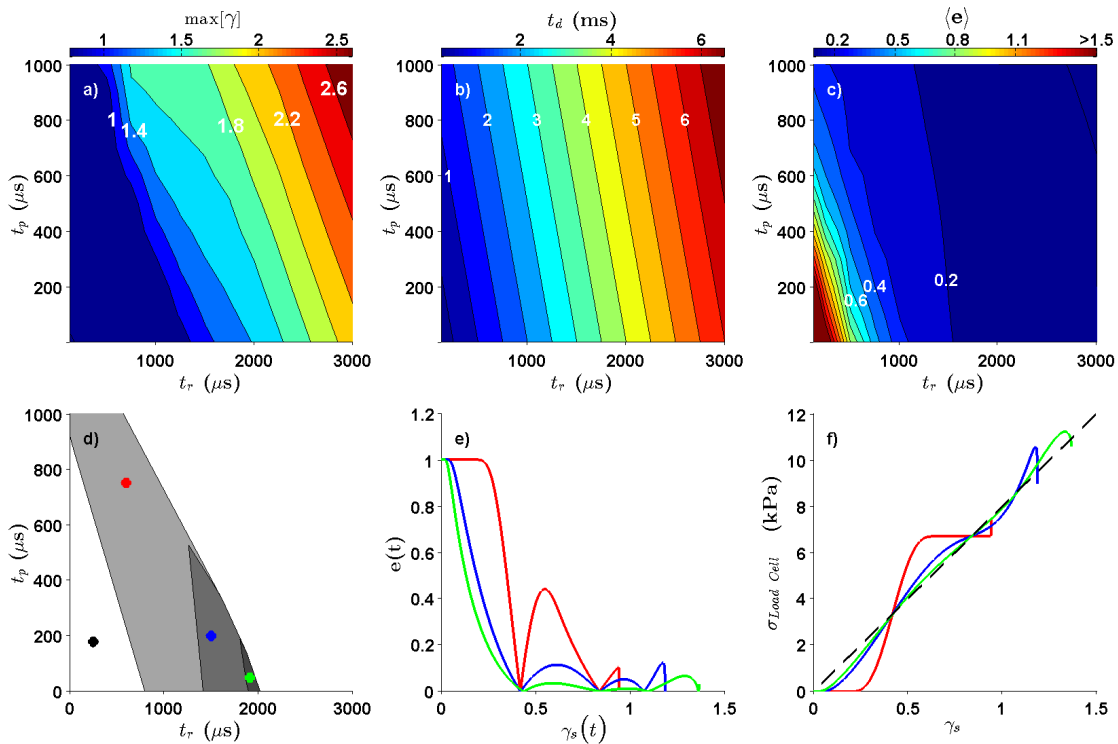
Figure 5. Panels *a–c* show the effects of varying the rise time t_r (horizontal axis) and the plateau time t_p (vertical axis) for $\dot{\gamma}_{\max} = 700/s$ tests on a linear elastic specimen with shear modulus 8 kPa. Through false-color images, these panels show the peak strain reached at the *Load Cell* during a simulation (max[γ], panel *a*), the total loading pulse duration t_d (panel *b*), and the average error $\langle e \rangle$ in the strain (see text, panel *c*). Panel *d* shows the regions where the peak strain is less than 1.5, the total pulse duration less than 5 ms, and the average error less than 40%, 20%, and 15% in darkening shades of gray. The black dot represents *Simulation III*, which most closely resembles the test conditions in [Nie et al. 2013]. The red, blue, and green circles are sample test conditions taken in each region. Additional results for these test conditions are given in panels *e* and *f*. Panel *e* is a plot of *e*(*t*) (the relative error in the strain at the *Load Cell*) versus the average imposed strain $\gamma_s(t)$. Panel *f* shows the resultant stress-strain curves. The black dashed line represents the ideal to which these curves should be compared, that is, the curve that would have been produced if $\gamma_s(t)$ coincided with $\gamma_{\text{Load Cell}}$.

from this simple behavior. This is most clearly seen for the smaller values of t_r and t_p. For example, when $t_r = 250\,\mu s$ and $t_p = 179\,\mu s$, the maximum average strain $\gamma_{\max} = 0.3$, but the peak strain is close to 1 (*Simulation III*). These larger strains, as discussed in the previous section, are from a failure to achieve dynamic equilibrium.

Panel *b* shows the dependence of the pulse duration t_d on the rise time and plateau time, also given by (3-19). This panel is relevant to the constraints introduced from the lengths of the bars in a Kolsky bar experiment. As discussed earlier, a 7 ms long pulse may be unmanageable in an aluminum or steel bar.

Since there are nonuniform strains experienced in the specimen, there is an error associated with assuming that the measured average shear strain $\gamma_s(t)$ is equal to the shear strain at the *Load Cell*, $\gamma(L, t)$. We therefore take the relative error in the strain measurement at time t to be

$$e(t) = \frac{|\gamma(L, t) - \gamma_s(t)|}{\gamma_s(t)}. \tag{3-21}$$

This error is time-dependent and is small when near-uniform conditions exist within the specimen. Since $\gamma(L, t) = 0$ prior to the arrival of the shear wave at the *Load Cell*, the value of the error $e(t)$ in (3-21) is 1 for all times less than the travel time. We ignore the error during these early times since we hold the travel time fixed in this section. We define an average error by using the time average of its value starting after the travel time until a later time $t_{\max}$

$$\langle e \rangle = \frac{1}{t_{\max} - t_{\text{travel}}} \int_{t_{\text{travel}}}^{t_{\max}} e(t) \, dt. \tag{3-22}$$

Qualitatively similar results were found for various values of $t_{\max}$, and in what follows, we chose a large integration window where $t_{\max} = 15 \, \text{ms}$ (roughly twice the value of the longest pulse duration considered). Thus, the average error is an estimate of the sensitivity of a torsion test to the parameters of the loading pulse.

Panel c in Figure 5 presents the dependence of the average error $\langle e \rangle$ on the rise time and plateau time. This panel clearly shows that error is reduced by increasing both the rise time and the plateau time as suggested by (3-20) although it depends most critically on the rise time. For sufficiently large rise times, the effects of the plateau time become negligible.

Combining the limitations introduced by the specimen in terms of maximum allowable strain, the constraint from bar lengths in terms of total duration of the pulse, and the acceptable error in the measurement, we can determine whether it is possible to design an experiment that reaches dynamic equilibrium for a given imposed average strain-rate. The small dark gray region in panel d in Figure 5 (small triangular region near $t_r = 2000 \, \mu\text{s}$) represents the rise and plateau times where the peak strain at the *Load Cell* is less than 1.5, the loading pulse duration is less than 5 ms, and the average error is less than 15%. The two neighboring lighter shades of gray correspond to the regions where rise and plateau times satisfy the same requirements in peak strain and loading pulse duration but relax the average error constraint to 20 and 40%. Although not clear in the presentation of the colored regions, these regions overlap so that the light gray region extends "underneath" the two darker shades of gray, and the medium gray region extends under the dark gray region (but not under the light gray). An average strain of 1.5 corresponds to roughly a 17° rotation of one end of the specimen with dimensions given in Table 2. Achieving a pulse that is 5 ms long would require a *polymer bar* approximately 5 m long, depending on how the strain was measured. The error bounds were taken fairly loosely since actual error is time-dependent and therefore depends on the average imposed strain γ_s. The red, green, and blue circles in panel d are three sample test conditions, one taken in each region of error. The black dot outside the gray regions represents *Simulation III*, which most closely resembles the test conditions in [Nie et al. 2013].

Panel e in Figure 5 is the error $e(t)$ plotted against the imposed average strain $\gamma_s(t)$ for the three sample test conditions discussed above. This panel shows that, even for the most accurate test (green line), the initial ring-up period extends until moderate strains of about 0.4 are reached. This means that even in

these experiments the small and moderate strain region of the stress-strain curve would be unreliable. Panel f shows the resultant stress-strain curves from each of the color-coded simulations. Here, as in Figure 4, the black dashed line represents the ideal to which these curves should be compared, that is, the curve that would have been produced if $\gamma_s(t)$ coincided with $\gamma_{\text{Load Cell}}$. Long loading pulses[20] and large strains are necessary to reproduce the linear stress-strain curve in the most accurate test (green line).

4. Quasistatic torsion of isotropic nonlinear elastic specimens[21]

In this section, we examine the stress state in isotropic nonlinear elastic materials undergoing various types of quasistatic torsional deformation. The general constitutive relation for incompressible isotropic elastic solids is discussed in Section 4A. The strain state in pure torsion is considered in Section 4B. The stress state for pure torsion of a general incompressible isotropic elastic solid is derived in Section 4C, and the stress state for the special case of a Mooney–Rivlin material is considered in Section 4D. The specimens in Sections 4B–4D may be either annular or disc-shaped. For incompressible annular specimens, radially nonuniform torsional deformations are briefly discussed in Section 4E; such deformations are necessary in order to satisfy the stress-free boundary condition on both the outer and inner surfaces.

In Section 4F, we present the results of our three-dimensional quasistatic torsion simulations for short, nearly incompressible, annular specimens with glued ends and stress-free inner and outer surfaces. The constitutive model used in these simulations is a compressible version of the Mooney–Rivlin model. The boundary conditions in these simulations, which mimic those in the tests by Nie et al. [2013], do not allow the annular specimens to undergo pure torsion or the radially nonuniform torsion considered in Section 4E. The stress components obtained in the simulations are compared with the analytical results for pure torsion from Sections 4C and 4D.

4A. *Incompressible isotropic nonlinear elastic solids.* The Cauchy stress tensor $\boldsymbol{T}$ can be decomposed into a pressure (or hydrostatic stress) p and a deviatoric stress tensor $\boldsymbol{S}$ (i.e., tr $\boldsymbol{S} = 0$):

$$\boldsymbol{T} = -p\boldsymbol{I} + \boldsymbol{S}, \qquad p \equiv -\tfrac{1}{3}\,\text{tr}\,\boldsymbol{T}, \qquad \boldsymbol{S} = \text{dev}\,\boldsymbol{T} \equiv \boldsymbol{T} - \tfrac{1}{3}(\text{tr}\,\boldsymbol{T})\boldsymbol{I}. \tag{4-1}$$

Here $\boldsymbol{I}$ denotes the identity tensor. The standard sign convention for the Cauchy stress tensor is used in this paper: normal stress components are taken positive in tension. However, the pressure p is positive in compression. It is sometimes simpler to decompose $\boldsymbol{T}$ as

$$\boldsymbol{T} = -\hat{p}\boldsymbol{I} + \hat{\boldsymbol{S}}, \tag{4-2}$$

where the tensor $\hat{\boldsymbol{S}}$ need not be deviatoric, in which case the scalar $\hat{p}$ need not equal the pressure p.[22] Consistency with the relations (4-1) requires that

$$p = \hat{p} - \tfrac{1}{3}\,\text{tr}\,\hat{\boldsymbol{S}}, \qquad \boldsymbol{S} = \text{dev}\,\hat{\boldsymbol{S}}. \tag{4-3}$$

---

[20]In this case, the notion of "constant strain-rate" should be modified to "peak strain-rate" since the plateau time is small compared to the rise time.

[21]General background for some of the material in Sections 4A–4E can be found in the books [Green and Adkins 1960; Truesdell and Noll 1965; Treloar 1975; Batra 2006] and the papers [Rivlin 1948b; 1949; Beatty 1987].

[22] Nevertheless, some authors still refer to $\hat{p}$ as "the pressure" in this case.

For a compressible (i.e., unconstrained) material, a constitutive relation must be provided for $\boldsymbol{T}$ and, equivalently, for p and $\boldsymbol{S}$ or for $\hat{p}$ and $\hat{\boldsymbol{S}}$.

For an incompressible material, p and $\hat{p}$ are indeterminate in the sense that they are not subject to any constitutive relation. However, their values at each point in the material must be such that the boundary conditions and momentum balance equations (or, in the quasistatic case, the equilibrium equations) are satisfied. For an incompressible material, a constitutive relation need only be provided for $\boldsymbol{S}$ or $\hat{\boldsymbol{S}}$, which are referred to as the determinate parts of the stress.

For an incompressible elastic material, the determinate stress $\hat{\boldsymbol{S}}$ is, by definition, a function of the deformation gradient $\boldsymbol{F}$. If the material is also isotropic, then $\hat{\boldsymbol{S}}$ is an isotropic function of the left Cauchy–Green deformation tensor $\boldsymbol{B} = \boldsymbol{F}\boldsymbol{F}^T$. A general representation for such functions is given by

$$\hat{\boldsymbol{S}} = \mu\big[\omega\boldsymbol{B} - (1-\omega)\boldsymbol{B}^{-1}\big] = 2C_1\boldsymbol{B} - 2C_2\boldsymbol{B}^{-1}, \tag{4-4}$$

where

$$C_1 = \tfrac{1}{2}\mu\omega, \qquad C_2 = \tfrac{1}{2}\mu(1-\omega), \qquad \mu = 2(C_1+C_2), \qquad \omega = \frac{C_1}{C_1+C_2}. \tag{4-5}$$

The elastic moduli C_1, C_2, and μ and the dimensionless parameter ω are scalar-valued functions of $\operatorname{tr}\boldsymbol{B}$ and $\operatorname{tr}\boldsymbol{B}^{-1}$. In particular, $\mu = \tilde{\mu}(\operatorname{tr}\boldsymbol{B}, \operatorname{tr}\boldsymbol{B}^{-1})$ can be interpreted as a (generally strain-dependent) shear modulus.[23] For infinitesimal deformations, the deviatoric part of the constitutive relation (4-4) reduces to the linear elastic constitutive relation for the deviatoric stress tensor: $\boldsymbol{S} = 2\mu_0\operatorname{dev}\boldsymbol{\epsilon}$, where $\boldsymbol{\epsilon}$ is the infinitesimal strain tensor and $\mu_0 = \tilde{\mu}(3,3)$ since $\operatorname{tr}\boldsymbol{B} = \operatorname{tr}\boldsymbol{B}^{-1} = \operatorname{tr}\boldsymbol{I} = 3$ in the undeformed state. Thus, μ_0 is the linear elastic shear modulus that was denoted by μ in previous sections.

Specification of either set of constitutive functions μ, ω or C_1, C_2 determines a particular material within the general class of incompressible isotropic elastic materials. At this point, we do not assume that the material is hyperelastic since this condition is not necessary for any of the results on the stress state in pure torsion in Section 4C.[24] However, the incompressible Mooney–Rivlin model considered in Section 4D and the compressible version of this model used in the three-dimensional simulations (Sections 4F and 5A) are hyperelastic.

It has been found that the inequalities $C_1 > 0$ and $C_2 \geq 0$ imply physically reasonable response and are consistent with experimental data on many nearly incompressible isotropic elastic solids.[25] These inequalities, which are equivalent to

$$\mu > 0, \qquad 0 < \omega \leq 1, \tag{4-6}$$

are assumed throughout this paper. Then $0 \leq 1 - \omega < 1$ also.

---

[23] See also (4-16) below for the case of pure torsional deformations.

[24] If the material is hyperelastic, then the stress tensor is derivable from a strain energy (per unit volume) W with $W = \widetilde{W}(\operatorname{tr}\boldsymbol{B}, \operatorname{tr}\boldsymbol{B}^{-1})$ for an incompressible isotropic elastic material. Consequently, the coefficient functions μ, ω and C_1, C_2 in (4-4) are determined by W; e.g., $C_1 = \partial W/\partial(\operatorname{tr}\boldsymbol{B})$ and $C_2 = \partial W/\partial(\operatorname{tr}\boldsymbol{B}^{-1})$. It follows that C_1 and C_2 are not independent although neither function completely determines the other. Similar comments apply to μ and ω although their expressions in terms of the derivatives of W are more complicated.

[25] See [Truesdell and Noll 1965, §49, §53] and [Beatty 1987], where these are referred to as the E-inequalities.

4B. *Pure torsional deformation.* A *pure torsional deformation* satisfying the boundary conditions (2-2) is given by (3-1) with the angular displacement δ as in (3-13):

$$r = R, \qquad \theta = \hat{\theta}(\Theta, Z) = \Theta + \psi(Z - L), \qquad z = Z. \tag{4-7}$$

We assume that the angle of twist per unit length, ψ, is positive: $\psi > 0$. For this deformation, the physical components[26] of the deformation gradient F, the left Cauchy–Green tensor $B \equiv F F^T$, and its inverse B^{-1} are given by

$$[F] = \begin{bmatrix} 1 & 0 & 0 \\ 0 & 1 & \psi r \\ 0 & 0 & 1 \end{bmatrix}, \qquad [B] = \begin{bmatrix} 1 & 0 & 0 \\ 0 & 1 + \psi^2 r^2 & \psi r \\ 0 & \psi r & 1 \end{bmatrix}, \qquad [B^{-1}] = \begin{bmatrix} 1 & 0 & 0 \\ 0 & 1 & -\psi r \\ 0 & -\psi r & 1 + \psi^2 r^2 \end{bmatrix}. \tag{4-8}$$

Thus, pure torsion is radially inhomogeneous and isochoric ($\det F = 1$). The Eulerian finite strain tensors corresponding to B and B^{-1} are $E = \frac{1}{2}(B - I)$ and $\mathcal{E} = \frac{1}{2}(I - B^{-1})$; the latter is known as the Almansi strain tensor. For pure torsion, the only nonzero components of E and $\mathcal{E}$ are $E_{\theta\theta} = \psi^2 r^2$, $\mathcal{E}_{zz} = -\psi^2 r^2$, and

$$E_{\theta z} = E_{z\theta} = \mathcal{E}_{\theta z} = \mathcal{E}_{z\theta} = \frac{1}{2}\psi r, \tag{4-9}$$

which is a measure of the shear strain in pure torsion.[27]

The volume average of the shear strain $E_{\theta z}$ is given by

$$\langle E_{\theta z}\rangle \equiv \frac{1}{V} \iiint E_{\theta z}\, dV = \frac{1}{3}\psi \frac{R_o^2 + R_i R_o + R_i^2}{R_i + R_o}. \tag{4-10}$$

Since $E_{\theta z}$ is independent of z, this is also the average over the annular cross-section at any given axial location. $\langle E_{\theta z}\rangle$ can also be expressed in terms of the average radius $\bar{R}$ and the radial difference Δ (see (2-1)):

$$\langle E_{\theta z}\rangle = \frac{1}{3}\psi \frac{(3\bar{R}^2 + \Delta^2)}{2\bar{R}} = \frac{1}{2}\psi \bar{R}\left[1 + \frac{1}{3}\left(\frac{\Delta}{\bar{R}}\right)^2\right] \approx \frac{1}{2}\psi \bar{R}, \tag{4-11}$$

where the approximation is valid when $\Delta/\bar{R} \ll 1$. The relative error in approximating $E_{\theta z}$ by $\frac{1}{2}\psi \bar{R}$ takes on all values between the following bounds:

$$\frac{-\Delta/\bar{R}}{1 - \Delta/\bar{R}} \leq \frac{E_{\theta z} - \frac{1}{2}\psi \bar{R}}{E_{\theta z}} \leq \frac{\Delta/\bar{R}}{1 + \Delta/\bar{R}}. \tag{4-12}$$

The relative error of largest absolute value occurs at the inner surface and is given by the absolute value of the expression on the left. For the specimen dimensions considered here (see Table 1), the largest relative error in approximating $E_{\theta z}$ by its average is 15%.

As discussed in Section 2B, for torsion tests, a measure of average shear strain often used in the experimental literature is γ_s as defined in (2-5), that is, $\gamma_s = \psi \bar{R}$. By (4-11), it follows that

$$\gamma_s \approx 2\langle E_{\theta z}\rangle \tag{4-13}$$

---

[26] Recall that these are the components relative to the unit basis vectors along the cylindrical coordinate directions.

[27] In general, both E and $\mathcal{E}$ reduce to the infinitesimal strain tensor ϵ in the limit of small displacement gradients. This fact, together with (4-9), yields $\epsilon_{\theta z} = \frac{1}{2}\psi r$ for infinitesimal deformations, consistent with (3-14).

with the relative error in this approximation being given by

$$\frac{2\langle E_{\theta z}\rangle - \gamma_s}{\gamma_s} = \tfrac{1}{3}\left(\frac{\Delta}{\bar{R}}\right)^2. \tag{4-14}$$

For the specimen dimensions in Table 1, this is about 0.0056, that is, a relative error of about 0.56%.

Finally, note that, while annular specimens have been assumed in part of the discussion above, most of the results in this section are also valid for disc-shaped specimens ($R_i = 0$). The approximation on the right side of (4-11) is no longer valid in this case since $\Delta/\bar{R} = 1$. Also, the lower bound in (4-12) becomes $-\infty$ since $\Delta/\bar{R} \to 1$ from below as $R_i \to 0$. This latter result also follows from the fact that $E_{\theta z} = 0$ at $r = 0$ whereas $\tfrac{1}{2}\psi \bar{R} > 0$.

4C. *Stress state in pure torsion of incompressible isotropic elastic specimens.* In this and the next section, we discuss the stress state in pure torsion of an incompressible, isotropic, nonlinear elastic solid. The results in these sections are valid for both annular and disc-shaped specimens. In this section, we consider the general constitutive relation $(4\text{-}4)_1$ for the determinate stress $\hat{S}$ subject only to the inequalities (4-6) for the coefficient functions μ and ω. In the next section, we consider the special case where these functions are taken to be constants. Recall that μ and ω are generally scalar-valued functions of $\mathrm{tr}\,\boldsymbol{B}$ and $\mathrm{tr}\,\boldsymbol{B}^{-1}$. Since $\mathrm{tr}\,\boldsymbol{B} = \mathrm{tr}\,\boldsymbol{B}^{-1} = 3 + \psi^2 r^2$ for pure torsion, we have

$$\mu = \tilde{\mu}(\mathrm{tr}\,\boldsymbol{B}, \mathrm{tr}\,\boldsymbol{B}^{-1}) = \tilde{\mu}(3 + \psi^2 r^2, 3 + \psi^2 r^2) \equiv \hat{\mu}(\psi^2 r^2) \tag{4-15}$$

in this case and similarly for ω, C_1, and C_2.

For pure torsion, the shear stress components are given by [Rivlin 1947; 1948b; 1949]

$$T_{\theta z} = \mu \psi r = 2\mu E_{\theta z}, \qquad T_{rz} = T_{r\theta} = 0, \tag{4-16}$$

and the differences in the normal stress components are given by

$$T_{\theta\theta} - T_{zz} = \mu \psi^2 r^2, \qquad T_{\theta\theta} - T_{rr} = \mu\omega\psi^2 r^2, \qquad T_{rr} - T_{zz} = \mu(1-\omega)\psi^2 r^2. \tag{4-17}$$

These relations follow from (4-2), $(4\text{-}4)_1$, and (4-8). It is clear that the stress state is radially inhomogeneous. We refer to the shear stress component $T_{\theta z}$ as the *torsional stress*. From (4-16), we see that μ can be interpreted as a shear modulus and that $T_{\theta z} > 0$ (since we assume $\psi > 0$) with the exception that $T_{\theta z} = 0$ at $r = 0$ for a disc-shaped specimen.

From the relations in (4-16) and (4-17), we see that the normal stress differences are proportional to the torsional stress:

$$T_{\theta\theta} - T_{zz} = \psi r \cdot T_{\theta z}, \qquad T_{\theta\theta} - T_{rr} = \omega\psi r \cdot T_{\theta z}, \qquad T_{rr} - T_{zz} = (1-\omega)\psi r \cdot T_{\theta z}. \tag{4-18}$$

The relation on the left in (4-18) is a *universal relation* between the hoop, axial, and torsional stress: it does not explicitly involve the constitutive functions μ or ω in the representation $(4\text{-}4)_1$ for the determinate stress.

To determine the normal stress components (as opposed to just their differences), we need to utilize the equilibrium equations and boundary conditions. Since $T_{r\theta}$ and T_{rz} are zero throughout the specimen, the radial component of the equilibrium equation reduces to

$$\frac{\partial T_{rr}}{\partial r} + \frac{T_{rr} - T_{\theta\theta}}{r} = 0, \tag{4-19}$$

and the assumption that the outer lateral surface ($r = R_o$) is stress-free reduces to the requirement that $T_{rr} = 0$ at $r = R_o$. On using (4-17)$_2$ to evaluate the $T_{rr} - T_{\theta\theta}$ term above, integrating from r to R_o, and then using $T_{rr}|_{r=R_o} = 0$, we obtain the following relation for the radial stress:

$$T_{rr} = -\psi^2 \int_r^{R_o} \mu\omega r \, \mathrm{d}r = -2\psi^2 \int_r^{R_o} C_1 r \, \mathrm{d}r. \qquad (4\text{-}20)$$

Then from (4-17), we see that the hoop and axial stresses are given by

$$T_{\theta\theta} = T_{rr} + \mu\omega\psi^2 r^2, \qquad T_{zz} = T_{rr} - \mu(1-\omega)\psi^2 r^2 \qquad (4\text{-}21)$$

with T_{rr} as in (4-20). Since μ and ω are functions of $\psi^2 r^2$, it follows that T_{rr}, $T_{\theta\theta}$, T_{zz}, and $T_{\theta z}$ depend only on ψ and r while $T_{r\theta} = T_{rz} = 0$. These results imply that all terms in the θ and z components of the equilibrium equation are identically zero. Thus, pure torsion is possible in any incompressible, isotropic, nonlinear elastic specimen (disc-shaped or annular), and the outer surface $R = R_o$ may be taken to be stress-free [Rivlin 1947; 1948b; 1949].[28]

Since μ, ω and C_1 are functions of $\psi^2 r^2$, the integral for T_{rr} cannot be evaluated unless C_1 (equivalently, the product $\mu\omega$) is specified. However, since μ and ω are positive and $\omega \leq 1$ and $\psi \neq 0$,[29] important qualitative properties of the normal stress components may be inferred directly from (4-20) and (4-21), as summarized below.[30]

For pure torsion of an incompressible, isotropic, nonlinear elastic specimen (disc-shaped or annular) with stress-free outer surface $r = R_o$, we have:

Conclusion 1. T_{rr} is negative for $R_i \leq r < R_o$. Thus, the radial stress is compressive except at the outer surface, where it is zero. Furthermore, the magnitude of the radial stress increases with increasing radial distance from the outer surface.

Conclusion 2. Since $T_{rr} < 0$ at $r = R_i$, for annular specimens (where $R_i > 0$), we see that a (nonzero) compressive normal stress must be applied on the inner surface in order that radial equilibrium be satisfied. If this compressive stress is not applied, then the specimen cannot undergo a pure torsional deformation.

Conclusion 3. Since $T_{rr} < 0$ for $R_i \leq r < R_o$, it follows that $T_{zz} < 0$ for $R_i \leq r < R_o$ and $T_{zz} \leq 0$ at $r = R_o$ with equality holding only if $\omega = 1$ at $r = R_o$. Thus, the axial stress is compressive everywhere except possibly at the outer surface $r = R_o$, where it is either compressive or zero.

Conclusion 4. Since $T_{rr} = 0$ at $r = R_o$, it follows that $T_{\theta\theta}|_{r=R_o} = \mu\omega\psi^2 r^2 > 0$. Thus, the hoop stress $T_{\theta\theta}$ is positive (i.e., tensile) at the outer surface, and by continuity, $T_{\theta\theta}$ must be tensile for some radial distance into the interior of the specimen.

Conclusion 5. The radial, hoop, and axial stresses depend on both constitutive functions $\mu = \hat{\mu}(\psi^2 r^2)$ and $\omega = \hat{\omega}(\psi^2 r^2)$ while the torsional stress is independent of ω. It follows that *no information on the dimensionless constitutive function ω can be inferred from measurements of the torsional stress $T_{\theta z}$ alone.*[31]

---

[28] Rivlin assumed that the material is hyperelastic although that assumption is not necessary for this conclusion [Truesdell and Noll 1965, §57].

[29] Actually, we have assumed that ψ is positive, but the sign of ψ does not affect Conclusions 1–5.

[30] Many (but not all) of these conclusions can be found in the references cited previously.

[31] This conclusion holds even if we assume (as is reasonable) that the material is hyperelastic although we omit the proof of this result.

4D. *Pure torsion of Mooney–Rivlin materials.* The classical Mooney–Rivlin model[32] is a special case of the general constitutive relation for an incompressible isotropic elastic solid. It is obtained by taking the coefficient functions C_1 and C_2 (equivalently, μ and ω) in the expression (4-4) for the determinate stress $\hat{S}$ to be constants.[33] The special case $C_2 = 0$ (i.e., $\omega = 1$) is known as a neo-Hookean material. For infinitesimal deformations, the deviatoric part of the Mooney–Rivlin constitutive relation reduces to $S = 2\mu \operatorname{dev} \epsilon$, where ϵ is the infinitesimal strain tensor. Thus, the constant μ in the Mooney–Rivlin model agrees with the shear modulus in the linear elastic theory [Mooney 1940; Rivlin 1947].

The Mooney–Rivlin model is one of the simplest isotropic nonlinear elastic constitutive models, and yet it still exhibits features that are in qualitative agreement with experimental data on many soft, nearly incompressible materials under moderate deformations. For this model, there are explicit closed-form expressions for all stress components in pure torsion (see below). Furthermore, a compressible version of the Mooney–Rivlin model was available in the code that we intended to use for our three-dimensional torsion simulations. For these reasons, all of our quasistatic torsion simulations (Section 4F) and most of the three-dimensional dynamic simulations (Section 5A) used this compressible version of the Mooney–Rivlin model. The following analytical results for pure torsion of an incompressible Mooney–Rivlin material will be compared with the three-dimensional quasistatic torsion simulations in Section 4F.

For Mooney–Rivlin specimens, the relation (4-16) for $T_{\theta z}$ and the relations (4-17) and (4-18) for the normal stress differences do not simplify further (aside from the fact that μ and ω are now constants). However, the relations (4-20) and (4-21) for the normal stress components reduce to[34]

$$-T_{rr} = \tfrac{1}{2}\mu\psi^2 \cdot \omega(R_o^2 - r^2) = C_1\psi^2(R_o^2 - r^2), \tag{4-22a}$$

$$T_{\theta\theta} = \tfrac{1}{2}\mu\psi^2 \cdot \omega(3r^2 - R_o^2) = C_1\psi^2(3r^2 - R_o^2), \tag{4-22b}$$

$$-T_{zz} = \tfrac{1}{2}\mu\psi^2 \cdot \left[\omega R_o^2 + (2 - 3\omega)r^2\right] = \psi^2\left[(C_1 - 2C_2)(R_o^2 - r^2) + 2C_2 R_o^2\right]. \tag{4-22c}$$

Of course, all of the conclusions at the end of Section 4C apply to the special case of Mooney–Rivlin specimens. The (compressive) radial stress that must be applied to the inner surface $r = R_i$ of an annular specimen in order to maintain a pure torsional deformation is now given explicitly by

$$T_{rr}|_{r=R_i} = -\tfrac{1}{2}\mu\psi^2 \cdot \omega(R_o^2 - R_i^2) = -\psi^2 C_1(R_o^2 - R_i^2) < 0. \tag{4-23}$$

From (4-22b), it follows that $T_{\theta\theta} > 0$ (i.e., the hoop stress is tensile) for all $R_i \le r \le R_o$ if and only if $R_i > R_o/\sqrt{3}$. This condition on the inner and outer radii is satisfied for the specimens in our quasistatic and dynamic simulations (see Table 1). The relations (4-22), together with $p = -\tfrac{1}{3}(T_{rr} + T_{\theta\theta} + T_{zz})$, imply that the pressure is given by

$$p = \tfrac{1}{2}\mu\psi^2 \cdot \left[\omega R_o^2 + \tfrac{1}{3}(2 - 7\omega)r^2\right]. \tag{4-24}$$

Since μ is constant, from the relation (4-16) for $T_{\theta z}$, together with the expression (4-11) for $\langle E_{\theta z}\rangle$ and

---

[32] In some of the literature, this is referred to as the Mooney model [Mooney 1940; Rivlin 1947; 1948a; 1948b; 1949; Rivlin and Saunders 1951; Green and Adkins 1960; Truesdell and Noll 1965, §95; Treloar 1975; Beatty 1987; Batra 2006].

[33] Equivalently, this is the hyperelastic material with strain energy function $W = C_1(\operatorname{tr} B - 3) + C_2(\operatorname{tr} B^{-1} - 3)$.

[34] The relations (4-22c)$_2$ and (4-23)$_2$ are some of the earliest results of [Rivlin 1947; 1948a].

the fact that $\gamma_s = \psi \bar{R}$ (see (2-5)), we see that the volume-averaged torsional stress is given by

$$\langle T_{\theta z} \rangle = 2\mu \langle E_{\theta z} \rangle = \mu \psi \bar{R} \left[1 + \tfrac{1}{3} \left(\frac{\Delta}{\bar{R}} \right)^2 \right] = \mu \gamma_s \left[1 + \tfrac{1}{3} \left(\frac{\Delta}{\bar{R}} \right)^2 \right]. \qquad (4\text{-}25)$$

For the specimen dimensions in Table 1, the term in square brackets differs from unity by only 0.0056. Thus, the relative error in approximating $\langle T_{\theta z} \rangle$ by $\mu \gamma_s$ is 0.56%, a result which also follows directly from (4-14).

4E. *Radially nonuniform torsional deformations of annular specimens.* Conclusion 2 in Section 4C implies that for incompressible annular specimens a class of torsional deformations more general than *pure* torsion must be considered if both the outer and inner lateral surfaces ($r = R_o$ and $r = R_i$) are stress-free. Recall that the pure torsional deformation (4-7) does not involve any radial displacement. Here we briefly consider more general torsional deformations for which the annular specimen may deform radially:

$$r = \hat{r}(R), \qquad \theta = \Theta + \psi(Z - L), \qquad z = Z. \qquad (4\text{-}26a)$$

Incompressibility requires that $1 = \det \boldsymbol{F} = (\partial r / \partial R)(r/R) = \partial(r^2)/\partial(R^2)$; consequently,

$$r = \sqrt{R^2 + \beta}, \qquad (4\text{-}26b)$$

where β is an arbitrary constant subject only to the condition that $R_i^2 + \beta > 0$. Note that the deformation (4-26) reduces to pure torsion ($r = R$) if and only if $\beta = 0$.

Proceeding as in the case of pure torsion, it can be shown that the deformation (4-26) is possible in any incompressible, isotropic elastic, annular specimen; that $T_{rz} = T_{r\theta} = 0$; and that the outer surface $R = R_o$ may be taken to be stress-free. This was first shown by Rivlin [1949].[35] The radial stress is expressed in terms of the undeformed radial coordinate by

$$T_{rr}(R) = -\int_R^{R_o} \mu \left[\psi^2 \omega R + \frac{1}{R} - \frac{R^3}{(R^2 + \beta)^2} \right] dR \qquad (4\text{-}27)$$

with the constitutive functions μ and ω generally dependent on ψ^2, R^2, and β. On letting $R = R_i$ in this relation and then setting the result to zero, we obtain an implicit relation for β that must be satisfied in order that the inner surface $R = R_i$ is stress-free. Clearly, this value of β depends on ψ, R_i, and R_o as well as the constitutive functions μ and ω. The dependence on μ drops out if μ is a constant as in the Mooney–Rivlin model. For that case, the integral can be evaluated and a simpler implicit relation for β is obtained [Rivlin 1949, §8].[36]

4F. *Three-dimensional quasistatic torsion simulations.* Although the torsional deformation (4-26) is of some theoretical interest, in practice, it would be difficult to apply a torque on the face of a soft specimen while simultaneously admitting a radial deformation on that face. In the torsional Kolsky bar tests in [Nie et al. 2013], the faces of the specimen are glued to the bar and the load cell, and analogous

---

[35] Rivlin considered a slightly more general deformation that includes a superposed uniform axial extension. He assumed that the material is hyperelastic, but this condition is not necessary [Truesdell and Noll 1965, §57].

[36] Rivlin considered the more general case that includes a superposed uniform axial extension; see also (95.8) in [Truesdell and Noll 1965].

glued end conditions are used for their quasistatic torsion tests. Thus, for the actual torsion tests of interest here, neither the pure torsion considered in Sections 4B–4D nor the torsional deformation (4-26) can be expected to hold exactly. Nevertheless, it is clear from the discussion in Section 4E that, at axial locations between the two faces, an annular specimen will have a tendency to deform radially in order to satisfy the stress-free boundary conditions on the inner and outer surfaces. Since relatively short annular specimens are used, the constraints at either end of the specimen can be expected to severely restrict (though not completely eliminate) the radial deformation at axial locations in the interior. Thus, in quasistatic torsion tests with glued ends, we expect some axial variation in the radial deformation and consequently in the stress components as well as additional nonzero stress components such as T_{rz}. The analytical results for the torsional, axial, and hoop stresses in pure torsion may still hold approximately, but the accuracy of these approximations is not clear. Since a theoretical analysis of this problem is intractable,[37] we rely on numerical simulations for quantitative estimates of the stress state.

One face of the annular specimen was subjected to a rigid rotation while the other face was fixed so that material points on either face could not undergo axial or radial displacements. Stress-free boundary conditions were used on the outer surface $R = R_o$ and the inner surface $R = R_i$. Details of the numerical method are provided in Appendix A.

In these simulations, we used a compressible version of the Mooney–Rivlin model for the specimens.[38] The equation of state for the pressure in this model is

$$p = -\kappa \ln J \approx \kappa(1 - J), \qquad J = \det \boldsymbol{F}. \tag{4-28}$$

The constant κ is the bulk modulus. The constitutive relation for the Cauchy stress tensor $\boldsymbol{T}$ is given by (4-2) with $\hat{p}$ and $\hat{\boldsymbol{S}}$ defined as follows:

$$\hat{p} = p + \tfrac{1}{3} \operatorname{tr} \hat{\boldsymbol{S}}, \qquad J\hat{\boldsymbol{S}} = \mu\big[\omega\widetilde{\boldsymbol{B}} - (1-\omega)\widetilde{\boldsymbol{B}}^{-1}\big] = 2C_1\widetilde{\boldsymbol{B}} - 2C_2\widetilde{\boldsymbol{B}}^{-1}. \tag{4-29}$$

Here μ, ω, C_1, and C_2 are constants as in the incompressible version, and

$$\widetilde{\boldsymbol{B}} = \frac{\boldsymbol{B}}{(\det \boldsymbol{B})^{1/3}} = \frac{\boldsymbol{B}}{J^{2/3}} \tag{4-30}$$

is the distortional part of the left Cauchy–Green tensor $\boldsymbol{B}$. Note that, regardless of the value of the Jacobian J, $\det \widetilde{\boldsymbol{B}} = \det \widetilde{\boldsymbol{B}}^{-1} = 1$, analogous to the conditions $\det \boldsymbol{B} = \det \boldsymbol{B}^{-1} = 1$ for the incompressible case. This relation for $\hat{\boldsymbol{S}}$ is identical to the relation (4-4) for the incompressible Mooney–Rivlin model except that $\boldsymbol{B}$ has been replaced by its distortional part and $\hat{\boldsymbol{S}}$ is multiplied by the factor J.[39] The relation (4-29)₁ for $\hat{p}$ guarantees consistency with (4-3)₁.

We used $\kappa = 2.3\,\mathrm{GPa}$ for all simulations and varied the shear modulus by almost three orders of magnitude: $\mu = 800, 80, 8$, and $2\,\mathrm{kPa}$. The corresponding ratios of bulk to shear modulus varied from 2875 to 1.15×10^6 so that in all cases the specimen was nearly incompressible. For each of the four values

---

[37] Some idea of the difficulty of this problem can be inferred from the paper [Hill and Lee 1989], which treats a slightly different problem, namely combined compression and torsion of incompressible, disc-shaped, Mooney–Rivlin specimens with glued ends. This work has been extended to torsional waves [Hill and Wegner 2004], but the results are not directly applicable to the dynamic problem considered here since annular specimens are not considered.

[38] Additional departures (perhaps small) from pure torsion will be introduced by the slight compressibility of the specimens.

[39] This factor ensures that the material is hyperelastic. The strain energy function is given by $W = \kappa J(\ln J - 1) + C_1(\operatorname{tr}\widetilde{\boldsymbol{B}} - 3) + C_2(\operatorname{tr}\widetilde{\boldsymbol{B}}^{-1} - 3)$.

of the shear modulus, simulations were performed for three values of the nondimensional parameter ω: 0.3, 0.6, and 1. This resulted in twelve quasistatic simulations.

We have compared the stress states obtained from the numerical simulations (using the compressible version of the Mooney–Rivlin model) with the stress states that would have been obtained in pure torsion of an incompressible Mooney–Rivlin material (as determined from (4-22) and (4-24)). These comparisons are made at the same average angle of twist per unit length ψ (equivalently, at the same average shear strain γ_s) and for the same set of twelve values for μ and ω. The results are plotted in Figure 6. Each of the ten panels contains either thirteen or fifteen curves, but many (in panels a and b, all of them) are indistinguishable. This is due (in part) to the normalization of the stress components as discussed in the next paragraph. In each panel, there are twelve curves for the numerical simulations (solid lines) and either one curve (panels a and b) or three curves for the theoretical pure torsion (dashed lines).
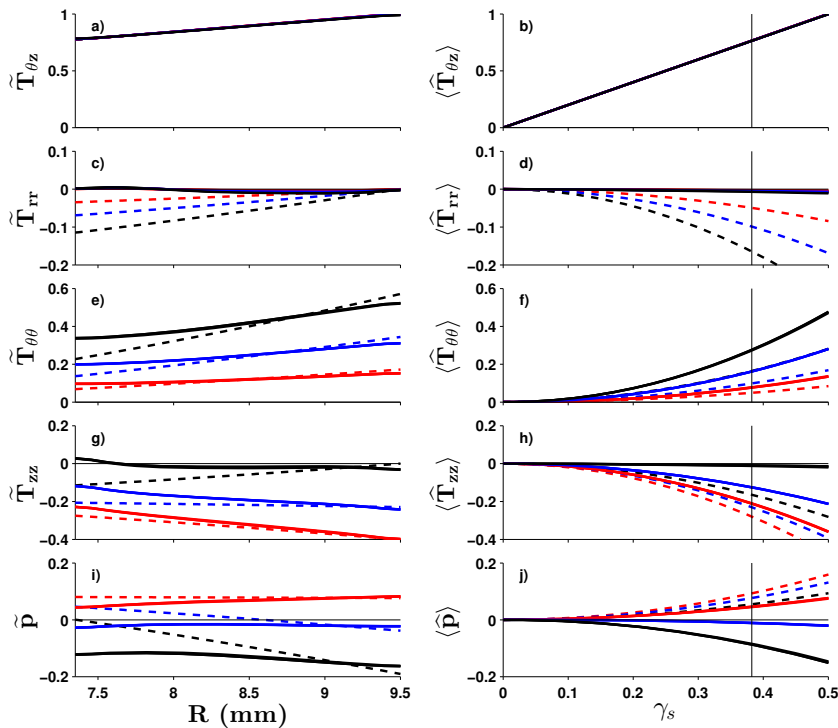
Figure 6. Normalized stress states in torsion for Mooney–Rivlin specimens. Twelve numerical simulations (solid lines) are compared with pure torsion (dashed lines). For each of four values of the shear modulus μ (800, 80, 8, and 2 kPa), curves for $\omega = 0.3$ (red), $\omega = 0.6$ (blue), and $\omega = 1.0$ (black) are shown. Curves for different shear moduli are indistinguishable (either approximately or exactly) because of the normalizations. The left panels examine the variation of the normalized stress with referential radius for an angle of twist per unit length $\psi = 0.059$ radians/mm at the axial location $Z = L/2$. The right panels are plots of normalized volume-averaged stress versus average shear strain. The vertical line in the right column indicates the average shear strain for the panels on the left.

In order to condense the information from the simulations and the theoretical results and also to more clearly display the relative magnitude of the stresses in each case, all stress components in Figure 6 have been normalized by an appropriate "maximum" torsional stress. For the left column, the tilde on the stresses indicates that they have been normalized by $\mu \psi R_o$, which by $(4\text{-}16)_1$ is the maximum torsional stress that would occur in a pure torsional deformation. For the right column, the hat on the stresses indicates that they have been normalized by the volume-averaged torsional stress $\langle T_{\theta z} \rangle$ (see (4-25)) that would occur in a pure torsional deformation, evaluated at the final average shear strain $\gamma_s = 0.5$. The angle brackets on the stresses in the right column indicate that these normalized stresses have then been volume-averaged.

In the left column of Figure 6, we examine the radial variation in the torsional stress, the normal stress components, and the pressure at an axial location in the middle of the specimen ($Z = L/2$). In these plots, the average angle of twist per unit length is $\psi = 0.059 \, \text{radians/mm} = 3.38°/\text{mm}$, and the corresponding average shear strain is $\gamma_s = 0.38$. Data from torsion tests is typically plotted as average shear stress versus average shear strain γ_s with the average shear stress inferred from the measured torque. The right column of Figure 6 displays the volume-averaged stress-strain curves. The vertical black lines in the right column indicate the average shear strain (0.38) for the panels on the left.

Consider panel a for the radial variation of the torsional stress. Since $T_{\theta z} = \mu \psi r$ for pure torsion of an incompressible Mooney–Rivlin material, the normalized torsional stress in this case is given by $\widetilde{T}_{\theta z} = \mu \psi r / \mu \psi R_o = r/R_o = R/R_o$, independent of μ or ω. Thus, for pure torsion of an incompressible Mooney–Rivlin material, there is a single normalized torsional stress versus radius curve, namely the line R/R_o. This line and the twelve normalized torsional stress versus radius curves from the numerical simulations are indistinguishable, the maximum relative difference being less than 1%.

A similar situation occurs for the average torsional stress versus average shear strain curves in panel b. Since $\langle T_{\theta z} \rangle$ is given by (4-25) for pure torsion of an incompressible Mooney–Rivlin material, the normalized average torsional stress in this case is given by $\langle \widehat{T}_{\theta z} \rangle = \gamma_s / (\gamma_s|_{0.5})$. Thus, for pure torsion of an incompressible Mooney–Rivlin material, there is a single normalized average torsional stress versus average strain curve, namely the line $\gamma_s / 0.5$. This line and the twelve normalized average torsional stress versus average shear strain curves from the numerical simulations are indistinguishable, the maximum relative difference again being less than 1%.

Thus, even though the annular specimens in our numerical simulations cannot undergo a pure torsional deformation, the torsional stress in those simulations is indistinguishable from the torsional stress in theoretical pure torsion of an incompressible Mooney–Rivlin material. On the other hand, it is clear from Figure 6 that this conclusion does not hold for the normal stress components; that is, the normal stresses and the pressure in the annular specimen simulations (solid lines) do not agree with the theoretical predictions for pure torsion of an incompressible Mooney–Rivlin material (dashed lines).

For pure torsion of an incompressible Mooney–Rivlin material, the theoretical relations (4-22) and (4-24) predict that the normal stress components and the pressure are proportional to the shear modulus μ and depend on ω as well; consequently, the normalized stress components in panels c–j in Figure 6 are independent of μ but still depend on ω. This results in three normalized stress curves (dashed lines) for the case of pure torsion in each of these panels — one curve for each of the three values of ω.

The disagreement between the normalized stresses for pure torsion and those for the numerical simulations are most pronounced for the radial component (panels c and d). In fact, the normalized radial

stresses for the simulations are so small that all twelve curves (solid lines) are indistinguishable from the horizontal axis ($\widetilde{T}_{rr} = 0$ or $\langle \widehat{T}_{rr} \rangle = 0$). Of course, the fact that the radial stress is essentially zero throughout the annular specimen is not unexpected in view of the fact that it is zero on the inner and outer lateral surfaces. This is one of the motivations for using annular specimens. The other motivation for using annular (as opposed to disc-shaped) specimens in torsion tests is that, while torsional stress $T_{\theta z}$ and the shear strain $E_{\theta z}$ are radially nonuniform, the total radial variation in these quantities is expected to be smaller for annular specimens. For the torsional stress, this is verified in Figure 6a.

Unlike the radial stresses, the hoop stress, axial stress, and pressure (panels e–j) for the simulations (solid lines) share some qualitative features with the theoretical predictions for pure torsion (dashed lines). In particular, the normalized hoop stress, axial stress, and pressure for the simulations are (approximately) independent of the shear modulus but depend strongly on the value of ω so that the twelve curves appear to collapse into three curves. Furthermore, for both the simulations and the pure torsion case, the hoop stress increases with increasing ω while the magnitude of the axial stress decreases with increasing ω. For the axial and hoop stresses, the discrepancies between the simulations and the pure torsion case increase with increasing ω.

Further consideration of (4-16) and (4-22) shows that, for pure torsion, the ratio of normal stress to torsional shear stress increases with shear strain: the shear stress depends linearly on ψ while the normal components depend quadratically on ψ and thus quadratically on the average shear strain γ_s. Comparison of the solid curves in panel b with those in panels f and h in Figure 6 shows that the same conclusion holds for the hoop and axial stresses (but not the radial stress) in the numerical simulations. Thus, for sufficiently large angles of twist or for sufficiently thin specimens, the magnitude of the normal stresses could exceed the shear stress. On the other hand, a smaller shear strain of 0.2, say, gives an average hoop stress that is only 5 to 20% of the shear stress (depending on ω) and an average axial stress that is only 1 to 15% of the shear stress.

The glued-end boundary conditions in combination with the stress-free boundary conditions on the inner and outer surfaces of the annular specimen resulted in axial variations in the stress components in the torsion simulations although these results are not plotted here. For the normal stresses, these axial variations were concentrated within approximately 0.25 mm of either face of the specimen and essentially vanished away from the specimen faces. Both hoop and axial stresses varied by as much as 30% near the faces whereas the variation in this region for the torsional stress $T_{\theta z}$ was typically less than 5%. The other shear components, T_{rz} and $T_{r\theta}$, were also nonzero. They were smaller in magnitude (typically less than 10% of the torsional stress) and varied throughout the length of the specimen.

Although the magnitude of T_{rz} is small, the fact that T_{rz} cannot be identically zero can be established as follows. Using the assumption that the specimen is in equilibrium (so that div $\boldsymbol{T} = \boldsymbol{0}$) together with the stress-free boundary conditions on the inner and outer surfaces of the annular specimen, one could show

$$\int_{\mathcal{A}(z)} \frac{1}{r} T_{\theta\theta} \, dA = \frac{\partial}{\partial z} \int_{\mathcal{A}(z)} T_{rz} \, dA, \qquad (4\text{-}31)$$

where $\mathcal{A}(z)$ is the annular cross-section at the axial location z.[40] As observed above (see panel e in

---

[40] We omit the proof of this relation. It is a fairly general result in the sense that no material symmetry conditions are required, the specimen need not be homogeneous, and neither the initial nor deformed annular cross-sections need be axially uniform or have circular boundaries.

Figure 6), $T_{\theta\theta}$ is positive at each radial location. Hence, the integral on the left above is positive and must be balanced by an axial gradient in the integral of T_{rz} over the cross-section $\mathcal{A}(z)$.

5. Three-dimensional dynamic simulations

In this section, we further supplement our one-dimensional dynamic simulations and three-dimensional quasistatic analysis and simulations with three-dimensional dynamic simulations. Our dynamic torsion simulations use the same glued-end boundary conditions and stress-free boundary conditions on the outer and inner surfaces as in the quasistatic simulations discussed in Section 4F. With the exception of the viscoelastic results discussed in Section 5B, we used the same constitutive model and the same model parameters as in the three-dimensional quasistatic simulations except that the $\mu = 2\,\text{kPa}$ case is not considered. Thus, we used $\kappa = 2.3\,\text{GPa}$ and varied the shear modulus by two orders of magnitude: $\mu = 800$, 80, and 8 kPa. The corresponding ratios of bulk to shear modulus varied from 2875 to 2.875×10^5 so that in all cases the specimen was nearly incompressible. For each of the three values of the shear modulus, simulations were performed for three values of the nondimensional parameter ω: 0.3, 0.6, and 1. The nine simulations used the same 700/s loading pulse as the one-dimensional *Simulations I–III*; see Table 2 and panels *a* and *b* in Figure 3. Details of the numerical method are provided in Appendix A.

5A. *Nonlinear elastic model for the specimen.* We calculated the radially averaged stress at the *Load Cell* for each of the six components T_{ij} of the stress tensor, i.e.,

$$\frac{1}{\pi(R_o^2 - R_i^2)} \int_{R_i}^{R_o} T_{ij}(R, L) 2\pi R\, \mathrm{d}R.$$

These time histories are plotted for the nine simulations in Figure 7. The shear modulus μ changes with the row, and ω changes with the column so that the nine panels span vastly different elastic responses.

In the quasistatic torsion simulations (see Figure 6), the torsional shear stress $T_{\theta z}$ is insensitive to the dimensionless parameter ω in the Mooney–Rivlin model. This is also observed in the dynamic case: comparing the shear stress $T_{\theta z}$ (green traces) for fixed shear modulus, i.e., panels *a–c*, *d–f*, and *g–i* in Figure 7, we see little to no variation with ω. Similarly, in both the quasistatic and dynamic simulations, the magnitude of the axial stress T_{zz} (black traces) decreases with increasing ω whereas the hoop stress $T_{\theta\theta}$ (blue traces) increases with increasing ω with the exception of the hoop stress for the $\mu = 8\,\text{kPa}$ dynamic case. Since neither T_{zz} or $T_{\theta\theta}$ is measured in a Kolsky bar test, there would be no way to infer a value for ω from the test data, namely the measured shear stress, even if it were known that the specimen behavior was governed by the Mooney–Rivlin model.

Unlike the quasistatic simulations, for a given value of ω, the relative magnitude of the normal and torsional shear stress components vary considerably with the shear modulus in the dynamic simulations. In particular, the radial stress (red traces) is not negligible for the $\mu = 80$ and 8 kPa dynamic simulations. Also note that, for the $\mu = 8\,\text{kPa}$ case with $\omega = 0.3$ or 0.6 (panels *g* and *h*), all three normal stress components begin to change well before the torsional stress increases. This effect cannot be due to bending waves or longitudinal waves that might be generated in the incident bar as a result of the initial impact since such effects are not included in the simulations. Rather, it is caused by a longitudinal precursor wave in the specimen as discussed in the next paragraph. From Section 3, it is clear that
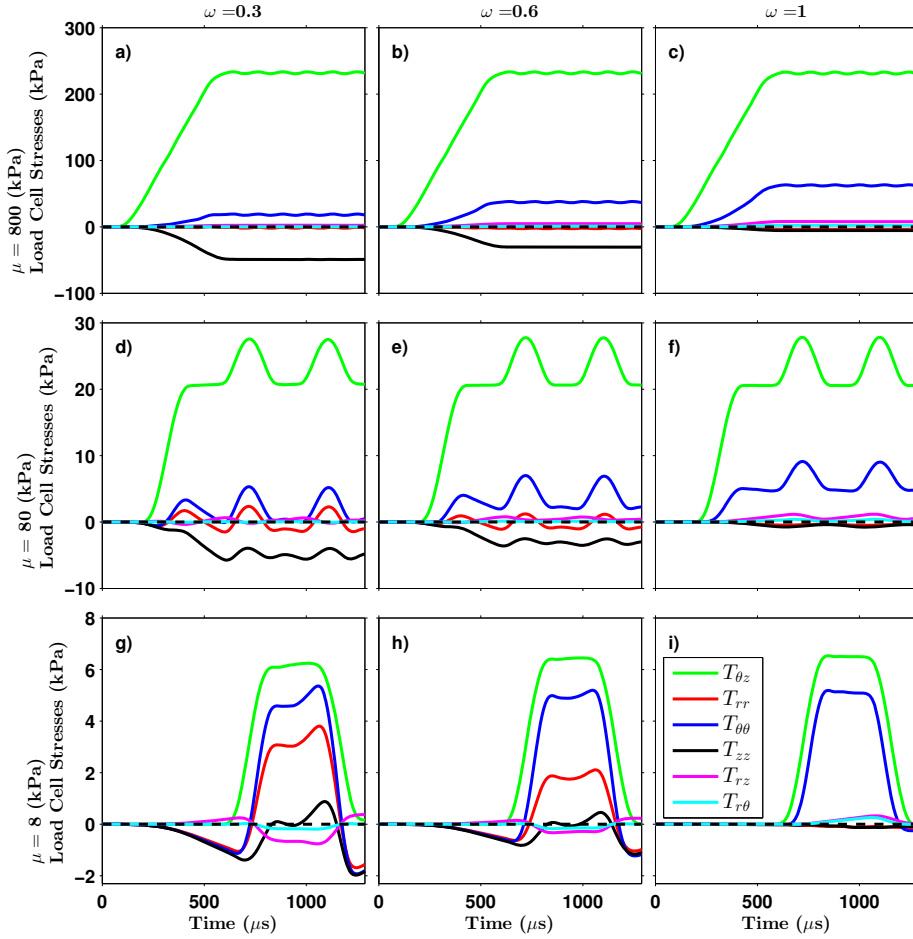
Figure 7. The radially averaged stress components at the *Load Cell* ($Z = L$) versus time for the nine simulations: two decades of shear modulus ($\mu = 800$, 80, and 8 kPa) and three values of dimensionless parameter ($\omega = 0.3$, 0.6, and 1.0). All simulations used the same 700/s loading pulse as the one-dimensional *Simulations I–III*; see Table 2 and panels *a* and *b* in Figure 3. The legend for the line colors is given in panel *i* and is consistent throughout the figure. Note the change in vertical scales for the different rows.

dynamic equilibrium is not reached when $\mu \leq 80$ kPa, and the three-dimensional simulations inform us that the stress state is no longer simple as well.

The normal stresses produced by the shearing deformation propagate at the longitudinal elastic wave speed,[41] which far exceeds the shear wave speed for all cases in Figure 7. Indeed, the longitudinal wave speed is about 1.52 mm/μs for all nine cases.[42] Hence, this wave arrives at the *Load Cell* in about 1.1 μs,

---

[41]This is a well-known nonlinear elastic effect [Davison 1966; Abou-Sayed and Clifton 1976; Scheidler 1998].

[42] For a nonlinear elastic solid, a longitudinal wave propagating into undeformed material travels at the linear elastic wave speed $c_L = \sqrt{\frac{4}{3}c_S^2 + c_B^2}$, where c_S is the shear wave speed and c_B is the bulk wave speed, i.e., $\sqrt{\kappa/\rho}$. For the bulk and shear moduli considered here ($\kappa = 2.3$ GPa and $\mu \leq 800$ kPa), the shear wave speed is negligible and $c_L \approx c_B = 1.52$ mm/μs.

which is essentially instantaneous on the time scale of Figure 7. But even though the normal stresses begin to change at the *Load Cell* at this early time, their magnitude is initially quite small — on the order of the square of the shear strain produced by the slower torsional wave. Consequently, these initial changes cannot be observed on the scale of the plots until much later times. And it is only in panels *g* and *h* that the magnitude of the normal stresses (relative to the torsional stress) is significant enough to be observed prior to the arrival of the torsional wave.

5B. *Nonlinear viscoelastic model for the specimen.* Although the goal of the torsional Kolsky bar test considered here is to quantify the strain-rate sensitivity of viscoelastic soft tissues, only elastic constitutive models have been considered up to this point. Elastic models (linear or nonlinear) are particularly useful for revealing inertial effects: since the stress in an elastic material is rate-independent, any differences between the quasistatic and dynamic simulations of the torsion test must necessarily be due to inertial effects. There is certainly no reason to expect that these inertial effects will disappear for materials exhibiting viscoelastic response. Nevertheless, we have also performed some three-dimensional dynamic simulations of torsional Kolsky bar tests using a nonlinear viscoelastic constitutive model[43] for the specimen.

We used an equilibrium elastic shear modulus of 2 kPa and an instantaneous elastic shear modulus of 40 kPa,[44] five times larger than the 8 kPa shear modulus that had been used as representative of brain tissue in the elastic models. This gives a viscoelastic shear wave speed about 2.2 times the shear speed for the $\mu = 8$ kPa linear and nonlinear elastic cases.[45] It should be clear from our results for these elastic cases that this wave speed is much too slow for dynamic equilibrium to be achieved. Indeed, while the stress histories in our simulations with the viscoelastic model differed both qualitatively and quantitatively from those described above for the elastic model, we found that the viscoelastic stress histories fell roughly between the $\mu = 80$ kPa and 8 kPa elastic cases in Figure 7.

6. Discussion and conclusions

We have conducted one- and three-dimensional analyses and simulations to understand the deformations and stress states that exist in nearly incompressible soft materials in a torsional Kolsky bar test. Here we highlight the main conclusions of this study and also discuss some relevant issues that were not addressed previously.

The use of (*linear or nonlinear*) *elastic constitutive models for the specimen in numerical simulations of Kolsky bar tests can reveal the presence of inertial effects in these tests.* Using viscoelastic models in

---

[43] See Appendix A for more details.

[44] This is close to our rough estimate of 42 kPa for the 700/s tests in [Nie et al. 2013]; see the discussion at the end of Section 3D. Recall that they estimated an initial shear modulus of 53.5 kPa from their average "700/s" shear stress versus shear strain curve.

[45] For a (linear or nonlinear) viscoelastic material, the speed of a shear wave propagating into an undeformed region is that of a linear elastic material with shear modulus equal to the (small strain) instantaneous elastic shear modulus of the viscoelastic material. This result also holds for any simple material with fading memory [Coleman et al. 1965]. However, the shear wave in the torsion test initially propagates into a slightly deformed region caused by the longitudinal precursor wave and then reflects from the *Load Cell* into a more complicated strain state. Nevertheless, the shear wave speed into an undeformed material should yield a rough estimate for the wave speed in this test, and for the viscoelastic model considered here, this is $\sqrt{40\,\text{kPa}/\rho} = \sqrt{5 \times 8\,\text{kPa}/\rho}$ or $\sqrt{5}$ times the shear speed for the $\mu = 8$ kPa elastic cases.

these simulations will add strain-rate effects to the stress histories but not substantially alter the inertial effects since the main issue here is the slow shear wave speed in the specimen.

In soft specimens, the travel time of the torsional wave can be on the order of the loading pulse duration, in which case there is insufficient time for ring-up to dynamic equilibrium. For the torsional Kolsky bar tests on bovine brain tissue at a strain-rate of "700/s" that were reported in [Nie et al. 2013], *the specimen could not have been in dynamic equilibrium, contrary to statements made in that paper.* Consequently, their "stress-strain curves" are not valid — the average strain used in their plots does not correspond to the strain at the load cell. In fact, throughout much of the test, the actual strain at the load cell was likely several times larger than the average strain used in their stress-strain plots.

The stress history at the load cell should never be time-shifted to synchronize it with the history of the average strain in order to produce a "stress-strain curve". If the stress-strain curves produced from unshifted data contain an initial strain interval for which the stress is zero (as in the left panels in Figure 4), then this is a clear indication that the specimen is not in dynamic equilibrium and consequently that no meaningful stress-strain curves can be inferred from the test data. Even if the "stress-strain curves" produced by time-shifting the load cell data *appear* physically reasonable, they will necessarily contain erroneous "strain-rate effects".

It is not clear how to modify the experimental design to alleviate the inertial effects that exist when testing with very soft specimens at high strain-rates. In Section 3E, we discussed the changes in the loading pulse and the specimen geometry that would be necessary to improve the quality. These alterations require longer bars, thinner specimens, and reductions of the maximum strain-rates considered. Ignoring the practical difficulties that longer bars, polymer bars, or thinner specimens pose, the lower strain-rates required would be on the order of 100–200/s (unless larger strains are considered) and are perhaps too low for the ranges needed for the modeling effort.

Other Kolsky bar tests such as double-lap shear [Saraf et al. 2007; Trexler et al. 2011] *or circular shearing* [Nie et al. 2011] *will have similar issues with dynamic equilibrium.* Similar dimensional arguments can be made for each of these tests. With proper consideration of the direction of the shear wave propagation and the relevant specimen length, the results of Section 3 would apply. Thus, inertial effects are still an issue with high shear strain-rate Kolsky bar tests on soft materials.

In view of the remarks above, *for tests on sufficiently soft specimens at sufficiently high strain-rates, experimenters should abandon the practice of presenting their data as "stress-strain curves" and simply report the measurements that are valid.* For the torsional Kolsky bar test of Nie et al. [2013], this consists of the torque history at the load cell and the history of the angle of twist at the other face of the specimen. These histories should be provided for each valid test, not averaged over multiple tests. Such data, in conjunction with numerical simulations of the tests, could be used in the process of validating a constitutive model that has already been calibrated. In this regard, *optical measurements of the angle of twist at the end of the incident bar adjacent to the specimen should be used in place of the traditional strain gage measurements on the incident bar.* Unlike the analysis of strain gage data, the analysis of optical data does not require that the specimen be in dynamic equilibrium or that the incident and reflected pulses do not overlap at the measurement location.

The above procedure could not be used to actually calibrate the parameters in a viscoelastic constitutive model unless the twist and torque histories are part of a larger data set for use with a numerical inverse method. The issue here is nonuniqueness, for which there are several sources. Even if a numerical

inverse method were used to optimize the fit to the measured stress and twist histories, it seems likely that several different calibrations might fit the limited data equally well, particularly in view of the variability that exists in biological specimens and the fact that several reasonable criteria for optimality could be used. Each calibration would likely result in a different numerical prediction of the strain history at the load cell. Since this strain history cannot be measured in the torsional Kolsky bar test, there would be no criterion for selecting one of these calibrations over the other. Also, significant radial, hoop, and axial stresses exist if the specimen is sufficiently soft and the strain-rate sufficiently high, yet these normal stress components are not measured in the torsional Kolsky bar test.[46] Furthermore, the measured torque (or the torsional shear stress $T_{\theta z}$) may be insensitive to some of the parameters that determine these normal stresses as was demonstrated for the case of a Mooney–Rivlin model. Different model calibrations might fit the twist and torque histories equally well or nearly as well and yet predict drastically different normal stresses, but there would be no way to determine which (if any) of these predictions are correct.

Appendix A: Details of numerical methods

One-dimensional dynamic. We solve the wave equation (3-8) along with boundary conditions (3-3)$_1$ and (3-12) numerically using a finite difference scheme. Initially, an explicit second-order, centered-time and centered-space method was implemented. This method produced reasonable results but had a tendency to be dispersive, creating erroneous ripples and other small oscillatory noise. The results presented here use a Crank–Nicolson method applied to the centered-space differences, thus making it a semi-implicit method; i.e., the approximations of the spatial derivatives were taken as an average of the values for the current time step and the next time step. This alteration trades the dispersive error for a slightly dissipative error. The length of the specimen ($L = 1.7$ mm) was divided up into equal intervals ($\Delta z = 0.0085$ mm) so that $u(z, t)$ was evaluated at 200 points; a time step Δt was chosen to satisfy the Courant stability criterion for the explicit method, $c \Delta t / \Delta z \leq 1$.

Three-dimensional quasistatic. Meshes were generated in Cubit (V12.1, Sandia National Laboratory). Simulations were performed using Sierra SolidMechanics (Adagio 4.24, Sandia National Laboratory). Adagio is an implicit, nonlinear preconditioned conjugate gradient solver. Reduced integration on HEX8 element meshes was performed. Due to the highly constrained nature of the problem, extreme care had to be taken to ensure the mesh was structured and symmetric to prevent mesh artifacts. Postprocessing of simulation results was carried out in ParaView (V3.14.0, Kitware) and MATLAB (The MathWorks).

The solutions obtained from the fully three-dimensional simulations were rotationally symmetric and enabled a reduction of the data. Variables were evaluated along five radial lines at a single angle and equally spaced axial locations ($\Theta = 0$ and $Z = 0, \frac{1}{4}L, \frac{1}{2}L, \frac{3}{4}L, L$). This postprocessing was performed in ParaView to enable further analysis. The area integrals used a composite Simpson's method in MATLAB. Similarly, volumetric averages were calculated from the five area integrals utilizing a five-point Simpson rule. Continuous plots over the radius of the specimens have been linearly interpolated between elements.

Three-dimensional dynamic. Several demanding simulation requirements arise when modeling shear wave propagation in soft, nearly incompressible materials. Figure 3 (for the one-dimensional simulations)

---

[46] Measurements of axial stress in quasistatic torsion tests are common, and such measurements could perhaps be done in torsional Kolsky bar tests as well. However, it seems unlikely that radial or hoop stresses could ever be measured.

shows that, when a specimen is far from dynamic equilibrium, large gradients in strain exist. These large gradients cannot be captured in a numerical simulation without a sufficiently fine mesh. In *Simulation I*, there were changes in strain of 0.4 over distances of approximately 0.6 mm. A large number of elements along the shortest dimension of the specimen geometry requires extremely large meshes to model the entire specimen in a three-dimensional simulation. A large reduction in the number of elements is gained by utilizing the rotational symmetry of the problem and effectively changing it to a two-dimensional problem by simulating a thin wedge with periodic boundaries. An explicit code would require very short time steps for these small elements. Simulations were performed using Adagio with HHT integration [Hilber et al. 1977]. This enabled taking larger time steps while maintaining stability and introducing a small damping to higher frequencies.

The software used for meshing and postprocessing was the same as for the quasistatic simulations. Utilizing the rotational symmetry of the problem, variables were evaluated along axial lines at a single angle ($\Theta = 0$) and five equally spaced radial locations from R_i to R_o. For the simulations with a viscoelastic specimen, we used the Viscoelastic Swanson Model in Sierra SolidMechanics. The parameters in the elastic part of that model were chosen so that it reduced to a Mooney–Rivlin model.

Appendix B: Mathematical formulation of a smooth loading pulse

The simulations of the torsional Kolsky bar test require a loading pulse (i.e., an applied average strain-rate history $\dot{\gamma}_s$) that ramps up smoothly to a constant value before subsequently unloading (Figure 2a). In this appendix, we formulate a parametrized loading pulse using a Hermitian smoothing spline. The time integral of the average strain-rate $\dot{\gamma}_s$ can then be used to obtain an applied average shear strain γ_s and ultimately the applied displacement boundary condition (2-6).

We use a Hermitian smoothing spline of degree 5 as the basis for the ramp-up portion of the loading pulse (see [Fitzpatrick and Scheidler 2013]):

$$H_5(x) = 10x^3 - 15x^4 + 6x^5, \quad 0 \le x \le 1. \tag{B-1}$$

This function increases from 0 at $x = 0$ to 1 at $x = 1$ and has zero first and second derivatives at both of these end points. Following [Fitzpatrick and Scheidler 2013], one can use $H_5(x)$ to construct a strain-rate function that ramps up from zero to $\dot{\gamma}_{\max}$ over the time interval $[0, t_r]$, maintains this constant value over the time interval $[t_r, t_r + t_p]$, and then unloads to zero over the time interval $[t_r + t_p, t_d]$:

$$\dot{\gamma}_s(t) = \begin{cases} 0, & t < 0, \\ \dot{\gamma}_{\max} H_5\left(\dfrac{t}{t_r}\right), & 0 \le t \le t_r, \\ \dot{\gamma}_{\max}, & t_r < t < t_r + t_p, \\ \dot{\gamma}_{\max}\left[1 - H_5\left(\dfrac{t - (t_r + t_p)}{t_r}\right)\right], & t_r + t_p \le t \le t_d, \\ 0, & t > t_d. \end{cases} \tag{B-2}$$

Here t_r is referred to as the rise time, i.e., the time it takes to reach a constant strain-rate, t_p is the duration of the constant strain-rate plateau, and t_d is the total duration of the pulse. In the simulations, we made the additional assumption that the loading pulse is symmetric; that is, the unloading duration $t_d - (t_r + t_p)$ equals the rise time so that $t_d = 2t_r + t_p$.

Note that

$$\dddot{\gamma}_s(0) = \dddot{\gamma}_s(t_r) = \dddot{\gamma}_s(t_r + t_p) = 0, \qquad \ddddot{\gamma}_s(0) = \ddddot{\gamma}_s(t_r) = \ddddot{\gamma}_s(t_r + t_p) = 0. \tag{B-3}$$

Since $\dddot{\gamma}_s$ and $\ddddot{\gamma}_s$ are identically zero during the constant strain-rate plateau as well as for $t < 0$ and $t > t_d$, the conditions (B-3) guarantee that $\dot{\gamma}_s$ is twice continuously differentiable. This degree of smoothness was necessary to avoid an unwanted ringing in the simulations that would otherwise result from a lower order polynomial.

An explicit expression for $\gamma_s(t)$ is rather messy, and in practice, it is simpler to work with the integral of H_5:

$$\mathbb{H}_5(x) = \int_0^x H_5(y)\,\mathrm{d}y = x^4\left(x^2 - 3x + \tfrac{5}{2}\right). \tag{B-4}$$

Integrating each case in (B-2) with respect to time, assuming a symmetric loading pulse, and using $\mathbb{H}_5(1) = \tfrac{1}{2}$ gives

$$\gamma_s(t) = \begin{cases} 0, & t < 0, \\ \dot{\gamma}_{\max} t_r \mathbb{H}_5\left(\dfrac{t}{t_r}\right), & 0 \leq t \leq t_r, \\ \dot{\gamma}_{\max}\left[\tfrac{1}{2}t_r + (t - t_r)\right], & t_r < t < t_r + t_p, \\ \dot{\gamma}_{\max}\left[\tfrac{1}{2}t_r + (t - t_r) - t_r \mathbb{H}_5\left(\dfrac{t - (t_r + t_p)}{t_r}\right)\right], & t_r + t_p \leq t \leq 2t_r + t_p, \\ \dot{\gamma}_{\max}[t_r + t_p], & t > 2t_r + t_p = t_d. \end{cases} \tag{B-5}$$

Equations (B-2) and (B-5) are smooth functions that qualitatively reproduce typical strain and strain-rate loading conditions generated in Kolsky bar tests.

Acknowledgements

References

[Abou-Sayed and Clifton 1976] A. S. Abou-Sayed and R. J. Clifton, "Pressure shear waves in fused silica", *J. Appl. Phys.* **47**:5 (1976), 1762–1770.

[Batra 2006] R. C. Batra, *Elements of continuum mechanics*, American Institute of Aeronautics and Astronautics, Reston, VA, 2006.

[Beatty 1987] M. F. Beatty, "Topics in finite elasticity: Hyperelasticity of rubber, elastomers, and biological tissues—with examples", *Appl. Mech. Rev. (ASME)* **40**:12 (1987), 1699–1734.

[Chen and Song 2011] W. Chen and B. Song, *Split Hopkinson (Kolsky) bar: Design, testing and applications*, Springer, New York, 2011.

[Coleman et al. 1965] B. D. Coleman, M. E. Gurtin, and I. Herrera, "The velocity of one-dimensional shock and acceleration waves", pp. 1–19 in *Wave propagation in dissipative materials*, Springer, Berlin, 1965.

[Davison 1966] L. Davison, "Propagation of plane waves of finite amplitude in elastic solids", *J. Mech. Phys. Solids* **14**:5 (1966), 249–270.

[Donnelly and Medige 1997] B. R. Donnelly and J. Medige, "Shear properties of human brain tissue", *J. Biomech. Eng.* (*ASME*) **119**:4 (1997), 423–432.

[Fitzpatrick and Scheidler 2013] J. Fitzpatrick and M. Scheidler, "Considerations for numerical modeling of dynamic behavior of soft materials", pp. 29–39 in *Dynamic behavior of materials, I* (Costa Mesa, CA, 2012), edited by V. Chalivendra et al., Springer, New York, 2013.

[Gilat 2000] A. Gilat, "Torsional Kolsky bar testing", pp. 505–515 in *Mechanical testing and evaluation*, 10th ed., edited by H. Kuhn and D. Medlin, ASM Handbook **8**, ASM International, Materials Park, OH, 2000.

[Graff 1975] K. F. Graff, *Wave motion in elastic solids*, Ohio State University Press, Columbus, OH, 1975.

[Gray 2000] G. T. Gray, "Classic split-Hopkinson pressure bar testing", pp. 462–476 in *Mechanical testing and evaluation*, 10th ed., edited by H. Kuhn and D. Medlin, ASM Handbook **8**, ASM International, Materials Park, OH, 2000.

[Green and Adkins 1960] A. E. Green and J. E. Adkins, *Large elastic deformations*, Clarendon Press, Oxford, 1960.

[Hartley et al. 1985] K. A. Hartley, J. Duffy, and R. H. Hawley, "The torsional Kolsky (split Hopkinson) bar", pp. 218–228 in *Mechanical testing*, 9th ed., edited by J. R. Newby, Metals Handbook **8**, American Society for Metals, Metals Park, OH, 1985.

[Hilber et al. 1977] H. M. Hilber, T. J. R. Hughes, and R. L. Taylor, "Improved numerical dissipation for time integration algorithms in structural dynamics", *Earthq. Eng. Struct. Dyn.* **5**:3 (1977), 283–292.

[Hill and Lee 1989] J. M. Hill and A. I. Lee, "Combined compression and torsion of circular cylindrical pads of rubber", *J. Mech. Phys. Solids* **37**:2 (1989), 175–190.

[Hill and Wegner 2004] J. M. Hill and J. L. Wegner, "New families of exact nonlinear waves for the neo-Hookean finite elastic solid", *Math. Mech. Solids* **9**:1 (2004), 81–95.

[Hrapko et al. 2006] M. Hrapko, J. A. W. van Dommelen, G. W. M. Peters, and J. S. H. M. Wismans, "The mechanical behaviour of brain tissue: Large strain response and constitutive modelling", *Biorheology* **43**:5 (2006), 623–636.

[Miller and Chinzei 1997] K. Miller and K. Chinzei, "Constitutive modelling of brain tissue: Experiment and theory", *J. Biomech.* **30**:11-12 (1997), 1115–1121.

[Mooney 1940] M. Mooney, "A theory of large elastic deformation", *J. Appl. Phys.* **11**:9 (1940), 582–592.

[Nicolle et al. 2004] S. Nicolle, M. Lounis, and R. Willinger, "Shear properties of brain tissue over a frequency range relevant for automotive impact situations: New experimental results", *Stapp Car Crash J.* **48** (2004), 239.

[Nie et al. 2011] X. Nie, R. Prabhu, W. W. Chen, J. M. Caruthers, and T. Weerasooriya, "A Kolsky torsion bar technique for characterization of dynamic shear response of soft materials", *Exp. Mech.* **51**:9 (2011), 1527–1534.

[Nie et al. 2013] X. Nie, B. Sanborn, T. Weerasooriya, and W. Chen, "High-rate bulk and shear responses of bovine brain tissue", *Int. J. Impact Eng.* **53** (2013), 56–61.

[Rivlin 1947] R. S. Rivlin, "Torsion of a rubber cylinder", *J. Appl. Phys.* **18**:5 (1947), 444–449.

[Rivlin 1948a] R. S. Rivlin, "Some applications of elasticity theory to rubber engineering", pp. 1–8 in *Proceedings of the 2nd Rubber Technology Conference* (London, 1948), edited by T. R. Dawson, Heffer, Cambridge, 1948.

[Rivlin 1948b] R. S. Rivlin, "Large elastic deformations of isotropic materials, IV: Further developments of the general theory", *Phil. Trans. R. Soc. A* **241**:835 (1948), 379–397.

[Rivlin 1949] R. S. Rivlin, "Large elastic deformations of isotropic materials, VI: Further results in the theory of torsion, shear and flexure", *Phil. Trans. R. Soc. A* **242**:845 (1949), 173–195.

[Rivlin and Saunders 1951] R. S. Rivlin and D. W. Saunders, "Large elastic deformations of isotropic materials, VII: Experiments on the deformation of rubber", *Phil. Trans. R. Soc. A* **243**:865 (1951), 251–288.

[Sanborn 2011] B. Sanborn, *An experimental investigation of radial deformation of soft materials in Kolsky bar experiments*, Masters thesis, Purdue University, 2011, Available at http://search.proquest.com/docview/904409338.

[Sanborn et al. 2012] B. Sanborn, X. Nie, W. Chen, and T. Weerasooriya, "Inertia effects on characterization of dynamic response of brain tissue", *J. Biomech.* **45**:3 (2012), 434–439.

[Saraf et al. 2007] H. Saraf, K. T. Ramesh, A. M. Lennon, A. C. Merkle, and J. C. Roberts, "Measurement of the dynamic bulk and shear response of soft human tissues", *Exp. Mech.* **47**:3 (2007), 439–449.

[Scheidler 1998] M. Scheidler, "Response of nonlinear elastic solids to oblique plate impact", pp. 921–924 in *The tenth American Physical Society topical conference on shock compression of condensed matter* (Amherst, MA, 1997), edited by S. C. Schmidt et al., AIP Conf. Proc. **429**, American Institute of Physics, New York, 1998.

[Scheidler and Kraft 2010] M. Scheidler and R. Kraft, "Inertial effects in compression Hopkinson bar tests on soft materials", in *Proceedings of the ARL ballistic protection technologies workshop* (Herndon, VA, 2010), Army Research Laboratory, Adelphi, MD, 2010.

[Scheidler et al. 2011] M. Scheidler, J. Fitzpatrick, and R. Kraft, "Optimal pulse shapes for SHPB tests on soft materials", pp. 259–268 in *Dynamic behavior of materials, I* (Uncasville, CT, 2011), edited by T. Proulx, Springer, New York, 2011.

[Shuck and Advani 1972] L. Z. Shuck and S. H. Advani, "Rheological response of human brain tissue in shear", *J. Basic Eng. (ASME)* **94**:4 (1972), 905–911.

[Treloar 1975] L. R. G. Treloar, *The physics of rubber elasticity*, 3rd ed., Clarendon Press, Oxford, 1975.

[Trexler et al. 2011] M. M. Trexler, A. M. Lennon, A. C. Wickwire, T. P. Harrigan, Q. T. Luong, J. L. Graham, A. J. Maisano, J. C. Roberts, and A. C. Merkle, "Verification and implementation of a modified split Hopkinson pressure bar technique for characterizing biological tissue and soft biosimulant materials under dynamic shear loading", *J. Mech. Behav. Biomed. Mater.* **4**:8 (2011), 1920–1928.

[Truesdell and Noll 1965] C. Truesdell and W. Noll, *The non-linear field theories of mechanics*, Handbuch der Physik **III/3**, Springer, Berlin, 1965.

[Warren and Forrestal 2010] T. L. Warren and M. J. Forrestal, "Comments on the effect of radial inertia in the Kolsky bar test for an incompressible material", *Exp. Mech.* **50**:8 (2010), 1253–1255.

[Wylie 1975] C. R. Wylie, *Advanced engineering mathematics*, 4th ed., McGraw-Hill, New York, 1975.

ADAM SOKOLOW: adam.c.sokolow.civ@mail.mil
U.S. Army Research Laboratory, Soldier Protection Sciences Branch, Aberdeen Proving Ground, MD 21005, United States

MIKE SCHEIDLER: michael.j.scheidler2.ctr@mail.mil
U.S. Army Research Laboratory, Soldier Protection Sciences Branch, Aberdeen Proving Ground, MD 21005, United States

msp

TRANSIENT ELASTIC-VISCOPLASTIC DYNAMICS OF THIN SHEETS

ALI A. ATAI AND DAVID J. STEIGMANN

Dedicated to José J. A. Rodal

A model for the finite transient viscoplastic response of thin membranes is derived from three-dimensional viscoplasticity theory for isotropic materials. This accommodates large elastic strains and is not limited to conventional Kirchhoff–Love kinematics. In particular, we show that the Kirchhoff–Love hypothesis need not obtain in the presence of plastic deformation. Numerical experiments exhibit large transient elastic strains accompanied by small deviations from Kirchhoff–Love kinematics.

1. Introduction

The problem of the dynamic viscoplastic response of thin metallic sheets to impact and blast loads is thoroughly reviewed in the classic monograph [Cristescu 1967]. In addition to a detailed overview of experimental methods, a description of theoretical and numerical analyses of transient finite axisymmetric motions is given in the setting of rate-independent and rate-dependent response. The present work may be viewed as a further development of this subject, cast in the setting of the modern theory of finite elastic-viscoplastic deformations.

In rate-independent plasticity theory the elastic strain is bounded by the diameter of an *elastic range* associated with a yield criterion. Typically, this implies that elastic strains are small enough to justify the use of classical linear relations between elastic strain and an appropriate measure of stress. In contrast, formulations of viscoplasticity theory to model rate-dependent behavior are characterized by significant excursions of the elastic strain (and associated stress) from the elastic range [Malvern 1951; Prager 1961; Perzyna 1962/1963; 1966]. In this case the elastic strain cannot be regarded as small *a priori* and so there is a need for an extended framework that accommodates finite elastic strain. To this end we adopt the finite-elastic-strain model for isotropic materials proposed in [Krishnan and Steigmann 2014].

The basic framework of finite elastoplasticity theory is recalled in Section 2, both for the sake of completeness and to set the stage for its subsequent application, in Section 3, to the dynamics of thin sheets. We show that the kinematics of the sheet do not conform to classical Kirchhoff–Love kinematics, even in the case of isotropy. In Section 4 we describe numerical experiments conducted using a two-dimensional spatial finite difference scheme based on Green's theorem in conjunction with explicit timewise integration of the equations of motion. This is applied to the simulation of the response of a plane sheet to transverse blast pressure. The predictions exhibit small deviations from Kirchhoff–Love kinematics and substantial transient elastic strains.

From the theoretical point of view it is advantageous to base the theory on the elastic stretch tensor rather than conventional measures of elastic strain; this is explained in Section 2. Typically the use of

stretch tensors is avoided in numerical work as they are not rational functions of the deformation gradient. However, as shown in Section 4, this issue is easily addressed by using an appropriate version of the Cayley–Hamilton formula.

We use standard notation such as A^t, A^{-1}, A^*, Dev A, tr A and J_A. These are, respectively, the transpose, the inverse, the cofactor, the deviatoric part, the trace and the determinant of a tensor A, regarded as a linear transformation from a three-dimensional vector space to itself, the latter being identified with the translation space of the usual three-dimensional Euclidean point space. We also use Sym to denote the linear space of symmetric tensors, Sym$^+$ the positive-definite symmetric tensors and Orth$^+$ the group of rotation tensors. If $J_A > 0$ then we have the unique polar decompositions $A = R_A U_A = V_A R_A$, with $R_A \in$ Orth$^+$ and U_A, $V_A \in$ Sym$^+$. The tensor product of 3-vectors is indicated by interposing the symbol $\otimes$, and the Euclidean inner product of tensors A, B is denoted and defined by $A \cdot B = \text{tr}(AB^t)$; the associated norm is $|A| = \sqrt{A \cdot A}$. Finally, the notation F_A, with a bold subscript, stands for the tensor-valued derivative of a scalar-valued function $F(A)$.

2. Elastoviscoplasticity theory for isotropic materials

In this section we recount the basic elements of the three-dimensional theory underpinning this work. Further background may be found in [Cleja-Ţigoiu and Soós 1990; Epstein and Elżanowski 2007; Rajagopal and Srinivasa 1998; Gurtin et al. 2010; Gupta et al. 2007; Bigoni 2012].

2.1. *Basic theory.* The fields to be determined are the motion $\chi(x, t)$ and the *plastic* deformation tensor $K(x, t)$, where x is the position of a material point in a fixed reference placement κ_r of the body. Commonly, the plastic deformation is identified with $G = K^{-1}$. The values $y = \chi(x, t)$ are the positions of material points at time t and generate the current placement κ_t of the body as x ranges over κ_r. The deformation gradient, denoted by F, is the gradient of χ with respect to x; this is assumed to be invertible with $J_F > 0$. These variables combine to yield the *elastic* deformation

$$H = FK. \tag{1}$$

Here we impose $J_H > 0$ and thus require that $J_K > 0$.

The basic elements of this framework were laid down by Bilby [1960], Kröner [1960], Noll [1967/1968] and Lee [1969]. Reference may be made to [Gurtin et al. 2010] for a thorough and modern account of the subject.

The strain energy of the body is

$$E = \int_{\kappa_t} \psi(H) \, dv, \tag{2}$$

where ψ is the spatial strain-energy density. We consider materials that are uniform in the sense that this function, and further constitutive functions to be discussed, do not involve x explicitly.

The local equations of motion, in the absence of body forces, are

$$\text{Div } P = \rho_r \ddot{y}, \quad PF^t \in \text{Sym} \quad \text{in } \kappa_r, \tag{3}$$

where P is the Piola stress, ρ_r is the fixed referential mass density, Div is the referential divergence (i.e., the divergence with respect to x), and superposed dots are used to denote material derivatives ($\partial/\partial t$ at

fixed $\boldsymbol{x}$). The Piola stress is defined in terms of the Cauchy stress $\boldsymbol{T}$ by

$$\boldsymbol{P} = \boldsymbol{T}\boldsymbol{F}^*. \tag{4}$$

The strain-energy function referred to the local *intermediate* configuration κ_i is

$$W(\boldsymbol{H}) = J_H \psi(\boldsymbol{H}), \tag{5}$$

and it generates the Cauchy stress via the formula [Gupta et al. 2007]

$$\boldsymbol{T}\boldsymbol{H}^* = W_H. \tag{6}$$

Accordingly,

$$W_H = \boldsymbol{P}\boldsymbol{K}^* \tag{7}$$

Necessary and sufficient for the symmetry condition $(3)_2$ is that W depend on $\boldsymbol{H}$ through the *elastic* Cauchy–Green deformation tensor

$$\boldsymbol{C}_H = \boldsymbol{H}^t\boldsymbol{H}. \tag{8}$$

Thus,

$$W(\boldsymbol{H}) = \widehat{W}(\boldsymbol{C}_H). \tag{9}$$

The associated second Piola–Kirchhoff stress, referred to κ_i, is $\boldsymbol{S} = \hat{\boldsymbol{S}}(\boldsymbol{C}_H)$, where

$$\hat{\boldsymbol{S}}(\boldsymbol{C}_H) = 2\widehat{W}_{\boldsymbol{C}_H}. \tag{10}$$

We assume the local configuration κ_i to be *natural* in the sense that $\hat{\boldsymbol{S}}(\boldsymbol{I}) = \boldsymbol{0}$; realistic constitutive hypotheses [Gupta et al. 2007] then associate it with an *undistorted* state, in the sense of an undistorted crystal lattice. The relevant symmetry group is thus a subgroup of the proper orthogonal group; i.e.,

$$W(\boldsymbol{H}) = W(\boldsymbol{H}\boldsymbol{R}), \tag{11}$$

where $\boldsymbol{R} \in \mathrm{Orth}^+$. For isotropic materials the symmetry group coincides with the proper orthogonal group, implying that this is satisfied for *all* $\boldsymbol{R} \in \mathrm{Orth}^+$.

The sum of the kinetic and strain energies of an arbitrary part $p \subset \kappa_t$ of the body is

$$\int_\pi \Phi \, dv; \quad \Phi = \Psi + \tfrac{1}{2}\rho_r|\dot{\boldsymbol{y}}|^2, \tag{12}$$

where π is the region occupied by p in κ_r, and

$$\Psi(\boldsymbol{F}, \boldsymbol{K}) = J_K^{-1} W(\boldsymbol{F}\boldsymbol{K}) \tag{13}$$

is the referential strain-energy density. In terms of this the Piola stress is given simply by [Epstein and Elżanowski 2007; Gupta et al. 2007]

$$\boldsymbol{P} = \Psi_F. \tag{14}$$

The dissipation $\mathscr{D}$ is the difference between the mechanical power P supplied to p and the rate of change of the total energy in p. Thus,

$$\mathscr{D} = P - \frac{d}{dt}\int_\pi \Phi \, dv, \tag{15}$$

which may be reduced to [Gupta et al. 2011]

$$\mathscr{D} = \int_\pi D \, dv, \tag{16}$$

where

$$D = \mathscr{E} \cdot \dot{\boldsymbol{K}} \boldsymbol{K}^{-1}, \tag{17}$$

in which

$$\mathscr{E} = \Psi \boldsymbol{I} - \boldsymbol{F}^t \boldsymbol{P} \tag{18}$$

is Eshelby's energy-momentum tensor.

The dissipation is thus nonnegative for every sub-body if and only if $D \geq 0$. It is convenient to use (17) in the form

$$J_K D = \mathscr{E}' \cdot \boldsymbol{K}^{-1} \dot{\boldsymbol{K}}, \tag{19}$$

where

$$\mathscr{E}' = J_K \boldsymbol{K}^t \mathscr{E} \boldsymbol{K}^{-t} \tag{20}$$

is the pushforward of the Eshelby tensor to κ_i. This satisfies [Gupta et al. 2007]

$$\mathscr{E}' = \widehat{W}(\boldsymbol{C}_H) \boldsymbol{I} - \boldsymbol{C}_H \hat{\boldsymbol{S}}(\boldsymbol{C}_H), \tag{21}$$

and is therefore purely elastic in origin.

In [Gupta et al. 2007] it is further demonstrated that if the strain energy and the dissipation are invariant under superposed rigid-body motions with uniform rotation $\boldsymbol{Q}(t)$, and if plastic evolution is *strictly dissipative* in the sense that $D > 0$ if and only if $\dot{\boldsymbol{K}} \neq \boldsymbol{0}$, then the transformation rules for the elastic and plastic deformations under superposed rigid-body motions are

$$\boldsymbol{H} \to \boldsymbol{Q}(t)\boldsymbol{H} \quad \text{and} \quad \boldsymbol{K} \to \boldsymbol{K}. \tag{22}$$

These imply that $\boldsymbol{C}_H$, $\boldsymbol{S}$ and $\mathscr{E}'$ are invariant.

In this work we consider strain-energy functions Ψ that satisfy the strong ellipticity condition

$$\boldsymbol{a} \otimes \boldsymbol{b} \cdot \Psi_{FF}(\boldsymbol{F}, \boldsymbol{K})[\boldsymbol{a} \otimes \boldsymbol{b}] > 0 \quad \text{for all} \quad \boldsymbol{a} \otimes \boldsymbol{b} \neq 0, \tag{23}$$

and for all deformations. This is equivalent to [Sfyris 2011; Steigmann 2014]

$$\boldsymbol{a} \otimes \boldsymbol{m} \cdot W_{HH}(\boldsymbol{H})[\boldsymbol{a} \otimes \boldsymbol{m}] > 0 \quad \text{for all} \quad \boldsymbol{a} \otimes \boldsymbol{m} \neq 0, \quad \text{with } \boldsymbol{m} = \boldsymbol{K}^t \boldsymbol{b}. \tag{24}$$

It follows that Ψ is strongly elliptic at $\boldsymbol{F}$ if and only if W is strongly elliptic at $\boldsymbol{H} = \boldsymbol{F}\boldsymbol{K}$.

2.2. *Isotropy.* Isotropy of the constitutive response implies that the strain-energy function satisfies (11) for all rotations $\boldsymbol{R}$. The choice $\boldsymbol{R} = \boldsymbol{R}_H^t$ yields the necessary condition $W(\boldsymbol{H}) = W(\boldsymbol{V}_H)$. Invariance of W under superposed rigid-body motions imposes the further restriction (see (22)$_1$) $W(\boldsymbol{V}_H) = W(\boldsymbol{Q}\boldsymbol{V}_H\boldsymbol{Q}^t)$ for all rotations $\boldsymbol{Q}$, which is satisfied if and only if W is expressible in the form

$$W(\boldsymbol{H}) = w(h_1, h_2, h_3), \tag{25}$$

where h_i are the principal invariants of the elastic left-stretch $\boldsymbol{V}_H$. Because these are isotropic functions, they are also the invariants of the elastic right-stretch $\boldsymbol{U}_H$; i.e.,

$$h_1 = \operatorname{tr} \boldsymbol{U}_H, \quad h_2 = \operatorname{tr} \boldsymbol{U}_H^*, \quad h_3 = \det \boldsymbol{U}_H = J_H, \tag{26}$$

and this of course is a special case of (9) because $\boldsymbol{U}_H$ is determined by $\boldsymbol{C}_H$. Equation (25) thus yields the canonical representation of an isotropic, frame-invariant strain-energy function. A representation formula derived in [Steigmann 2002] may then be used to arrive at

$$W_H = \boldsymbol{R}_H \boldsymbol{\sigma}, \tag{27}$$

where

$$\boldsymbol{\sigma} = (w_1 + h_1 w_2)\boldsymbol{I} - w_2 \boldsymbol{U}_H + w_3 \boldsymbol{U}_H^*, \tag{28}$$

in which

$$w_i = \frac{\partial w}{\partial h_i} \tag{29}$$

is the Biot stress based on the use of κ_i as reference [Ogden 1997]. Using (7), (10) and (27) we have $\boldsymbol{C}_H \boldsymbol{S} = \boldsymbol{U}_H \boldsymbol{\sigma}$, yielding (21) in the form

$$\mathscr{E}' = W\boldsymbol{I} - \boldsymbol{U}_H \boldsymbol{\sigma} = (w - h_3 w_3)\boldsymbol{I} - (w_1 + h_1 w_2)\boldsymbol{U}_H + w_2 \boldsymbol{U}_H^2. \tag{30}$$

Our preference for a framework based on the stretch tensor and associated invariants is due to the availability of simple sufficient conditions, expressed in terms of these variables, for the condition of polyconvexity. This in turn guarantees strong ellipticity, which plays an important role in the considerations of Section 3.

To elaborate, we write the strain energy of the body in the form

$$E = \int_{\kappa_r} \Psi(\nabla \boldsymbol{\chi}, \boldsymbol{K}) \, dv, \tag{31}$$

where (cf. (13))

$$\Psi(\nabla \boldsymbol{\chi}, \boldsymbol{K}) = J_K^{-1} W((\nabla \boldsymbol{\chi})\boldsymbol{K}). \tag{32}$$

The function $\Psi(\,\cdot\,, \boldsymbol{K})$, with $\boldsymbol{K}(\boldsymbol{x})$ fixed, delivers the strain energy of an inhomogeneous elastic body.

Polyconvexity is the condition that there exists a (possibly nonunique) function $\Phi_{(\boldsymbol{x})}(\boldsymbol{F}, \boldsymbol{F}^*, J_F)$, jointly convex in each argument, such that $\Phi_{(\boldsymbol{x})}(\boldsymbol{F}, \boldsymbol{F}^*, J_F) = \Psi(\boldsymbol{F}, \boldsymbol{K}(\boldsymbol{x}))$. This in turn is equivalent to the polyconvexity of the function $\Phi'_{(\boldsymbol{x})} = W$, where $\Phi'_{(\boldsymbol{x})}(\boldsymbol{H}, \boldsymbol{H}^*, J_H) = J_K \Phi_{(\boldsymbol{x})}(\boldsymbol{H}\boldsymbol{K}^{-1}, (\boldsymbol{H}\boldsymbol{K}^{-1})^*, J_H J_K^{-1})$ with $\boldsymbol{K}$ fixed [Neff 2003]. In the case of isotropy, sufficient conditions are [Steigmann 2003]

$$
\begin{array}{lll}
\text{(i)} & w(h_1, h_2, h_3) \text{ is a convex function of all three arguments jointly,} & \\
\text{(ii)} & w \text{ is an increasing function of } h_1 \text{ and } h_2; &
\end{array} \tag{33}
$$

that is,

$$w(\bar{h}_1, \bar{h}_2, \bar{h}_3) - w(h_1, h_2, h_3) > (\bar{h}_1 - h_1)\frac{\partial w}{\partial h_1} + (\bar{h}_2 - h_2)\frac{\partial w}{\partial h_2} + (\bar{h}_3 - h_3)\frac{\partial w}{\partial h_3}, \tag{34}$$

together with

$$\frac{\partial w}{\partial h_1} > 0 \quad \text{and} \quad \frac{\partial w}{\partial h_2} > 0, \tag{35}$$

in which h_k and $\bar{h}_k$, respectively, are the invariants associated with $\boldsymbol{H}$ and the comparison deformation $\bar{\boldsymbol{H}}$, and the derivatives are evaluated at h_k.

For example, strain energies of the form

$$w = c_1(h_1 - 3) + c_2(h_2 - 3) + g(h_3), \tag{36}$$

with c_1 and c_2 constant, have yielded explicit solutions to some boundary-value problems [Carroll 1988] in the setting of finite elasticity theory. These satisfy (33) — and thus yield polyconvexity — if and only if $c_1 > 0$, $c_2 > 0$ and $g''(h_3) > 0$. An example of such a function $g(\cdot)$ is

$$g(h_3) = -c_3 \log h_3, \tag{37}$$

with c_3 a positive constant, and the associated Biot stress is (cf. (28))

$$\boldsymbol{\sigma} = (c_1 + h_1 c_2)\boldsymbol{I} - c_2 \boldsymbol{U}_H - c_3 \boldsymbol{U}_H^{-1}. \tag{38}$$

To ensure that the intermediate configuration κ_i is stress-free, as required, and that the asymptotic formula

$$\boldsymbol{\sigma} = \lambda(\operatorname{tr}\boldsymbol{\epsilon})\boldsymbol{I} + 2\mu\boldsymbol{\epsilon} + o(|\boldsymbol{\epsilon}|) \tag{39}$$

is satisfied for small $|\boldsymbol{\epsilon}|$, where

$$\boldsymbol{\epsilon} = \boldsymbol{U}_H - \boldsymbol{I} \tag{40}$$

is the elastic Biot strain and where λ and μ are the usual Lamé moduli, we impose

$$c_3 = c_1 + 2c_2, \quad c_2 = \lambda \quad \text{and} \quad \tfrac{1}{2}(c_1 + c_2) = \mu. \tag{41}$$

The polyconvexity criteria (33) then imply the classical inequalities $\mu > 0$ and $\kappa > 0$, where μ and $\kappa\left(= \lambda + \tfrac{2}{3}\mu\right)$, respectively, are the conventional shear and bulk moduli. Accordingly, for materials possessing a positive modulus λ, equations (36), (37) and (41) provide a simple nonlinear, polyconvex extension of the strain-energy function of linear elasticity theory to finite elastic strains.

Finally, following [Krishnan and Steigmann 2014], we adopt the isotropic viscoplastic flow rule

$$\nu \dot{\boldsymbol{G}} \boldsymbol{G}^{-1} = F \operatorname{Dev}(\boldsymbol{\sigma}\boldsymbol{U}_H); \quad F > 0, \quad \text{where} \quad F = 1 - \frac{\sqrt{2}K}{|\operatorname{Dev}(\boldsymbol{\sigma}\boldsymbol{U}_H)|}, \tag{42}$$

$\nu(> 0)$ is a material viscosity and K is the static yield stress in shear. This is an extension of the classical over-stress models pioneered by Malvern [1951], Prager [1961] and Perzyna [1962/1963; 1966]. We impose $\dot{\boldsymbol{G}} = 0$ if $\boldsymbol{U}_H$ belongs to the elastic range, defined by $F \leq 0$. In the case of nontrivial plastic evolution the elastic stretch is not bounded by the elastic range, in contrast to the situation in rate-independent plasticity. For this reason it is generally necessary to account for finite elastic strain in the presence of viscoplasticity.

We note that the skew part of $\dot{\boldsymbol{G}}\boldsymbol{G}^{-1}$, the so-called *plastic spin*, is suppressed in (42). That this entails no loss of generality in the case of isotropic response has been established in [Epstein and Elżanowski 2007] and [Gurtin et al. 2010]. A general framework for addressing issues of this kind is discussed in [Steigmann and Gupta 2011].

Using $\boldsymbol{K}^{-1}\dot{\boldsymbol{K}} = -\dot{\boldsymbol{G}}\boldsymbol{G}^{-1}$, the dissipation D, defined by (19), is easily shown to vanish if $F \leq 0$, and to satisfy

$$D > 2FK^2/\nu \quad \text{if} \ F > 0, \tag{43}$$

ensuring that plastic evolution is indeed strictly dissipative.

3. Membrane dynamics

We identify the reference configuration κ_r with the prismatic region $\Omega \times \left[-\frac{1}{2}h, \frac{1}{2}h\right]$, where Ω is the midplane of the sheet and h is its thickness. To obtain the relevant model we restrict the exact equations of motion (3) to Ω and invoke the exact traction conditions at the lateral surfaces $\varsigma = \pm\frac{1}{2}h$. The resulting system delivers equations of motion for the sheet valid to leading order in h [Steigmann 2009].

3.1. *Equations of motion.* Let $\boldsymbol{k}$ be a unit vector that orients the plane Ω. The associated projection operator is

$$\boldsymbol{1} = \boldsymbol{I} - \boldsymbol{k} \otimes \boldsymbol{k}, \tag{44}$$

where $\boldsymbol{I}$ is the identity for 3-space. This generates the orthogonal decomposition

$$\boldsymbol{P} = \boldsymbol{P}\boldsymbol{1} + \boldsymbol{P}\boldsymbol{k} \otimes \boldsymbol{k} \tag{45}$$

of the Piola stress, which may be used to cast the equation of motion (3) in the form

$$\text{div}(\boldsymbol{P}\boldsymbol{1}) + \boldsymbol{P}'\boldsymbol{k} = \rho_r \ddot{\boldsymbol{y}}, \tag{46}$$

where $\text{div}(\,\cdot\,)$ is the two-dimensional divergence with respect to position $\boldsymbol{u} \in \Omega$, and $(\,\cdot\,)' = \partial(\,\cdot\,)/\partial\varsigma$ is the derivative with respect to the linear coordinate ς orthogonal to Ω in the representation $\boldsymbol{x} = \boldsymbol{u} + \varsigma\boldsymbol{k}$.

This holds at all points in the interior of the body and hence at the midplane Ω defined by $\varsigma = 0$; thus,

$$\text{div}(\boldsymbol{P}_0\boldsymbol{1}) + \boldsymbol{P}_0'\boldsymbol{k} = \rho_r \ddot{\boldsymbol{r}}, \tag{47}$$

where $\boldsymbol{r} = \boldsymbol{\chi}_0$ and $(\,\cdot\,)_0$ is used to denote the restriction of the enclosed variable to Ω. Here,

$$\boldsymbol{P}_0 = \Psi_{\boldsymbol{F}}(\boldsymbol{F}_0, \boldsymbol{K}_0), \tag{48}$$

where

$$\boldsymbol{F}_0 = \nabla\boldsymbol{r} + \boldsymbol{d} \otimes \boldsymbol{k}, \tag{49}$$

in which $\boldsymbol{d} = \boldsymbol{\chi}_0'$ is the membrane director field and $\nabla(\,\cdot\,)$ is the two-dimensional gradient with respect to $\boldsymbol{u}$. This follows easily from the decomposition $\boldsymbol{F} = \boldsymbol{F}\boldsymbol{1} + \boldsymbol{F}\boldsymbol{k} \otimes \boldsymbol{k}$.

Equation (47) is the exact equation of motion for the midplane Ω. Approximations arise when using it to represent material response in $\Omega \times \left[-\frac{1}{2}h, \frac{1}{2}h\right]$. Here we seek the leading-order model for small thickness h, which is assumed to be much smaller than any other length scale in the considered problem. The smallest of these is used as the unit of length, so that $h \ll 1$ when nondimensionalized. To this end we impose lateral traction data at $\varsigma = \pm\frac{1}{2}h$, obtaining [Steigmann 2009]

$$\boldsymbol{p}^+ + \boldsymbol{p}^- = h\boldsymbol{P}_0'\boldsymbol{k} + o(h) \quad \text{and} \quad \boldsymbol{p}^+ - \boldsymbol{p}^- = 2\boldsymbol{P}_0\boldsymbol{k} + o(h), \tag{50}$$

where $\boldsymbol{p}^\pm = \pm\boldsymbol{P}^\pm\boldsymbol{k}$ are the tractions at the major surfaces.

In this work we prescribe

$$\boldsymbol{p}^+ = \boldsymbol{0} \quad \text{and} \quad \boldsymbol{p}^- = p(\boldsymbol{F}^*)^-\boldsymbol{k}, \quad \text{with } p = hP + o(h) \quad \text{and} \quad P = O(1), \tag{51}$$

corresponding to a pressure p of order $O(h)$ acting at $\varsigma = -\frac{1}{2}h$. This is reconciled with (50) if and only if

$$\boldsymbol{P}_0\boldsymbol{k} = \boldsymbol{0} \quad \text{and} \quad \boldsymbol{P}_0'\boldsymbol{k} = P\alpha\boldsymbol{n} + o(h)/h, \tag{52}$$

where $\boldsymbol{n}$ is the unit normal to the image $\omega = \chi(\Omega, t)$ of the midplane after deformation and α is the areal stretch, defined by Nanson's formula

$$\alpha\boldsymbol{n} = \boldsymbol{F}_0^*\boldsymbol{k}, \quad \text{with} \quad \alpha = |\boldsymbol{F}_0^*\boldsymbol{k}|. \tag{53}$$

Here we have used the fact — valid for smooth deformations — that $(\boldsymbol{F}^*)^-$ is approximated by $\boldsymbol{F}_0^*$ with an error of order $O(h)$.

Substitution of (52) into (47) delivers

$$\text{div}(\boldsymbol{P}_0\boldsymbol{1}) + P\alpha\boldsymbol{n} + o(h)/h = \rho_r\ddot{\boldsymbol{r}}, \tag{54}$$

and passage to the limit yields the leading-order differential-algebraic system

$$\text{div}(\boldsymbol{P}_0\boldsymbol{1}) + P\alpha\boldsymbol{n} = \rho_r\ddot{\boldsymbol{r}} \quad \text{and} \quad \boldsymbol{P}_0\boldsymbol{k} = \boldsymbol{0}. \tag{55}$$

Combining this with (14) and the restriction to Ω of the flow rule (42), we arrive at a system for the determination of the plastic deformation $\boldsymbol{K}_0$, the midplane motion $\boldsymbol{r}$ and the director field $\boldsymbol{d}$.

To address the requirement $J_{F_0} > 0$, we observe that

$$J_{F_0} = \boldsymbol{F}_0^*\boldsymbol{k} \cdot \boldsymbol{F}_0\boldsymbol{k}. \tag{56}$$

Accordingly, $J_{F_0} > 0$ if and only if

$$\boldsymbol{d} \cdot \boldsymbol{n} > 0. \tag{57}$$

Henceforth we work exclusively with functions defined on Ω and thus drop the subscript $(\cdot)_0$ for the sake of convenience.

3.2. *Elimination of the director field.* The second equation in (55) requires that Ω be in a state of plane stress. Using (7), this is seen to be equivalent to

$$\{W_{\boldsymbol{H}}(\boldsymbol{H})\}\boldsymbol{l} = 0, \quad \text{where } \boldsymbol{l} = \boldsymbol{K}^t\boldsymbol{k}. \tag{58}$$

To prove that this system yields a unique $\boldsymbol{d}$, we first show that any solution, $\bar{\boldsymbol{d}}$ say, minimizes W. To this end we fix $\nabla\boldsymbol{r}$ and $\boldsymbol{K}$ and define $R(\boldsymbol{d}) = W(\boldsymbol{H})$ with $\boldsymbol{H} = (\nabla\boldsymbol{r} + \boldsymbol{d} \otimes \boldsymbol{k})\boldsymbol{K}$. Let $\boldsymbol{d}(t)$ be a one-parameter family belonging to the half-space $S_+(\boldsymbol{d})$ defined by $\boldsymbol{d} \cdot \boldsymbol{n} > 0$. This is the admissible set associated with the restriction $J_F > 0$. The derivatives of $\sigma(t) = R(\boldsymbol{d}(t))$ are

$$\dot{\sigma} = \dot{\boldsymbol{d}} \cdot \{W_{\boldsymbol{H}}(\boldsymbol{H})\}\boldsymbol{l} = \dot{\boldsymbol{d}} \cdot R_{\boldsymbol{d}} \tag{59}$$

and

$$\ddot{\sigma} = \ddot{\boldsymbol{d}} \cdot \{W_{\boldsymbol{H}}(\boldsymbol{H})\}\boldsymbol{l} + \dot{\boldsymbol{d}} \otimes \boldsymbol{l} \cdot W_{\boldsymbol{H}\boldsymbol{H}}(\boldsymbol{H})[\dot{\boldsymbol{d}} \otimes \boldsymbol{l}] = \ddot{\boldsymbol{d}} \cdot R_{\boldsymbol{d}} + \dot{\boldsymbol{d}} \cdot (R_{\boldsymbol{d}\boldsymbol{d}})\dot{\boldsymbol{d}}. \tag{60}$$

It follows that

$$R_d(\bar{d}) = \{W_H(\bar{H})\}l, \tag{61}$$

with $\bar{H} = (\nabla r + \bar{d} \otimes k)K$, vanishes, and that $R_{dd}(d)$ satisfies

$$\{R_{dd}(d)\}v = \{W_{HH}(H)[v \otimes l]\}l, \tag{62}$$

implying, by the strong ellipticity (cf. (24)) of the polyconvex energy (36), that it is positive definite.

Because $S_+(d)$ is a convex set, it contains the straight line $d(t) = td_2 + (1-t)d_1$ with $d_{1,2} \in S_+(d)$ and $t \in [0, 1]$. We have $\ddot{\sigma} > 0$ on this line and hence $\dot{\sigma}(t) > \dot{\sigma}(0)$ for $t \in (0, 1]$. Then $\sigma(1) - \sigma(0) > \dot{\sigma}(0)$, implying that the function $R(d)$ is convex on S_+; that is,

$$R(d_2) - R(d_1) > R_d(d_1) \cdot (d_2 - d_1). \tag{63}$$

Because such functions have unique stationary points, it follows that there exists a unique solution $d = \bar{d}(\nabla r, K)$ to (58), corresponding to the global minimizer of $R(d)$.

Plastic deformation generally prevents the solution from conforming to classical Kirchhoff–Love kinematics with $d = \mu n$, where μ is the thickness distension. This stands in contrast to the ubiquitous imposition of the constraint of Kirchhoff–Love kinematics throughout the literature on theories for the plastic deformation of membranes and shells derived from three-dimensional considerations [Cristescu 1967; Lubliner 2008].

To prove the claim we invoke (58) in the form (cf. (27))

$$\sigma l = 0, \tag{64}$$

where σ is the Biot stress. Thus, l is an eigenvector of σ with vanishing eigenvalue. Henceforth we normalize l to be a unit vector without loss of generality. It follows from (38) that σ and U_H are coaxial in the case of isotropy, and hence that l is also an eigenvector of U_H. The standard representation $H = \sum \lambda_i m_i \otimes l_i$, where $\lambda_i(> 0)$ are the eigenvalues of U_H, l_i are the associated (orthonormal) eigenvectors and $m_i = R_H l_i$, follows from the polar decomposition theorem and yields $H^* = \sum \lambda_i^* m_i \otimes l_i$, where $\lambda_i^* = \lambda_i / J_H$.

Because $l \in \{l_i\}$ we have $H^* l = \lambda^* m$, with $\lambda^* \in \{\lambda_i^*\}$ and $m \in \{m_i\}$. Using $H^* = F^* K^*$ we obtain $\lambda^* m = (J_K / |K^t k|) F^* k$, which furnishes $\lambda^* = \alpha J_K / |K^t k|$ and $m = n$. Accordingly, it follows from $\lambda m = Hl$ and $d = Fk$ (cf. (49)) that

$$(\lambda / |K^t k|)n = F K K^t F^{-1} d, \tag{65}$$

implying that d is not generally aligned with n. Exceptionally, such alignment occurs — and the director then conforms to Kirchhoff–Love kinematics — if K is a rotation composed with a dilation, including the case of pure elasticity; i.e., $K = I$.

Equation (65) does not account fully for the restrictions embodied in (64). In Section 4, (64) is solved directly for d by using an iterative method.

The present formulation does not yield energetically optimal solutions in the specialization to equilibrium problems. This is due to the potential of the constitutive relations to supply a compressive state of (plane) stress, in violation of a necessary condition for the existence of an energy-minimizing membrane deformation [Pipkin 1986]. In such circumstances the model may be replaced by its quasiconvexification
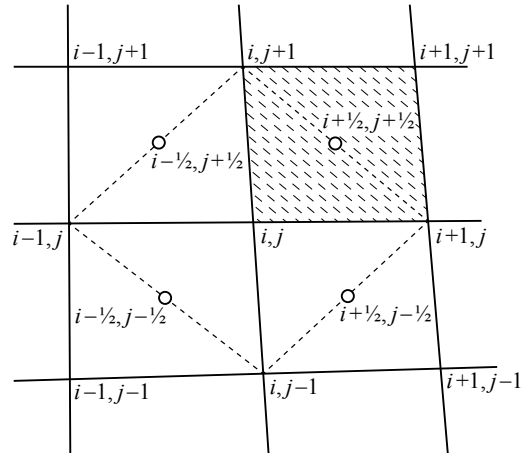
Figure 1. A unit cell of the finite-difference mesh.

[Dacorogna 1989], yielding states that automatically satisfy relevant necessary conditions for energy minimizers. This is the conceptual basis of *tension-field theory* [Steigmann 1990], a model that accommodates finely wrinkled equilibrium states in the context of membrane theory. The same model follows from the method of gamma convergence [Le Dret and Raoult 1996] in the zero-thickness limit. We forego such modifications here, however, as we are concerned exclusively with dynamical states, which of course are not energy minimizers. In particular, the method of gamma convergence is not applicable in this setting. A similar point of view was adopted in [Yokota et al. 2001] in connection with a model for the dynamics of nonlinearly elastic strings. There, dynamics characterized by transient compressive states of stress were obtained via a direct numerical simulation, despite the intermittently nonhyperbolic character of the equations. The present work proceeds in the same spirit.

4. Numerical experiments

4.1. *Finite differences.* We discretize $(55)_1$ using a finite-difference scheme derived from Green's theorem. Applications to plane-strain problems in nonlinear elasticity theory are described in [Silling 1988]. The method was first applied by Wilkins [1963] to the simulation of plane plastic flow. Its application to static problems in membrane theory is developed in [Haseganu and Steigmann 1994; Atai and Steigmann 1998]. Here, we present a brief outline of the method and its adaptation to the description of three-dimensional viscoplastic membrane deformations.

The reference plane Ω is covered by a grid consisting of cells of the kind depicted in Figure 1. Nodes are labeled using integer superscripts (i, j). Thus, $u_\alpha^{i,j}$ are the referential Cartesian coordinates of node (i, j), where $u_\alpha = \boldsymbol{u} \cdot \boldsymbol{i}_\alpha$; $\alpha = 1, 2$, and $\{\boldsymbol{i}_\alpha\}$ is an orthonormal basis in Ω. The four regions adjoining a node and its nearest neighbors are called *zones*. Zone-centered points, identified by open circles in the figure, are labeled using half-integer superscripts.

Green's theorem may be stated in the form

$$\int_D \sigma_{\alpha,\alpha} \, da = e_{\alpha\beta} \int_{\partial D} \sigma_\alpha \, du_\beta, \tag{66}$$

where $\sigma_\alpha(u_1, u_2)$ is a smooth two-dimensional vector field, $e_{\alpha\beta}$ is the two-dimensional permutation symbol ($e_{12} = +1$, etc.), D is an arbitrary simply connected subregion of Ω and commas followed by subscripts are partial derivatives with respect to the coordinates. To approximate the divergence $\sigma_{\alpha,\alpha}$ at node (i, j) we identify D with the quadrilateral bounded by the dashed contour of Figure 1. The left-hand side of (66) is estimated as the nodal value of the integrand multiplied by the area of D; the right-hand side as the zone-centered values of the integrand on each of the four edges of ∂D multiplied by the appropriate length. Thus [Silling 1988],

$$2A^{i,j}(\sigma_{\alpha,\alpha})^{i,j} = e_{\alpha\beta}\big[\sigma_\alpha^{i+1/2,j+1/2}(u_\beta^{i,j+1} - u_\beta^{i+1,j}) + \sigma_\alpha^{i-1/2,j+1/2}(u_\beta^{i-1,j} - u_\beta^{i,j+1})$$
$$+ \sigma_\alpha^{i-1/2,j-1/2}(u_\beta^{i,j-1} - u_\beta^{i-1,j}) + \sigma_\alpha^{i+1/2,j-1/2}(u_\beta^{i+1,j} - u_\beta^{i,j-1})\big], \quad (67)$$

where

$$A^{i,j} = \tfrac{1}{4}\big[(u_2^{i-1,j} - u_2^{i+1,j})(u_1^{i,j+1} - u_1^{i,j-1}) - (u_1^{i-1,j} - u_1^{i+1,j})(u_2^{i,j+1} - u_2^{i,j-1})\big] \quad (68)$$

is one half the area of the quadrilateral.

We also require gradients of functions at zone-centered points. These are derived from the integral formula

$$\int_D \sigma_{,\alpha} \, da = e_{\alpha\beta} \int_{\partial D} \sigma \, du_\beta. \quad (69)$$

We now identify D with the shaded region in the figure. The left-hand side is estimated as the product of the shaded area with the integrand, evaluated at the zone-centered point, and the four edge contributions to the right-hand side are approximated by replacing the integrand in each with the average of the nodal values at the endpoints. This furnishes [Silling 1988]

$$2A^{i+1/2,j+1/2}(\sigma_{,\alpha}^{i+1/2,j+1/2})$$
$$= e_{\alpha\beta}\big[(\sigma^{i+1,j+1} - \sigma^{i,j})(u_\beta^{i,j+1} - u_\beta^{i+1,j}) - (\sigma^{i,j+1} - \sigma^{i+1,j})(u_\beta^{i+1,j+1} - u_\beta^{i,j})\big], \quad (70)$$

where

$$A^{i+1/2,j+1/2} = \tfrac{1}{2}\big[(u_2^{i,j+1} - u_2^{i+1,j})(u_1^{i+1,j+1} - u_1^{i,j}) - (u_1^{i,j+1} - u_1^{i+1,j})(u_2^{i+1,j+1} - u_2^{i,j})\big]. \quad (71)$$

The term $\alpha\boldsymbol{n}$ in (55) associated with the applied pressure may be expressed as a divergence on Ω [Taylor and Steigmann 2009]. Thus, $\boldsymbol{n} = n_k \boldsymbol{i}_k$, with $\boldsymbol{i}_3 = \boldsymbol{k}$, where

$$\alpha n_k = \tfrac{1}{2} e_{ijk} e_{\alpha\beta} r_{i,\alpha} r_{j,\beta} = G_{k\beta,\beta} \quad (72)$$

and

$$G_{k\beta} = \tfrac{1}{2} e_{ijk} e_{\alpha\beta} r_{i,\alpha} r_j, \quad (73)$$

in which e_{ijk} is the three-dimensional permutation symbol ($e_{123} = +1$). For uniformly distributed pressures (55) is thus equivalent to the system

$$T_{k\alpha,\alpha} = \rho_r \ddot{r}_k, \quad \text{where } T_{k\alpha} = P_{k\alpha} + P(t) G_{k\alpha}, \quad (74)$$

where $P_{k\alpha} = \boldsymbol{P} \cdot \boldsymbol{i}_k \otimes \boldsymbol{i}_\alpha$ are the components of $\boldsymbol{P}\boldsymbol{1}$ and $r_k = \boldsymbol{i}_k \cdot \boldsymbol{r}$ are the Cartesian coordinates of a material point after deformation.

Each of the equations (74) is of the form

$$\sigma_{\alpha,\alpha} = \rho_r \ddot{\sigma}, \tag{75}$$

where $\sigma_\alpha = T_{k\alpha}$ and $\sigma = r_k$; $k = 1, 2, 3$. This is integrated over the region containing the node, enclosed by the quadrilateral of Figure 1, yielding

$$\Sigma^{i,j,n} = m^{i,j} \ddot{\sigma}^{i,j,n}, \tag{76}$$

where n is the time step,

$$\Sigma^{i,j,n} = 2A^{i,j} (\sigma_{\alpha,\alpha})^{i,j,n}, \tag{77}$$

and

$$m^{i,j} = 2A^{i,j} \rho_r \tag{78}$$

is the nodal mass.

The right-hand side of (76) is evaluated in terms of the zone-centered values of σ_α via (67). The latter depend constitutively on corresponding zone-centered values of the gradients $\sigma_{,\alpha}$ which, in turn, are determined via (70) by the values of σ at the nodes located at the vertices of the shaded region of Figure 1. The scheme requires one degree of differentiability less than that required by the local differential equations. Discussions of the associated truncation errors are given in [Silling 1988; Herrmann and Bertholf 1983].

We observe that the matrix $G_{k\beta}$ associated with lateral pressure (not to be confused with the plastic deformation) is evaluated at zone-centered points (cf. (72)). However, this involves the deformation r_k (cf. (73)), a nodal variable; in place of this we substitute the average of the deformations at the four adjacent nodes.

The time derivatives in (76) are approximated by the central differences

$$\dot{\sigma}^n = \tfrac{1}{2}(\dot{\sigma}^{n+1/2} + \dot{\sigma}^{n-1/2}), \quad \ddot{\sigma}^n = \tfrac{1}{\epsilon}(\dot{\sigma}^{n+1/2} - \dot{\sigma}^{n-1/2}), \quad \dot{\sigma}^{n-1/2} = \tfrac{1}{\epsilon}(\sigma^n - \sigma^{n-1}), \tag{79}$$

where ϵ is the time increment and the node label (i, j) has been suppressed. Substitution into (76) furnishes the explicit, decoupled system

$$\begin{aligned}
m^{i,j} \dot{\sigma}^{i,j,n+1/2} &= m^{i,j} \dot{\sigma}^{i,j,n-1/2} + \epsilon \Sigma^{i,j,n}, \\
\sigma^{i,j,n+1} &= \sigma^{i,j,n} + \epsilon \dot{\sigma}^{i,j,n+1/2},
\end{aligned} \tag{80}$$

which is used to advance the solution in time node-by-node.

The starting procedure is derived from the quiescent initial conditions $r = u$ and $\dot{r} = 0$ for $t \le 0$, and the initial values of the director and plastic deformation fields are $d = k$ and $K = I$, corresponding to $\chi = x$ and $H = F = I$; the constitutive equations then require that the initial value of the Biot stress vanish. The boundary condition is $r(u, t) = u$ on $\partial\Omega$, for all t.

Stability of the scheme is ensured by using sufficiently small time steps selected on the basis of successive trials based on a sequence of values of ϵ.

Our procedure presumes a degree of regularity for the solution that is not consistent with the existence of shocks. Accordingly, we do not append associated discontinuity relations. The inclusion of such conditions would be appropriate in a numerical scheme based on the method of characteristics, such as described in [Cristescu 1967] in the setting of axisymmetry involving a single spatial dimension (the

radius). In contrast, the present procedure is a direct numerical simulation in the spirit of conventional structural dynamics. A similar approach was used to describe the potentially nonhyperbolic dynamics of elastic strings in [Yokota et al. 2001], where, with sufficient mesh refinement, it was shown to furnish close approximations to solutions containing genuine shocks obtained by characteristic-based methods [Beatty and Haddow 1985]. Nevertheless this issue furnishes a logical point of departure for further study, and it is in this sense that our simulations may be regarded as preliminary numerical experiments.

4.2. *Updating the director, the stress and the plastic deformation.* Given the nodal deformation $r(u, t_n)$, we use (70) to compute $\nabla r(u, t_n)$ at zone-centered points. The zone-centered values of $K(u, t_n)$ are combined with (1) to express the elastic deformation $H(u, t_n)$ in terms of $d(u, t_n)$, which remains to be determined. To this end we form the elastic Cauchy–Green deformation C_H and compute the associated invariants $H_1 = \operatorname{tr} C_H$, $H_2 = \frac{1}{2}[I_1^2 - \operatorname{tr}(C_H)^2]$ and $H_3 = \det C_H$; these are used to obtain the *elastic* principal stretches [Rivlin 2004]

$$\lambda_k = \frac{1}{\sqrt{3}}\left\{H_1 + 2A\cos\left[\tfrac{1}{3}(\phi - 2\pi k)\right]\right\}^{1/2}; \quad k = 1, 2, 3, \tag{81}$$

where

$$\begin{aligned} A &= (H_1^2 - 3H_2)^{1/2} \quad \text{and} \\ \phi &= \cos^{-1}\left[\frac{1}{2A^3}(2H_1^3 - 9H_1 H_2 + 27H_3)\right], \end{aligned} \tag{82}$$

and then the invariants

$$\begin{aligned} h_1 &= \lambda_1 + \lambda_2 + \lambda_3, \\ h_2 &= \lambda_1\lambda_2 + \lambda_1\lambda_3 + \lambda_2\lambda_3, \\ h_3 &= \lambda_1\lambda_2\lambda_3 \end{aligned} \tag{83}$$

of the *elastic* right stretch tensor U_H.

With these in hand we form the strain-energy function $w(h_1, h_2, h_3)$ from (36) and (37). The resulting expression is identified with the function $R(d)$ of Section 3. We have shown there that a solution to the plane-stress condition $(55)_2$ (or (64)) furnishes the unique minimizer of this function. Being strictly convex, the latter meets the hypotheses of convergence theorems for iterative gradient minimization algorithms such as the Cauchy–Goldstein method of steepest descents [Saaty and Bram 1964; Goldstein 1962].

With $d(u, t_n)$ thus determined, we use the Cayley–Hamilton formula [Steigmann 2002]

$$hU_H = h_1 h_3 I + (h_1^2 - h_2)C_H - C_H^2 \tag{84}$$

to compute the elastic stretch directly, where

$$h = h_1 h_2 - h_3 = (\lambda_1 + \lambda_2)(\lambda_1 + \lambda_3)(\lambda_2 + \lambda_3), \tag{85}$$

which is strictly positive. This is used to compute the zone-centered value of $\sigma^n U_H^n$ via (38) and (41). We then check the sign of the function $F^n = F(t_n)$ in (42) and decide accordingly whether or not to update the plastic deformation. If $F^n \leq 0$ we set $K^{n+1} = K^n$ at zone-centered points; otherwise we

evaluate $\boldsymbol{K}^{n+1} = \boldsymbol{K}^n + \epsilon \dot{\boldsymbol{K}}^n$, where (cf. (42) with $\boldsymbol{GK} = \boldsymbol{I}$)

$$\dot{\boldsymbol{K}}^n = -(F^n/\nu)\boldsymbol{K}^n \operatorname{Dev}(\boldsymbol{\sigma}^n \boldsymbol{U}_H^n). \tag{86}$$

4.3. *Examples*. We conclude by presenting the results of some simulations. Our purpose is to demonstrate that the present model is amenable to computation, and that it furnishes realistic predictions. We make no effort to simulate actual experimental data or to benchmark our predictions against alternative simulations. Indeed, we have not found any alternative simulations in the literature.

In the examples considered the membrane is subjected to a suddenly applied spatially uniform pressure that decays exponentially in time. A spanwise dimension, L, of the reference plane Ω is used to define dimensionless initial and final position vectors $\boldsymbol{u}$ and $\boldsymbol{r}$. Nondimensional time is defined by $\bar{t} = \sqrt{\lambda/\rho_r}(t/L)$, where t is physical time, λ is a Lamé modulus (cf. (41)) and ρ_r is the referential mass density occurring in $(55)_1$. All stress measures are nondimensionalized by λ, and the dimensionless shear modulus is $\bar{\mu} = \mu/\lambda$. We also use the dimensionless yield stress $\bar{K} = K/\lambda$ and viscosity $\bar{\nu} = \sqrt{\rho_r/\lambda}(\nu L/\lambda)$ in the flow rule. The term P in $(55)_1$, representing the actual pressure divided by initial membrane thickness h, is given by $P(t) = (\lambda/L)\bar{P}(\bar{t})$, where $\bar{P}$ is a dimensionless function; the actual pressure is $p(t) = \lambda(h/L)\bar{P}(\bar{t})$, to leading order in h/L. Here, for illustrative purposes, we impose $\bar{P}(\bar{t}) = \bar{P}_0 \exp(-\bar{t})$, where $\bar{P}_0$ is a constant.

Figures 2 and 3 depict the response of an initially square membrane. Here L is taken to be the length of a side, and $L/h = 100$. The selected parameter values are $\bar{K} = 4.93 \times 10^{-4}$, $\bar{\mu} = 0.470$ and $\bar{\nu} = 5.00 \times 10^5$, and the pressure intensity is $\bar{P}_0 = 7.04$. This is sufficient to induce substantial deformation, shown in Figure 2 for an interval spanning peak positive and negative vertical displacements, corresponding to roughly one half of the initial period of oscillation. The pressure induces a wave emanating from the boundaries of the domain and converging toward the center, followed by an interaction phase and a subsequent reversal of the direction of motion over most of the domain. The transient elastic strain is seen to be quite substantial (left image in Figure 3) and well beyond the range of validity of the classical linear relations typically assumed between stress and elastic strain. Also shown (right image in Figure 3) is the history of the norm of the cross product $\boldsymbol{d} \times \boldsymbol{n}$; this is nonzero whenever the Kirchhoff–Love hypothesis fails. The substantial plastic distortion generated in this example is such as to lead to a slight deviation from Kirchhoff–Love kinematics.

We emphasize the fact that the parameters of the model may require adjustment to enhance the simulations from the quantitative standpoint. Here we have simply chosen the parameter values for the purpose of illustrating the general nature of the transient response predicted by the model.

In the second example a circular disc of radius L is subjected to the same pressure distribution, but of a smaller intensity $\bar{P}_0 = 2.82$. All other parameters are as in the first example, and again $L/h = 100$. Snapshots of the motion and the histories of the norms of the elastic strain and $\boldsymbol{d} \times \boldsymbol{n}$ are displayed in Figures 4 and 5. The elastic strain is again seen to be substantial, but the deviation from Kirchhoff–Love kinematics is reduced, due to the diminished plastic distortion attending the smaller pressure pulse.
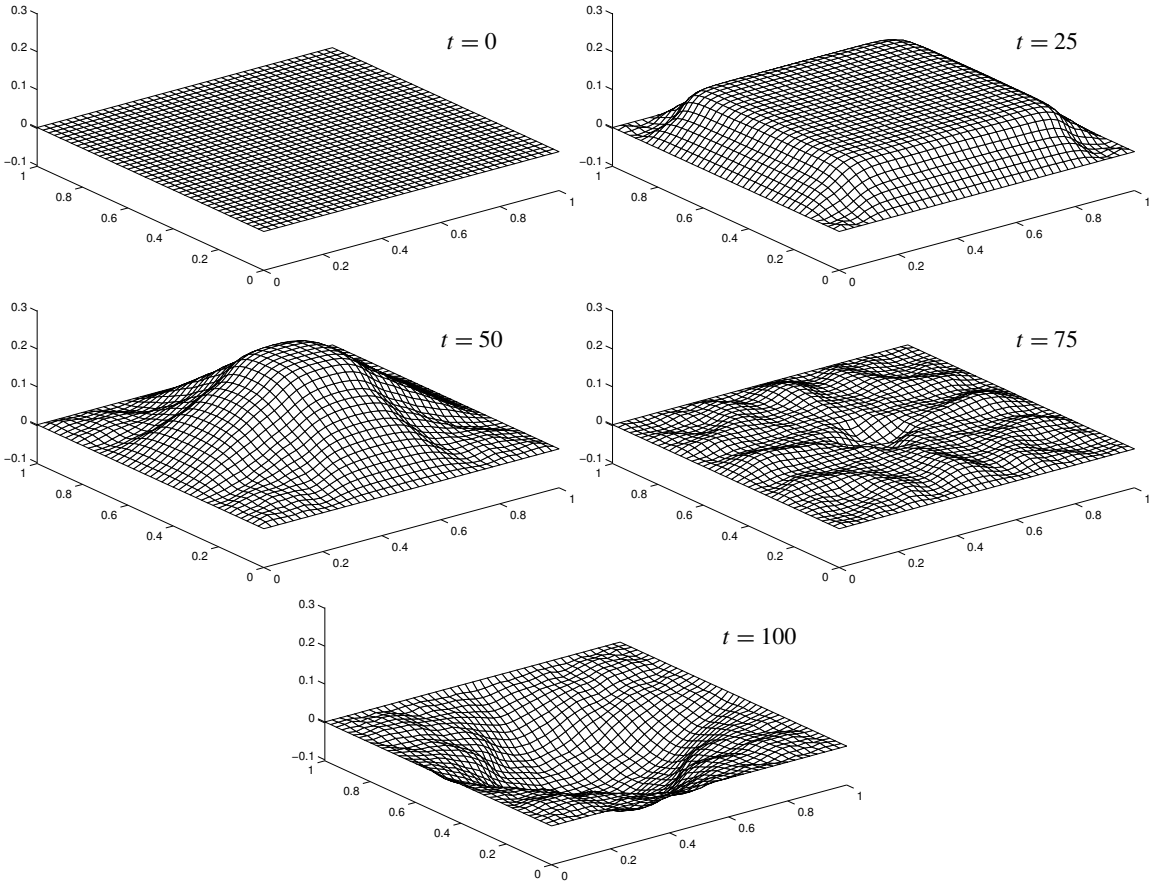
Figure 2. Configurations of a square membrane subjected to blast pressure at a sequence of times.
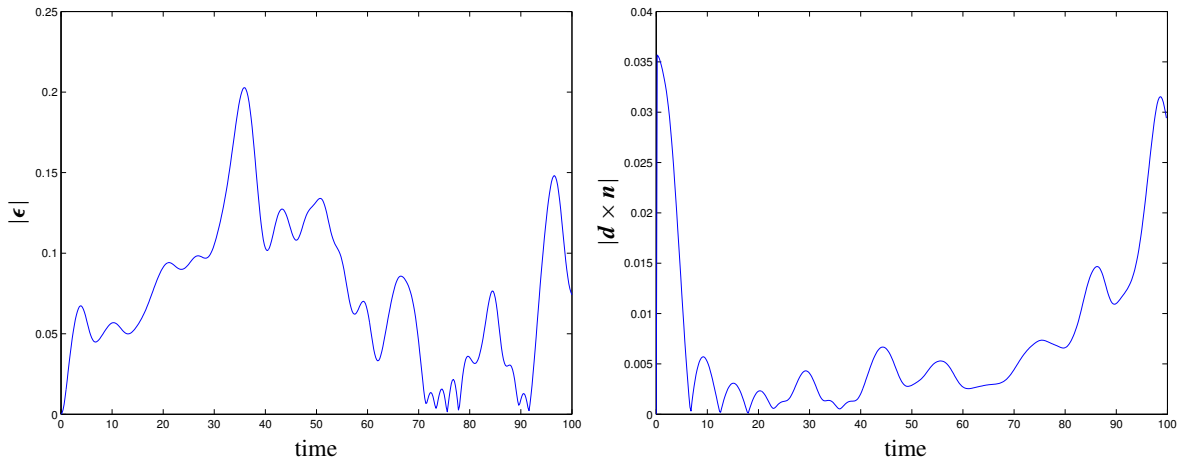
Figure 3. Left: norm of transient Biot strain midway along an edge of the square. Right: norm of $\boldsymbol{d} \times \boldsymbol{n}$ midway along an edge of the square.
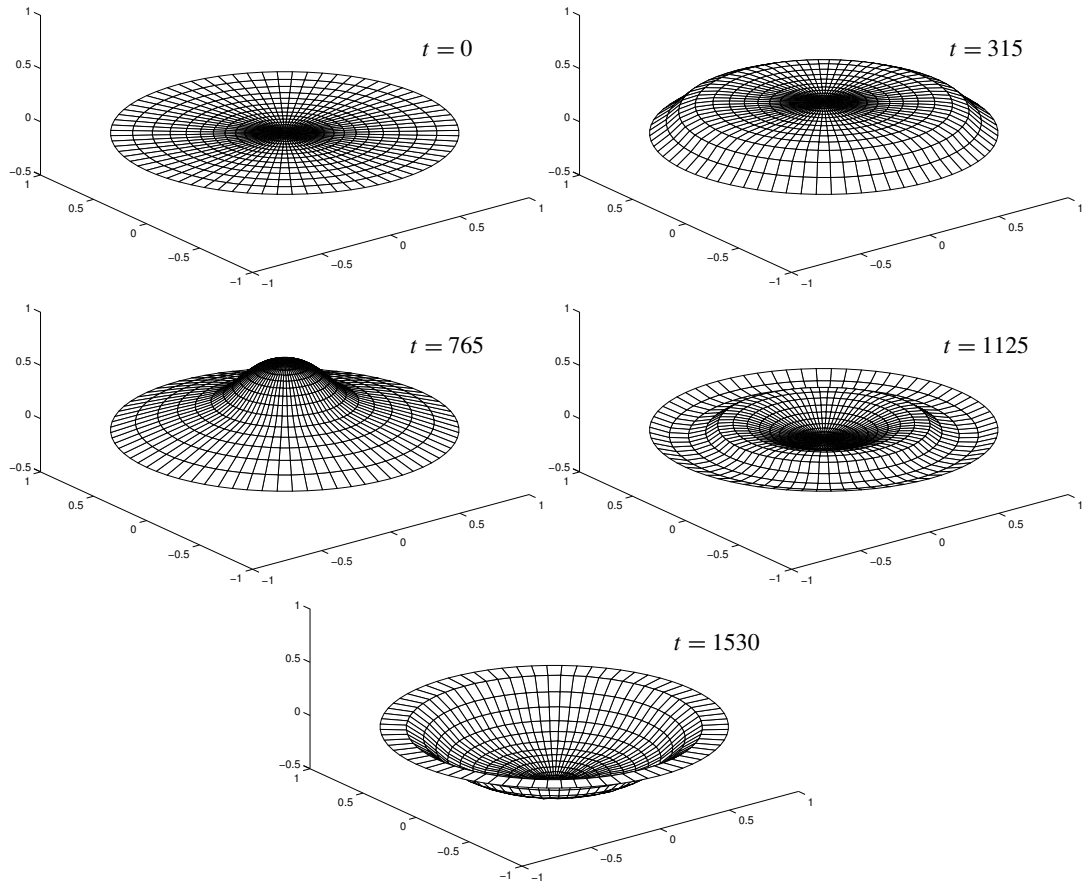
Figure 4. Configurations of a circular membrane subjected to blast pressure at a sequence of times.
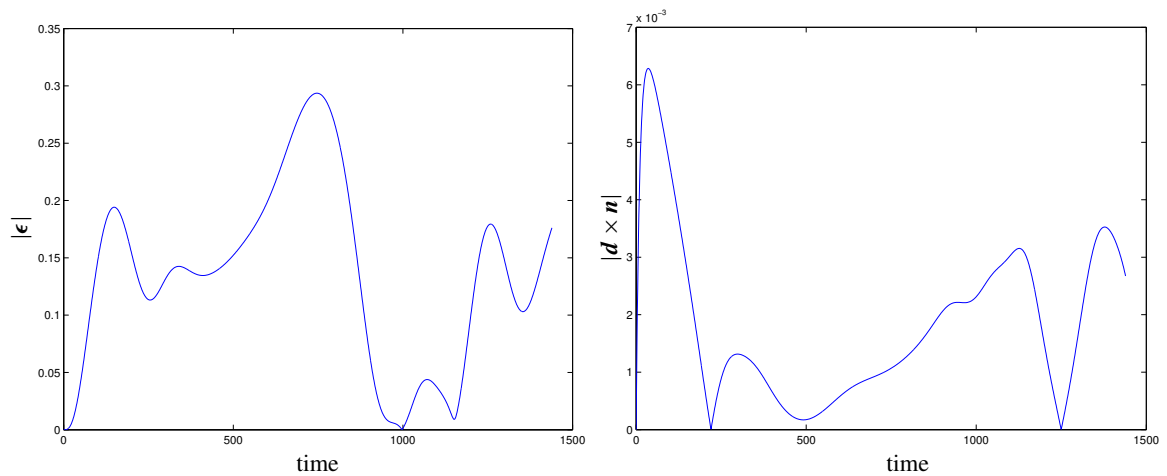
Figure 5. Left: norm of transient Biot strain at the edge of the circle. Right: norm of $\boldsymbol{d} \times \boldsymbol{n}$ at the edge of the circle.

References

[Atai and Steigmann 1998] A. A. Atai and D. J. Steigmann, "Coupled deformations of elastic curves and surfaces", *Int. J. Solids Struct.* **35**:16 (1998), 1915–1952.

[Beatty and Haddow 1985] M. F. Beatty and J. D. Haddow, "Transverse impact of a hyperelastic stretched string", *J. Appl. Mech. (ASME)* **52**:1 (1985), 137–143.

[Bigoni 2012] D. Bigoni, *Nonlinear solid mechanics: Bifurcation theory and material instability*, Cambridge University Press, 2012.

[Bilby 1960] B. A. Bilby, "Continuous distributions of dislocations", pp. 329–398 in *Progress in solid mechanics, I*, edited by R. Hill and I. N. Sneddon, North-Holland, Amsterdam, 1960.

[Carroll 1988] M. M. Carroll, "Finite strain solutions in compressible isotropic elasticity", *J. Elasticity* **20**:1 (1988), 65–92.

[Cleja-Ţigoiu and Soós 1990] S. Cleja-Ţigoiu and E. Soós, "Elastoviscoplastic models with relaxed configurations and internal state variables", *Appl. Mech. Rev. (ASME)* **43**:7 (1990), 131–151.

[Cristescu 1967] N. Cristescu, *Dynamic Plasticity*, North-Holland Series in Applied Mathematics and Mechanics **4**, North-Holland, Amsterdam, 1967.

[Dacorogna 1989] B. Dacorogna, *Direct methods in the calculus of variations*, Applied Mathematical Sciences **78**, Springer, Berlin, 1989.

[Epstein and Elżanowski 2007] M. Epstein and M. Elżanowski, *Material inhomogeneities and their evolution: A geometric approach*, Springer, Berlin, 2007.

[Goldstein 1962] A. A. Goldstein, "Cauchy's method of minimization", *Numer. Math.* **4** (1962), 146–150.

[Gupta et al. 2007] A. Gupta, D. J. Steigmann, and J. S. Stölken, "On the evolution of plasticity and incompatibility", *Math. Mech. Solids* **12**:6 (2007), 583–610.

[Gupta et al. 2011] A. Gupta, D. J. Steigmann, and J. S. Stölken, "Aspects of the phenomenological theory of elastic-plastic deformation", *J. Elasticity* **104**:1-2 (2011), 249–266.

[Gurtin et al. 2010] M. E. Gurtin, E. Fried, and L. Anand, *The mechanics and thermodynamics of continua*, Cambridge University Press, 2010.

[Haseganu and Steigmann 1994] E. M. Haseganu and D. J. Steigmann, "Analysis of partly wrinkled membranes by the method of dynamic relaxation", *Comput. Mech.* **14**:6 (1994), 596–614.

[Herrmann and Bertholf 1983] W. Herrmann and L. D. Bertholf, "Explicit Lagrangian finite difference methods", pp. 361–416 in *Computational methods for transient analysis*, edited by T. Belytschko and T. J. R. Hughes, Mechanics and Mathematical Methods **1**, Elsevier, Amsterdam, 1983.

[Krishnan and Steigmann 2014] J. Krishnan and D. J. Steigmann, "A polyconvex framework for isotropic elastoplasticity theory", *IMA J. Appl. Math.* **79**:5 (2014), 722–738.

[Kröner 1960] E. Kröner, "Allgemeine Kontinuumstheorie der Versetzungen und Eigenspannungen", *Arch. Ration. Mech. Anal.* **4** (1960), 273–334.

[Le Dret and Raoult 1996] H. Le Dret and A. Raoult, "The membrane shell model in nonlinear elasticity: A variational asymptotic derivation", *J. Nonlinear Sci.* **6**:1 (1996), 59–84.

[Lee 1969] E. H. Lee, "Elastic-plastic deformation at finite strain", *J. Appl. Mech. (ASME)* **36**:1 (1969), 1–6.

[Lubliner 2008] J. Lubliner, *Plasticity Theory*, Dover, Mineola, NY, 2008.

[Malvern 1951] L. E. Malvern, "The propagation of longitudinal waves of plastic deformation in a bar of material exhibiting a strain-rate effect", *J. Appl. Mech. (ASME)* **18** (1951), 203–208.

[Neff 2003] P. Neff, "Some results concerning the mathematical treatment of finite multiplicative elasto-plasticity", pp. 251–274 in *Deformation and failure in metallic and granular structures*, edited by K. Hutter and H. Baaser, Lecture Notes in Applied and Computational Mechanics **10**, Springer, Berlin, 2003.

[Noll 1967/1968] W. Noll, "Materially uniform simple bodies with inhomogeneities", *Arch. Ration. Mech. Anal.* **27** (1967/1968), 1–32.

[Ogden 1997] R. W. Ogden, *Non-linear elastic deformations*, Dover, Mineola, NY, 1997.

[Perzyna 1962/1963] P. Perzyna, "The constitutive equations for rate sensitive plastic materials", *Quart. Appl. Math.* **20** (1962/1963), 321–332.

[Perzyna 1966] P. Perzyna, "Fundamental problems in viscoplasticity", pp. 243–377 Adv. Appl. Math. **9**, 1966.

[Pipkin 1986] A. C. Pipkin, "The relaxed energy density for isotropic elastic membranes", *IMA J. Appl. Math.* **36**:1 (1986), 85–99.

[Prager 1961] W. Prager, *Introduction to mechanics of continua*, Ginn, Boston, 1961.

[Rajagopal and Srinivasa 1998] K. Rajagopal and A. Srinivasa, "Inelastic behaviour of materials, I: Theoretical underpinnings", *Int. J. Plast.* **14**:10-11 (1998), 945–967.

[Rivlin 2004] R. S. Rivlin, "A note on the constitutive equation for an isotropic elastic material", *Math. Mech. Solids* **9**:2 (2004), 121–129.

[Saaty and Bram 1964] T. L. Saaty and J. Bram, *Nonlinear mathematics*, McGraw-Hill, New York, 1964. Reprinted Dover, New York, 1981.

[Sfyris 2011] D. Sfyris, "The strong ellipticity condition under changes in the current and reference configuration", *J. Elasticity* **103**:2 (2011), 281–287.

[Silling 1988] S. A. Silling, "Finite difference modelling of phase changes and localization in elasticity", *Comput. Methods Appl. Mech. Eng.* **70**:3 (1988), 251–273.

[Steigmann 1990] D. J. Steigmann, "Tension-field theory", *Proc. R. Soc. Lond. A* **429**:1876 (1990), 141–173.

[Steigmann 2002] D. J. Steigmann, "Invariants of the stretch tensors and their application to finite elasticity theory", *Math. Mech. Solids* **7**:4 (2002), 393–404.

[Steigmann 2003] D. J. Steigmann, "On isotropic, frame-invariant, polyconvex strain-energy functions", *Quart. J. Mech. Appl. Math.* **56**:4 (2003), 483–491.

[Steigmann 2009] D. J. Steigmann, "A concise derivation of membrane theory from three-dimensional nonlinear elasticity", *J. Elasticity* **97**:1 (2009), 97–101.

[Steigmann 2014] D. J. Steigmann, "Mechanics of materially-uniform thin films", *Math. Mech. Solids* (2014). In press.

[Steigmann and Gupta 2011] D. J. Steigmann and A. Gupta, "Mechanically equivalent elastic-plastic deformations and the problem of plastic spin", *Theor. Appl. Mech.* **38**:4 (2011), 397–417.

[Taylor and Steigmann 2009] M. Taylor and D. J. Steigmann, "Simulation of laminated thermoelastic membranes", *J. Therm. Stresses* **32**:5 (2009), 448–476.

[Wilkins 1963] M. L. Wilkins, "Calculation of elastic-plastic flow", Report UCRL-7322, University of California, Lawrence Radiation Laboratory, 1963.

[Yokota et al. 2001] J. W. Yokota, S. A. Bekele, and D. J. Steigmann, "Simulating the nonlinear dynamics of an elastic cable", *AIAA J.* **39**:3 (2001), 504–510.

ALI A. ATAI: aataee@ut.ac.ir
School of Mechanical Engineering, College of Engineering, University of Tehran, PO Box 4563-11155, Tehran 11155, Iran

DAVID J. STEIGMANN: dsteigmann@berkeley.edu
Department of Mechanical Engineering, University of California, 6133 Etcheverry Hall, Berkeley, CA 94720-1740, United States

SUBMISSION GUIDELINES

ORIGINALITY

Authors may submit manuscripts in PDF format online at the Submissions page. Submission of a manuscript acknowledges that the manuscript is original and has neither previously, nor simultaneously, in whole or in part, been submitted elsewhere. Information regarding the preparation of manuscripts is provided below. Correspondence by email is requested for convenience and speed. For further information, write to contact@msp.org.

LANGUAGE

Manuscripts must be in English. A brief abstract of about 150 words or less must be included. The abstract should be self-contained and not make any reference to the bibliography. Also required are keywords and subject classification for the article, and, for each author, postal address, affiliation (if appropriate), and email address if available. A home-page URL is optional.

FORMAT

Authors can use their preferred manuscript-preparation software, including for example Microsoft Word or any variant of TeX. The journal itself is produced in LaTeX, so accepted articles prepared using other software will be converted to LaTeX at production time. Authors wishing to prepare their document in LaTeX can follow the example file at www.jomms.net (but the use of other class files is acceptable). At submission time only a PDF file is required. After acceptance, authors must submit all source material (see especially Figures below).

REFERENCES

Bibliographical references should be complete, including article titles and page ranges. All references in the bibliography should be cited in the text. The use of BibTeX is preferred but not required. Tags will be converted to the house format (see a current issue for examples); however, for submission you may use the format of your choice. Links will be provided to all literature with known web locations; authors can supply their own links in addition to those provided by the editorial process.

FIGURES

Figures must be of publication quality. After acceptance, you will need to submit the original source files in vector format for all diagrams and graphs in your manuscript: vector EPS or vector PDF files are the most useful. (EPS stands for Encapsulated PostScript.)

Most drawing and graphing packages—Mathematica, Adobe Illustrator, Corel Draw, MATLAB, etc.—allow the user to save files in one of these formats. Make sure that what you're saving is vector graphics and not a bitmap. If you need help, please write to graphics@msp.org with as many details as you can about how your graphics were generated.

Please also include the original data for any plots. This is particularly important if you are unable to save Excel-generated plots in vector format. Saving them as bitmaps is not useful; please send the Excel (.xls) spreadsheets instead. Bundle your figure files into a single archive (using zip, tar, rar or other format of your choice) and upload on the link you been given at acceptance time.

Each figure should be captioned and numbered so that it can float. Small figures occupying no more than three lines of vertical space can be kept in the text ("the curve looks like this:"). It is acceptable to submit a manuscript with all figures at the end, if their placement is specified in the text by means of comments such as "Place Figure 1 here". The same considerations apply to tables.

WHITE SPACE

Forced line breaks or page breaks should not be inserted in the document. There is no point in your trying to optimize line and page breaks in the original manuscript. The manuscript will be reformatted to use the journal's preferred fonts and layout.

PROOFS

Page proofs will be made available to authors (or to the designated corresponding author) at a Web site in PDF format. Failure to acknowledge the receipt of proofs or to return corrections within the requested deadline may cause publication to be postponed.